The Astrophysical Journal, 763:148 (30pp), 2013 February 1 doi:10.1088/0004-637X/763/2/148

CHARACTERIZING THE CIRCUMGALACTIC MEDIUM OF NEARBY GALAXIES WITH *HST*/COS AND *HST*/STIS ABSORPTION-LINE SPECTROSCOPY*

John T. Stocke[1], Brian A. Keeney[1], Charles W. Danforth[1], J. Michael Shull[1], Cynthia S. Froning[1], James C. Green[1], Steven V. Penton[1], and Blair D. Savage[2]
[1] Center for Astrophysics and Space Astronomy, Department of Astrophysical and Planetary Sciences, University of Colorado, 389 UCB, Boulder, CO 80309, USA; john.stocke@colorado.edu
[2] Department of Astronomy, University of Wisconsin, Madison, WI 53706, USA
Received 2012 October 19; accepted 2012 December 21; published 2013 January 17

ABSTRACT

The circumgalactic medium (CGM) of late-type galaxies is characterized using UV spectroscopy of 11 targeted QSO/galaxy pairs at $z \leqslant 0.02$ with the *Hubble Space Telescope* Cosmic Origins Spectrograph (COS) and ∼60 serendipitous absorber/galaxy pairs at $z \leqslant 0.2$ with the Space Telescope Imaging Spectrograph. CGM warm cloud properties are derived, including volume filling factors of 3%–5%, cloud sizes of 0.1–30 kpc, masses of 10–10^8 $M_\odot$, and metallicities of ∼0.1–1 $Z_\odot$. Almost all warm CGM clouds within 0.5 $R_{\rm vir}$ are metal-bearing and many have velocities consistent with being bound, "galactic fountain" clouds. For galaxies with $L \gtrsim 0.1\,L^*$, the total mass in these warm CGM clouds approaches 10^{10} $M_\odot$, ∼10%–15% of the total baryons in massive spirals and comparable to the baryons in their parent galaxy disks. This leaves ≳50% of massive spiral-galaxy baryons "missing." Dwarfs ($<0.1\,L^*$) have smaller area covering factors and warm CGM masses (≲5% baryon fraction), suggesting that many of their warm clouds escape. Constant warm cloud internal pressures as a function of impact parameter ($P/k \sim 10\,{\rm cm}^{-3}$ K) support the inference that previous COS detections of broad, shallow O VI and Lyα absorptions are of an extensive (∼400–600 kpc), hot ($T \approx 10^6$ K), intra-cloud gas which is very massive ($\geqslant 10^{11}$ $M_\odot$). While the warm CGM clouds cannot account for all the "missing baryons" in spirals, the hot intra-group gas can, and could account for ∼20% of the cosmic baryon census at $z \sim 0$ if this hot gas is ubiquitous among spiral groups.

Key words: galaxies: dwarf – galaxies: groups: general – galaxies: halos – galaxies: spiral – intergalactic medium – quasars: absorption lines

Online-only material: color figures

1. INTRODUCTION

The characterization of the circumgalactic medium (CGM) is necessary for any detailed understanding of galaxy formation and evolution, but its direct detection has been, so far, elusive. The theoretical case for a massive CGM is demonstrated by the continuing high star formation rate (SFR) in spiral galaxies (Binney & Tremaine 1987; Chomiuk & Povich 2011) as well as the detailed metallicity history in galaxies (e.g., the "G dwarf problem"; Larson 1972; Binney & Tremaine 1987; Chiappini et al. 2001), requiring that any successful model of galactic evolution is not a "closed box." Low-metallicity gas must be accreted by each star-forming galaxy to explain these basic observables (∼1 $M_\odot$ yr^{-1} for the Milky Way), but how much gas is present in the CGM at any one time? And how much of this is accreted from outside the system versus how much is recycled from the galaxy through the CGM? Additionally, there exists a substantial deficiency of detected baryons in spiral galaxies relative to the cosmic ratio of baryons to dark matter (e.g., McGaugh et al. 2000; Klypin et al. 2001) that seems to require a CGM baryonic mass much greater than the total amount in the galaxy's disk. The direct measurement of the amount, extent, ionization state (and thus total mass), metallicity, and origin of the multi-phase CGM (a.k.a. the galactic "halo"; Spitzer 1956) remains largely uncharacterized. This is due both to its low density (and thus low emission measure) and also to its range of temperatures (thought to be 10^4–10^6 K) which makes it impossible to detect in emission beyond a few kiloparsecs above galactic disks using current instruments.

For our own Galaxy, the detection of some small amount of CGM gas has been made possible by observing the so-called high-velocity clouds (HVCs) using H I 21 cm emission (Wakker & van Woerden 1997; Wakker 2001; Putman et al. 2012), but the number of baryons in HVCs is not substantial. Recently, various methods for determining, or at least bracketing HVC distances, have found that these clouds are only a few kpc away (Bland-Hawthorn & Maloney 1999; Putman et al. 2003; Wakker et al. 2007; Lehner & Howk 2011). Many remain without distance estimates, leading to suggestions that a subset of HVCs are ≫10 kpc away and much more massive (Blitz et al. 1999). There is little support for this conjecture, however (Putman et al. 2012). At present, the total infall rate of H I 21 cm detected HVC mass is an order of magnitude short of that required to sustain the current level of star formation in the Milky Way.

However, it is possible to use background active galactic nuclei (AGNs; quasars, QSOs, BL Lac objects, and Seyferts; we will use the abbreviation QSO to refer to these various classes of AGNs collectively), which have large far-UV (FUV) fluxes ($\geqslant 10^{-15}$ erg cm^{-2} s^{-1} Å^{-1}) to probe the full extent of the CGM in both the Milky Way and in other galaxies. In our own Galaxy's halo, the discovery of highly ionized HVCs (Sembach et al. 1995, 2003; Collins et al. 2004) using UV spectroscopy of QSOs has revealed a much larger reservoir of infalling gas (∼1 $M_\odot$ yr^{-1}; Shull et al. 2009; Collins et al. 2009) than the H I 21 cm HVCs. But only in some cases (Lehner & Howk 2011) can the distance to these highly ionized HVCs be determined,

* Based on observations with the NASA/ESA *Hubble Space Telescope*, obtained at the Space Telescope Science Institute, which is operated by AURA, Inc., under NASA contract NAS 5-26555.

allowing their total mass to be estimated. Nevertheless, the mass infall rate estimated by Shull et al. (2009) is sufficient to fuel much of the ongoing Milky Way SFR (2–4 $M_{\odot}$ yr^{-1}; Diehl et al. 2006; Robitaille & Whitney 2010; Shull et al. 2011).

But what is the origin of this infalling material? Observations of similar clouds around other galaxies can generalize their presence to other star-forming galaxies and provide an elementary understanding of a galactic ecology. Using UV spectroscopy of QSOs to study our own Galaxy's gaseous halo and that of other galaxies are nicely complementary. For our own Galaxy, CGM clouds within a few kiloparsecs of the disk are directly detected, and their infalling or outflowing kinematics are readily measured, but their distances are often poorly known. On the other hand, QSO probes of the CGM of other galaxies detect "warm," photoionized and "warm–hot," collisionally ionized clouds at greater galactocentric distances, providing an easily measured lower bound on their galactocentric distances. However, in these cases, cloud kinematics are usually uncertain. And, until recently, very few QSOs near galaxies have been bright enough to provide sufficient targets for multiple probes of single galaxies (Keeney et al. 2012).

The advent of the Cosmic Origins Spectrograph (COS; Green et al. 2012; Osterman et al. 2011) on the *Hubble Space Telescope* (*HST*) has allowed much fainter background target QSOs to be observed. This has facilitated detailed studies of the CGM by targeting fainter QSOs which are projected within the virial radius of a foreground galaxy. Before COS, the Faint Object Spectrograph (FOS) was used to conduct a substantial "Key Project" survey (Bahcall et al. 1993; Weymann et al. 1995; Jannuzi et al. 1998) that detected only the strongest Lyα absorbers ($W_{\lambda} \geqslant 250$ m Å). While many of these do appear associated with bright galaxies (Lanzetta et al. 1995), these absorbers are mostly well outside the virial radius of the nearby bright galaxies and are at distances too great to determine if somewhat fainter galaxies are much closer to the sight line. Later the Goddard High Resolution Spectrograph (GHRS) and the Space Telescope Imaging Spectrograph (STIS) found many weaker absorbers (Morris et al. 1991; Tripp et al. 1998; Penton et al. 2000a, 2000b, 2004; Danforth & Shull 2005, 2008) which were shown to have a much looser association with galaxies (Morris et al. 1993; Bowen et al. 1997; Impey et al. 1999; Penton et al. 2002, 2004; Wakker & Savage 2009). In the GHRS and STIS eras, there was little choice of QSO targets for high-resolution and signal-to-noise UV spectroscopy and any probes of foreground CGM gas were almost entirely "serendipitous." However, given the very small covering factor of galaxies and their CGM on the sky, there are few detected serendipitous CGM absorbers, and, when detected, these absorbers are most often in the outermost parts of the CGM at close to or just beyond the virial radius. The 10-fold increase in FUV sensitivity of COS now allows a substantial list of possible targets, including numerous QSOs close enough on the sky to foreground galaxies to probe the inner and outer CGM of nearby galaxies.

The tactic taken by several other *HST*/COS observers, as first reported in Tumlinson et al. (2011), is to use the vast database of the Sloan Digital Sky Survey (SDSS) to locate foreground galaxies near UV-bright targets. Owing to the flux-limited nature of the SDSS photometry and spectroscopy, this approach allows a study of the CGM of luminous galaxies out to $z \approx 0.2$–0.3. These redshifts maximize COS detectability of both higher order H I Lyman lines and the critical O VI absorption doublet, which probes so-called warm–hot gas at $T \approx 10^5$–$10^{6.3}$ K. However, the ionization mechanism for this transition remains controversial, as both photoionization (Davé & Oppenheimer 2007; Tripp et al. 2008) and collisional ionization due to shocks (Cen & Ostriker 1999; Shull et al. 2012) have been proposed. This ambiguity makes the interpretation of CGM O VI detections more uncertain, but the use of O VI absorption is essential to fully characterize the CGM gas.

The tactic taken by the COS Science Team (hereafter called Guaranteed Time Observers or GTOs) is complementary to the Tumlinson et al. approach. We have searched for bright QSOs near on the sky to very nearby ($z \leqslant 0.02$) galaxies with a range of luminosities (<0.01 L^* to L^*) and morphologies (massive spirals to dwarf irregulars, including starbursting systems, and low surface brightness galaxies). In this way, we have probed the CGM of a variety of late-type galaxies. Although the sample has limited size and is somewhat biased in its target selection, we have nevertheless constructed it with the goal of characterizing the CGM of late-type galaxies of various luminosities and morphologies for input into models of galactic evolution. At low redshift the diagnostic absorption lines of low ions Si II, C II, and Si III and the high ions Si IV and C IV as well as the H I Lyα line are available within the COS FUV bandpass (1150–1800 Å) for detection and study. While O VI absorption is more controversial, these FUV low- and high-ionization metal lines have strengths that are well modeled for the most part assuming photoionization provided by the extragalactic ionizing radiation field. This extragalactic background has been well characterized locally (Shull et al. 2012; Haardt & Madau 2012) and so can be used to model warm ($T \sim 10^4$ K) CGM clouds and the CGM in general. Throughout this paper we will refer to these clouds as "warm CGM" absorbers, an observational definition based originally on the popular three-phase interstellar medium model. A confusion in terminology has arisen recently when theoretical modelers refer to any gas at less than the virial temperature of a system ($T \sim 10^6$ K for a massive galaxy) as "cold." It is quite plausible that "cold accretion" (Kereš & Hernquist 2009; Kereš et al. 2009) could consist largely of what we term here "warm" CGM clouds.

Using a sample of very nearby galaxies also offers the possibility of in-depth scrutiny of the host galaxy. For example, deep Hα imaging for SFRs, long-slit emission-line spectroscopy for galaxy rotation curves, and H I 21 cm imaging spectroscopy for rotation curves and to search for extra-planar H I emission can all be brought to bear when the targeted galaxy is at $z \leqslant 0.02$. Galaxy metallicity measurements provided by H II region spectroscopy and/or Lick absorption line indices help constrain absorber metallicity and provide important limits for successful physical models of CGM clouds created within the galaxy either as "fountains" or unbound "winds"; i.e., unless there are very nearby galaxies with higher luminosity (and potentially higher metallicity), $Z_{\rm abs} \leqslant Z_{\rm gal}$ can be assumed as a useful constraint on models of CGM clouds. It is even possible in some cases at low-z to infer whether the gas is infalling or outflowing by using internal extinction patterns across the galaxy disk and assuming that any outflow or infall is largely vertical to the galaxy's disk (Stocke et al. 2010). These complementary studies of the host galaxy to the absorbers are not possible in such detail even at $z \sim 0.3$.

For the purposes of this paper, we define the CGM as the gas within the virial radius of the galaxy without reference to its dynamical state; i.e., infalling from outside the galaxy (extragalactic "cold accretion"; Kereš & Hernquist 2009; Kereš et al. 2009; Kacprzak et al. 2010), infalling after first being outflowing (i.e., a "galactic fountain"; Shull et al. 2009; Lehner

& Howk 2011), outflowing but bound (also a galactic fountain; Keeney et al. 2005), or outflowing and unbound (a "galactic wind" as advocated for many systems by Lehnert & Heckman 1996; Heckman et al. 2000; Shapley et al. 2003; Weiner et al. 2009; Martin et al. 2012, among others). While absorption-line spectroscopy against the continuum source produced by a starburst galaxy nucleus can determine infall versus outflow unambiguously, the location of the absorbing material relative to the galaxy potential is not well determined. Thus, whether outflowing gas escapes into the intergalactic medium (IGM) is not well determined either. In the case of a QSO sight line passing close to a foreground galaxy, the impact parameter provides a lower limit on the physical distance of the absorbing gas and the radial velocity difference allows a reasonable, but not fully unambiguous, determination of whether this gas escapes from the galaxy into the IGM (see, e.g., Tumlinson et al. 2011). Thus, both techniques, observing absorption against starburst continua and observing QSO/galaxy pairs, have significant limitations as well as unique advantages.

In this paper, we present a two-pronged approach to addressing the nature of the CGM using UV spectroscopy of background QSOs near on the sky to foreground galaxies. Two samples of absorber/galaxy pairs are investigated: targeted detections made using COS and serendipitous detections from the STIS/*FUSE* archives.

In Section 2, we present a modest-sized sample of 11 QSO/galaxy pairs (11 QSO targets probing 10 foreground galaxies) targeted for observation with COS because the QSO sight line passes within the virial radius of the foreground galaxy. The targeted galaxies are all late-type and at very low redshift ($z \leqslant 0.02$). At these redshifts the COS FUV spectra are very sensitive to Lyα, as well as covering the wavelengths of low and high ions plausibly photoionized, ranging from C II λ1335 and Si III λ1206 to Si IV $\lambda\lambda$1393, 1403 and C IV $\lambda\lambda$1548, 1552. While N V is present within the spectral coverage, this doublet is usually very weak, and the wavelengths of O VI are not covered by these spectra so that little or no information is available for the highest ions likely to be present in these clouds. The detection of the low and high ions listed above allows an estimate of the basic physical structure of the clouds (e.g., density, size, ionized fraction, and total mass) from standard photoionization modeling while leaving the amount of hotter gas poorly constrained. In addition, with only the first transition of the Lyman series detectable at the redshifts of the foreground galaxies, the column density of H I is sometimes not well constrained either since CGM Lyα is usually saturated, creating some uncertainty in absorber metallicity. This small sample was chosen for observation by the GTOs in the first three years of COS operation. The observational details of the individual sight lines, their absorber detections and photoionization modeling of the absorbing gas can be found in a companion paper (B. A. Keeney et al. 2013, in preparation, hereafter Paper II). Section 2 summarizes these targets and observations.

In Section 3, we present the analysis of a serendipitous sample of QSO/galaxy pairs, again focusing on those sight lines which pass within the virial radius of a foreground galaxy. In this case we have used the sample of ~500 Lyα absorbers with $N_{\rm H\,I} \geqslant 10^{13.0}\,{\rm cm}^{-2}$ (hereafter all column densities are quoted in $\rm cm^{-2}$) found in the high-resolution STIS FUV spectra of QSOs (Danforth & Shull 2008, hereafter DS08). Since none of these QSOs was chosen for observation due to the presence of a foreground galaxy, all QSO/galaxy pairs found in this sample are serendipitous. Galaxy catalogs compiled from large-angle spectroscopic surveys of galaxies (e.g., SDSS and 2dF) were cross-correlated with the STIS sight line locations to find ~700 galaxies $\leqslant$1 Mpc from these sight lines and foreground to the QSO. Because the serendipitous absorber sample was required to have both STIS and *Far-Ultraviolet Spectroscopic Explorer* (*FUSE*) spectroscopy, information on O VI absorption in CGM clouds is available in most cases. *FUSE* spectra also yield coverage of the higher-order Lyman lines and thus to curve-of-growth $N_{\rm H\,I}$ values; photoionization models have been constructed for some of these absorbers in the literature (e.g., Tripp et al. 2002; Tumlinson et al. 2005). New modeling of the serendipitous absorbers with several metal-line detections are presented in Paper II. A summary of results of the photoionization modeling of the metal-line absorbers in both the serendipitous and targeted samples is presented in Section 4.

Some new results on O VI absorbers will also be presented in Sections 3 and 4. Since Stocke et al. (2006) used these same absorber and galaxy samples to investigate the galaxy environment of O VI absorbers, this paper will not add much new information to what has already been published previously. Recent work on O VI absorbers by Prochaska et al. (2011b) finds similar results to Stocke et al. (2006) in closely associating the majority of O VI absorbers with sub-L^* galaxies, but both studies include only modest-sized absorber samples, which largely overlap. Due to its high ionization state and its large f-value, O VI λ1032 is a sensitive probe of very diffuse photoionized gas ($U \geqslant 10^{-1.5}$ or overdensities $\Delta_b \leqslant 30$; Davé et al. 1999; Schaye 2001) or collisionally ionized gas at $T \geqslant 10^5$ K. As such it provides our current best estimates for the spread of metals away from galaxies: ~800 kpc from L^* galaxies and ~450 kpc from 0.1 L^* galaxies (Stocke et al. 2006). However, all of these O VI results are based on quite small sample sizes which will be enlarged soon using COS spectra. O VI absorption shifts into the COS band at $z \gtrsim 0.12$, which requires much deeper galaxy survey work than what is used here to further constrain the spread of metals.

The GTO team is in the process of cataloging all intervening Lyα and metal-line absorbers (especially O VI) in COS GTO spectra (C. W. Danforth et al., in preparation) as well as conducting a wide and deep galaxy survey around each GTO sight line (B. A. Keeney et al., in preparation). Therefore, in Section 4 we combine the COS GTO "targeted" QSO/galaxy sample with a STIS-defined "serendipitous" QSO/galaxy sample to obtain a first look at CGM clouds, their physical properties, masses, and uncertain kinematics.

In Section 5, we discuss the implications of these results for the baryon census in spiral galaxies and galaxy groups and for galactic chemical evolution. We also present the prospects for a better understanding of the CGM of nearby galaxies which will be possible when all currently available COS UV spectroscopy (GTO spectra as well as those of *HST* GOs (Guest Observers)) has been fully analyzed and when detailed foreground galaxy spectroscopy near all COS sight lines has been completed. Section 6 lists our most important results.

Throughout this paper, we use the standard cosmological model with $H_0 = 70.4\,{\rm km\,s^{-1}\,Mpc^{-1}}$, $\Omega_\Lambda = 0.727$, $\Omega_{\rm m} = 0.273$, and $\Omega_{\rm b} = 0.0455$ (Larson et al. 2011).

2. THE COS GTO QSO/GALAXY "TARGETED SURVEY"

With a portion of the orbits allocated to the COS GTO Team, we have conducted a modest-sized survey of the CGM of very

Table 1
Summary of *HST*/COS Observations

Target	z_{em}[a]	Grating	Obs. Date	t_{exp} (s)	F_λ[b] (FEFU)	⟨S/N⟩[c]
1ES 1028+511	0.360	G130M	2011 May 1	14652	3.1	21
		G160M	2011 May 10	14607	2.3	13
1SAX J1032.3+5051	0.173	G130M	2011 Oct 15	11387	1.2	13
		G160M	2011 Oct 23	11342	0.8	8
FBQS J1010+3003	0.256	G130M	2011 May 19	10797	3.1	18
		G160M	2011 May 21	10752	4.6	11
HE 0435−5304	0.425	G130M	2010 Apr 13	8373	2.5	15
		G160M	2010 Apr 13	8936	2.0	11
		G285M	2010 Mar 31	4286	0.9	2
HE 0439−5254	1.053	G130M	2010 Jun 10	8403	4.6	17
		G160M	2010 Jun 10	8936	4.1	12
		G285M	2010 Mar 28	4316	2.2	4
PG 0832+251	0.330	G130M	2011 Apr 19	6135	4.2	16
		G160M	2011 Apr 19	6758	2.1	14
PMN J1103−2329	0.186	G130M	2011 Jul 5	13342	2.4	20
		G160M	2011 Jul 6	13297	1.9	12
RX J0439.6−5311	0.243	G130M	2010 Feb 7	8177	4.3	19
		G160M	2010 Feb 7	8934	3.1	11
		G285M	2010 May 26	4286	1.1	2
SBS 1108+560	0.767	G130M	2011 May 12	8388	0.2	16
		G160M	2011 May 12	8850	4.8	14
SBS 1122+594	0.852	G130M	2010 Nov 7	9875	2.3	14
		G160M	2010 Nov 7	10462	2.9	13
		G285M	2010 Nov 8	10048	2.0	6
VII Zw 244	0.131	G130M	2009 Sep 24	8866	8.4	31
		G160M	2009 Sep 24	6349	6.9	18

Notes.
[a] The emission line redshift of the QSO as listed in the NASA Extragalactic Database (NED), except for HE 0435−5304, whose redshift ($z = 0.425$) was measured from its co-added COS spectrum (NED lists $z = 1.231$ for this QSO).
[b] Continuum level as measured at 1250, 1550, and 2800 Å in the co-added G130M, G160M, and G285M spectra, respectively. Flux levels are listed in femto-erg flux units (FEFUs), where 1 FEFU $= 10^{-15}$ erg s^{-1} cm^{-2} Å^{-1}.
[c] Median S/N per resolution element in the grating passband, as measured by rms continuum deviations in the co-added spectra.

nearby, late-type galaxies. These observations were planned so as to obtain a peak signal-to-noise ratio (S/N) ∼ 15–20 per resolution element of 18 km s^{-1}. For each target both a G130M and a G160M exposure were obtained (see Table 1 for observing log). We limited the total exposures at the high end to avoid a re-pointing due to the South Atlantic Anomaly. A few targets were observed with the G285M grating for 1–2 orbits only to determine whether strong Mg II absorption was present as might be expected for higher $N_{H\,I}$ systems. None were detected. Because of the very low-z of the foreground galaxies targeted, the expected location of Lyα is close to the peak of the COS detector + grating sensitivity. The low redshift of the target galaxy also keeps the C IV doublet in a G160M spectral region of relatively high sensitivity. Thus, good measurements of line strengths have been obtained in all cases for the low and high metal ions so that viable photoionization models of CGM clouds can be well constrained. However, by targeting the CGM of very low-z galaxies, only one transition of the Lyman series is present in the COS bandpass which makes H I column densities uncertain. Because the important O VI doublet is absent from the observed bandpass, photoionization modeling of the absorbing clouds depends on either Si II, Si III, and Si IV, or C II and C IV. A summary of the *HST*/COS observations in the GTO program on QSO/Galaxy Pairs is shown in Table 1. A companion paper (Paper II) will present more details of the observations, data analysis, and photoionization modeling of these absorbers. For a specific example of the data handling and analysis and the detailed procedure for the photoionization modeling of these CGM clouds, see the description of the three sight lines surrounding the low-z galaxy ESO 157−49 (Keeney et al. 2012). All observations for this program except one were successful in obtaining excellent spectra near the planned S/N. Despite obtaining *GALEX* near- and far-UV fluxes for SBS 1108+561, a previously undetected Lyman-limit system (LLS) partially obscured Lyα and Si III λ1206 at the redshift of the foreground galaxy M 108 (i.e., S/N at Lyα and Si III are much less than the value in Table 1). But various metal lines were detected at M 108's redshift (see Table 2), so a detailed analysis of the two absorption systems associated with M 108 was still possible.

2.1. The Sample of "Targeted" QSO/Galaxy Pairs

The basic information on the COS GTO QSO/Galaxy Pairs sample is shown in Table 2. These QSO targets were chosen to be bright enough to provide excellent peak S/N ≈ 15–20 spectra to probe the CGM of a variety of galaxy luminosities at $L < L^*$ and types within the general category of star-forming galaxies. One 0.2 L^* galaxy (ESO 157−49) has three bright QSO targets around it (Keeney et al. 2012). One of these three QSOs (HE 0439−5254) provides a sight line past the major axis of a higher redshift, higher luminosity

Table 2
Targeted CGM Absorber Sample

Target	Galaxy	cz_{abs} (km s^{-1})	cz_{gal} (km s^{-1})	ρ (kpc)	ϕ[a] (°)	L_{gal} ($L*$)	log $N_{H\,I}$[b]	ρ/R_{vir}	$\lvert\Delta v\rvert/v_{esc}$	Associated Metals
1ES 1028+511	UGC 5740	728	649	90	···	0.007	$13.50^{+0.18}_{-0.19}$	0.98–1.68	1.2–2.7	None
1ES 1028+511	SDSS J103108.88+504708.7	961	934	25	−57	0.008	$17.21^{+0.22}_{-3.20}$	0.26–0.46	0.24–0.50	C IV?
1SAX J1032.3+5051	UGC 5740	716	649	65	···	0.007	$13.07^{+0.33}_{-0.52}$	0.71–1.21	0.89–2.0	None
FBQS J1010+3003	UGC 5478	1384	1378	48	89	0.011	$17.79^{+0.11}_{-3.48}$	0.47–0.83	0.061–0.14	None
HE 0435−5304	ESO 157−49	1509	1673	172	245	0.16	13.76 ± 0.12	0.99–1.73	1.4–3.1	None
		1635					$13.91^{+0.09}_{-0.11}$		0.31–0.73	None
		1710					$13.58^{+0.16}_{-0.19}$		0.31–0.71	None
HE 0439−5254	ESO 157−49	1662	1673	93	−6	0.16	$14.38^{+0.13}_{-0.07}$	0.54−0.94	0.069−0.15	C IV, Si III/IV
HE 0439−5254	ESO 157−50	3849	3874	88	177	0.53	$14.04^{+0.08}_{-0.06}$	0.40–0.60	0.11–0.19	C IV
PG 0832+251	NGC 2611	5227	5226	53	93	0.63	$18.45^{+0.14}_{-0.20}$	0.23–0.34	0.004–0.006	Many low + high ions
		5425					$15.01^{+2.29}_{-0.24}$		0.71–1.2	C II/IV, Si II/III/IV
PMN J1103−2329	NGC 3511	1194	1114	112	97	0.88	$14.51^{+3.71}_{-0.10}$	0.46–0.65	0.34–0.54	C IV, Si III/IV, N V?
RX J0439.6−5311	ESO 157−49	1671	1673	74	149	0.16	$14.41^{+0.12}_{-0.06}$	0.43–0.75	0.012–0.025	C IV, Si III/IV
SBS 1108+560	M 108	665	696	20	−81	0.64	$14.32^{+4.04}_{-0.22}$	0.09–0.13	0.087–0.14	Many low + high ions
		778					$14.20^{+3.99}_{-0.22}$		0.23–0.36	C IV, Si III/IV
SBS 1122+594	IC 691	1204	1204	32	129	0.091	$17.71^{+0.35}_{-2.85}$	0.21–0.37	0.000–0.000	C II/IV, Si III/IV
VII Zw 244	UGC 4527	712	721	7	···	0.003	$17.75^{+0.19}_{-3.24}$	0.09–0.15	0.074–0.13	C II/IV, Si II/III/IV

Notes. Column densities are given in units of cm^{-2}.
[a] The position angle of the QSO sight line with respect to the galaxy's major axis: $\phi \equiv$ PA(QSO) − PA(gal).
[b] H I column density as determined from Voigt profile fits to the Lyα line. Details of the fitting method can be found in Paper II.

($L = 0.5\,L^*$) spiral, ESO 157−50. Both of these galaxies have only weak Hα emission indicating very modest SFRs ($\lesssim$1 $M_\odot$ yr^{-1}). Another low-SFR object, a dwarf galaxy at $<$0.01 L^*, SDSS J103108.88+504708.7, has its halo probed by two lines of sight at two different impact parameters. These same two QSO sight lines (1ES 1028+511 and 1SAX J1032.3+5051) also probe the 0.01 L^* dwarf Magellanic spiral UGC 5740 at significantly larger impact parameters (0.6 and 0.9 R_{vir}). The remaining galaxies are probed by single sight lines and include a few late-type galaxies with much higher SFRs. Three modest starburst galaxies (M108, NGC 3511, and NGC 2611) are probed along their minor axes, while one starbursting dwarf, IC 691, had a previously detected metal-line absorber (Keeney et al. 2006) close to its minor axis, which we re-observed with COS. The very low surface brightness (LSB) galaxy UGC 4527 with a very low SFR ($\leqslant$0.001 $M_\odot$ yr^{-1}) rounds out the sample. Associated FUV absorption has been found in every case and H I + metal absorptions definitely were detected in most (10 of 17) cases. One clear LLS (log $N_{H\,I} = 18.39 \pm 0.06$) was found along the minor axis of NGC 2611; otherwise, the metal-bearing absorbers have stronger detections of higher ionization lines like Si IV and C IV. Where lower ionization metal lines were detected, C IV is generally stronger than C II and/or Si III is stronger than Si II. Only one target (PG 0832+251) possesses a *FUSE* spectrum which detects Lyβ and O VI $\lambda\lambda$1032, 1038.

While this sample was chosen to investigate the CGM gas around late-type galaxies, including galaxies with a variety of luminosities, morphologies and SFRs, it is neither a complete nor an unbiased sample. Several QSO targets were selected for observation due to being projected close to the minor axis of a moderately starbursting, disk galaxy. In these cases, the disk galaxy geometry and the sign of the absorber/galaxy velocity difference allowed the determination of whether the absorber is infalling or outflowing gas (Stocke et al. 2010). Of the three Lyα-only absorbers in the HE 0435−5304 sight line, two are constrained to be outflowing and one infalling onto ESO 157−49 (Keeney et al. 2012). The absorber associated with NGC 3511 in the PMN J1103−2329 sight line is constrained to be infalling, consistent with its low metallicity ($\sim$15% solar; see Section 4.3). Both PG 0832+251/NGC 2611 and SBS 1108+560/M 108 have absorbers whose radial velocities bracket the galaxy redshift, with the higher redshift absorbers being infalling gas (Paper II). The absorber in SBS 1122+594 is likely outflowing from the dwarf starburst IC 691 but the extinction pattern in the galaxy is too patchy to be certain of its orientation.

Table 2 contains the following information about this sample: (1) name of the QSO target; (2) name of the nearby galaxy whose CGM is probed; the heliocentric recession velocities of the absorber ($\pm$10–15 km s^{-1}; average of all species detected) in Column 3 and the galaxy ($\pm$5–10 km s^{-1}) in Column 4; (5) the impact parameter (ρ) scaled to h_{70}^{-1} kpc assuming a pure Hubble flow for galaxy recession velocities; (6) the orientation of the QSO sight line on the sky relative to the galaxy's major axis measured counterclockwise on the sky (i.e., 0° and 180° are along the major axes, while 90° and 270° are along the minor axes). No entry in this column means that the nearby galaxy has no well-defined major axis; (7) total B-band galaxy luminosity in L^* units, from SDSS model magnitudes where available, otherwise from galaxy magnitudes supplied in the NASA Extragalactic Database (NED); (8) the logarithm of the absorber neutral hydrogen column density in cm^{-2}; (9) impact parameter in units of the virial radius (R_{vir} defined by two different scaling relations; see Section 3.1) and (10) the absolute value of the absorber/galaxy velocity difference ($\lvert\Delta v\rvert$) in units of the escape velocity (v_{esc}) determined at the observed impact parameter using the galaxy mass model of Salucci et al. (2007, see Section 3.1 for further discussion). The range of values quoted in Columns 9 and 10 refers to the two different definitions

of R_{vir} described in Section 3.1. As with the impact parameter, Column 10 reports the minimum of the three-dimensional (3D) value of this quantity; it is partially correlated with the value of the impact parameter through the value of v_{esc}. Column 11 lists detected metal-line absorption seen in conjunction with this absorber. As shown in Table 2, most of the galaxies probed are sub-L^* but range from $< 0.01\ L^*$ to nearly L^* with impact parameters ranging from 0.1–1 R_{vir} in projection.

While details of the spectral analysis, line identifications, and photoionization modeling are presented elsewhere (Paper II), a summary of these results are described in Sections 4.3 and 4.4. Examples of our detailed photoionization method and its results are given in Keeney et al. (2012) for the three sight lines around ESO 157−49. Nine of the 17 CGM absorbers found in these sight lines contain metals with $\log(Z/Z_{\odot}) \approx -1$ to 0 where photoionization modeling is possible. We were surprised to find similar, high-ionization absorbing gas associated with most of the galaxies in our targeted sample.

3. THE STIS "SERENDIPITOUS" QSO/GALAXY SURVEY

3.1. The Absorber and Galaxy Samples

The 35 STIS sight lines used to define our "serendipitous" absorber sample are as presented in DS08. The STIS sample includes very bright FUV targets possessing both high-resolution 7 km s^{-1}, moderate S/N $\sim$ 5–15 STIS E140M spectra and also *FUSE* $\sim$ 20 km s^{-1} FUV spectra. DS08 analyzed 650 Lyα lines, and numerous associated metal lines spanning ionization states from C II to O VI; see DS08 for details concerning the line identifications of H I, Si III, C III, Si IV, C IV, and O VI, analyses of absorber systems, etc. The lower ionization detections and Lyman-limit decrements associated with these absorbers were added after DS08 (C. W. Danforth 2012, private communication; see also Tilton et al. 2012). Absorbers in the serendipitous sample have higher Lyman series lines as well as O VI lines detectable; i.e., O VI falls within the higher sensitivity regions of the *FUSE* detector providing detections at $\log N_{O\,VI} \geqslant 13.2$ (Danforth & Shull 2005; Stocke et al. 2006) where unobscured by Galactic absorption lines. In the current study we have used only those $\sim$500 Lyα absorbers with $\log N_{H\,I} \geqslant 13.0$ ($W_{\lambda} \geqslant 54$ mÅ), an absorber equivalent width detectable in all 35 STIS spectra (DS08). It has been known for some time (Lanzetta et al. 1995; Chen et al. 1998) that a loose correlation exists between Lyα equivalent width and nearest galaxy distance (see also Davé et al. 1999) and so the higher column density absorbers are more likely to be CGM clouds. Also Penton et al. (2002) found that at $W_{\lambda} \leqslant 54$ mÅ an increasingly larger percentage of Lyα absorbers are found in galaxy "voids," >3 Mpc from the nearest known galaxy.

The sample of $\sim$700 galaxies at $\leqslant$1 Mpc from these 35 sight lines is derived from a combined galaxy database with >1 million entries last described in Stocke et al. (2006), where it was used to investigate the galaxy environments of nearby O VI absorbers discovered by *FUSE*. Two major changes have occurred since that last use in 2006: SDSS DR4 has been replaced with SDSS DR8 (Eisenstein et al. 2011) and numerous galaxies near several of these sight lines have been cataloged in Prochaska et al. (2011a) and analyzed in Prochaska et al. (2011b). Details of the galaxy redshift database can be found in Stocke et al. (2006) and Penton et al. (2004).

Even a pointed survey for galaxies as conducted by Morris et al. (1993), McLin (2003), or Prochaska et al. (2011a) has difficulties defining a completeness limit given that both a limiting magnitude for galaxies surveyed for redshifts as well as a maximum angular size scale for target completeness must be defined. In this regard, both very nearby and very distant absorbers present distinct challenges. For distant absorbers faint limiting magnitudes (e.g., r = 19–20 for the above studies) require many galaxies to be surveyed with >90% completeness percentages at faint apparent magnitudes (percentage of galaxies at each magnitude limit for which redshifts are obtained). Further, faint galaxies are prone to misclassification. The percentage of stars observed by mistake increases with magnitude at least to $r \sim 22$ and more galaxies are not targeted due to misclassification at fainter magnitudes. However, even relatively bright galaxies can be misclassified; e.g., a 17th magnitude galaxy found to be the only one nearby to the strongest Lyα absorber in the FUV spectrum of 3C 273 was misclassified by Morris et al. (1993) and only observed after a different galaxy classifier was used to identify this object as a galaxy (see Stocke et al. 2004). Further, in a pointed survey care must be taken to ensure that no galaxies are missed for observation either by being too close on the sky to another targeted galaxy or because a galaxy falls in a sky area in between multi-object mask setups. In this respect large-angle galaxy surveys like SDSS and 2dF are excellent resources for this work simply because they have fewer edges to the surveyed areas. Also, in the absence of SDSS and/or 2dF some pointed surveys have too small a field of view to obtain complete galaxy survey spectra out to a 1 Mpc radius from a very low-z absorber. Therefore, a combination of SDSS and/or 2dF with a deeper, pointed survey is ideal, a process in which we are now engaged for all COS GTO sight lines (B. A. Keeney et al., in preparation).

For this survey we have used only those regions complete to well-defined apparent r-band magnitude limits in a circle around the sight line of radius at least 1 Mpc at the absorber's Hubble flow distance. For any absorber/galaxy association to be used statistically, the galaxy's luminosity must be greater than the completeness luminosity at its distance; i.e., a bright galaxy identified as associated with an absorber is the closest at its luminosity or higher. In this way each potentially associated galaxy with L_{gal} creates its own complete sample if all galaxies within 400 km s^{-1} and 1 Mpc of the absorber that have $L \geqslant L_{gal}$ have been observed and redshifts obtained. Only galaxy samples defined by this procedure are used for statistical purposes. To address some questions, an even more restrictive sample is used: absorbers located in regions completely surveyed for galaxies to $\lesssim$0.15 L^* (see Section 4).

In order to investigate absorber/galaxy associations for galaxies of differing luminosities, three luminosity bins are defined: (1) luminous super-L^* ($L > L^*$) galaxies, (2) sub-L^* galaxies (L = 0.1–1 L^*), and (3) dwarfs at $L < 0.1\ L^*$. Closest galaxies to absorbers are determined for each luminosity bin given the completeness constraints just described. We have used the same luminosity bins as Prochaska et al. (2011b) to facilitate easy comparisons. For the same reason, we have chosen the same "retarded velocity" as Prochaska et al. (2011b) of $\pm$400 km s^{-1}, slightly greater than the value we have used previously ($\pm$300 km s^{-1}; Penton et al. 2002). This choice means that if $|\Delta v| = |v_{abs} - v_{gal}| < 400$ km s^{-1}, the absorber and galaxy are assumed to be at the same radial distance from us. This value is only slightly greater than the rotation speed of a massive galaxy. If $|\Delta v| > 400$ km s^{-1}, a radial distance defined by the Hubble flow is assumed and the galaxy quickly attains a 3D space distance >1 Mpc from the absorber by this formulation. As reported in Penton et al. (2002), Stocke et al.

(2006), and Prochaska et al. (2011b), the exact choice of retarded velocity does not change the statistical results of this work. However, it is important to note that the galaxy recession velocities used in this study come from a variety of sources and, therefore, have a variety of accuracies; e.g., ± 10 km s^{-1} if from H I 21 cm emission profiles; ± 30 km s^{-1} if from SDSS or Prochaska et al. (2011b); and up to ± 80 km s^{-1} if from low-resolution spectroscopy obtained some time ago (e.g., McLin 2003).

Given the heterogeneous nature of the database, the magnitudes for galaxies also have some variation in accuracy and precision. Comparing magnitudes for the same galaxy from different sources, we find $\sigma \approx 0.2$ mag. In other cases magnitudes must be converted from a different color using transformations (e.g., $B = (g + 0.1) + 1.2\,(g - r)$ for SDSS model magnitudes) as described in Penton et al. (2002). The CfA galaxy luminosity function of Marzke et al. (1994) is adopted and sets $B^* = -19.57$. Given the low-z of our sample we make no evolutionary or K-correction to galaxy luminosities.

Lacking spatially resolved spectroscopy for all these galaxies, we infer total halo masses from galaxy luminosities only and then calculate a virial radius as a physical quantity determined by luminosity alone. However, when the theoretical definition of the virial radius is folded through the Tully–Fisher relationship (i.e., mass-to-light ratio as a function of luminosity), $R_{\rm vir}$ is expected to increase quite slowly with galaxy luminosity (i.e., $R_{\rm vir} \sim L^{0.3}$), so that any uncertainty in galaxy luminosity does not create a large uncertainty in virial radius. Also, the exact value of the virial radius is only indicative of the region over which the gravitation of a galaxy dominates the dynamics of gas clouds in its vicinity. Theoretical models suggest that the CGM extends to approximately the virial radius ($R_{\rm vir}$) and is enriched with metals by supernova-driven galactic winds (Stinson et al. 2012; van de Voort & Schaye 2012), which may or may not escape the galaxy's gravitational potential (escaping winds are more likely for low-mass galaxies; Côté et al. 2012). Therefore, we have used $R_{\rm vir}$ to distinguish CGM from IGM absorbers (see additional support for this statement in Section 3.2) and to place all CGM clouds into a context close to scale-free with respect to galaxy mass.

We have investigated two different prescriptions for virial mass and radius as a function of galaxy luminosity for this paper. Prochaska et al. (2011b) used an expression for the virial radius of a galaxy based on its luminosity L/L^*:

$$R_{\rm vir} = 250\,(L/L^*)^{0.2}\ {\rm kpc}. \quad (1)$$

Compared to the other estimator of virial mass and $R_{\rm vir}$ used herein, Equation (1) yields larger dynamical masses and virial radii. Adopting a "halo-matching" scheme whereby an observed galaxy luminosity function (e.g., Marzke et al. 1994; Montero-Dorta & Prada 2009) is matched with the theoretical halo mass function of Sheth & Tormen (1999), somewhat smaller values of total halo mass and $R_{\rm vir}$ are obtained. Comparisons between various estimators of halo mass and virial radius are shown in Figure 1, where Equation (1) is shown as a blue line and the observed Tully–Fisher relationship of Meyer et al. (2008) is shown in red. In black and yellow lines are results from the halo-matching schemes for the Marzke et al. (1994) B-band luminosity function and the SDSS r-band luminosity function of Montero-Dorta & Prada (2009), respectively. In both cases, a faint-end slope of $\alpha = -1.25$ is assumed to include LSB galaxies. A fourth physical size scaling of $L^{0.4}$ has been advocated by Chen et al. (2001) based only on a minimization of the spread in the observed broad correlation between W_λ(Lyα) and impact parameter. While each different scaling finds different fiducial radii for different luminosity galaxies, some scaling seems appropriate to compare the CGMs of different luminosity/halo mass galaxies.

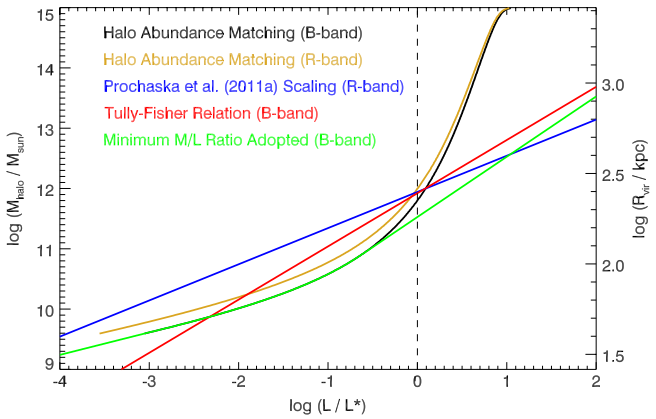

Figure 1. Comparison of various galaxy mass models as a function of galaxy luminosity alone. The primary mass model used in this paper is based on a "halo-matching" scheme (Trenti et al. 2010) in which a simulated halo abundance is matched to the B-band luminosity function of Marzke et al. (1994). At $L > L^*$ the halo matching returns enormous masses because individual halos encompass many galaxies. The green line labeled "Minimum M/L Ratio" departs from the halo matching above $L = 0.2\,L^*$, where the number of galaxies per halo begins to rapidly increase (Moster et al. 2010). We adopt this hybrid prescription for virial mass and radius, although the scaling based on Equation (1) (Prochaska et al. 2011b) is used on occasion to check the sensitivity of the results to these assumed prescriptions.

For the halo-matching schemes, $L > L^*$ galaxies are matched with much larger halo masses than either of the scaling relations shown in Figure 1 because these massive halos now encompass entire small groups of galaxies. Halos with associated stellar luminosities $L \geqslant 0.2\,L^*$ contain an increasing number of galaxies (Moster et al. 2010). Due to this multiplicity effect and in order to make a more accurate association between galaxy luminosity and mass we use the halo-matching approach below $0.2\,L^*$ and assume a constant mass-to-light ratio (50 in solar units) above that point (green curve in Figure 1). $M_{\rm halo}/L_{\rm gal} = 50\,M_\odot/L_\odot$ is also the minimum value of this quantity predicted by halo matching (Moster et al. 2010, 2012). Below $0.2\,L^*$ the halo mass-to-stellar light ratio of smaller galaxies rises significantly, as has been noted in several studies (e.g., Peeples & Shankar 2011).

In this paper we adopt the halo masses and virial radii defined by the green line in Figure 1, a "halo matching" with the CfA B-band galaxy luminosity function of Marzke et al. (1994) with $\alpha = -1.25$. Steeper faint-end slopes to the luminosity function bring the results of the halo-matching technique into close agreement with Equation (1) near L^* but fall below these scalings (i.e., Tully–Fisher and Prochaska et al. 2011a) at $L < 0.2\,L^*$. Two differences compared to Equation (1) are noted: (a) the values of the halo mass and $R_{\rm vir}$ at L^* are $\sim$20% smaller than Equation (1) and (b) the difference between these two models increases below L^* down to $\sim 0.01\,L^*$. For the present work this means that Equation (1) and the halo-matching result represent likely extremes in estimating halo masses and virial radii from total galaxy luminosities. While we have used both prescriptions to analyze the STIS serendipitous absorber–galaxy sample, in the discussion below we will present results based on the halo-matching technique, commenting on any differences which occur if Equation (1) is used.

Because the escape velocity is calculated using a Salucci et al. (2007) mass model in which the total halo mass

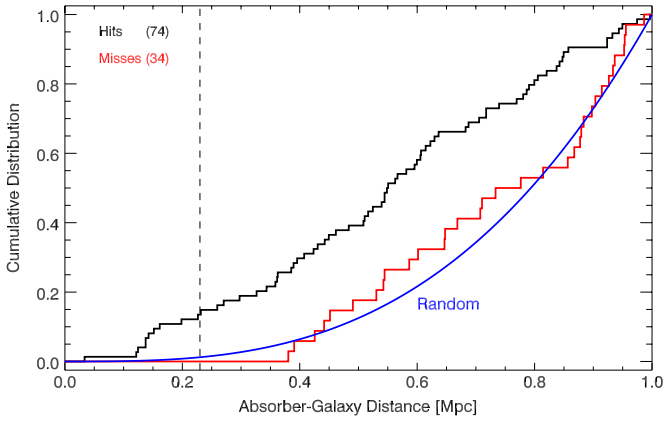

Figure 2. Cumulative distribution function of absorber–galaxy distance for the super-L^* galaxy sample with $\leqslant$1 Mpc absorber–galaxy separation. The "hits" are absorbers $\leqslant$1 Mpc from luminous galaxies while the misses are luminous galaxies $\leqslant$1 Mpc from the sight line with no absorber present at $|\Delta v| \leqslant 400$ km s^{-1}. The blue line shows the expectation for a random placement of galaxies relative to the sight line. Sample numbers are shown at upper left.

determines a core radius, the escape velocities in Tables 2–5 also depend on the adopted model from Figure 1. While a Navarro–Frenk–White (NFW) profile is somewhat "cuspier" than the Salucci et al. (2007) model we have assumed, this difference has little effect because we do not probe either the targeted or serendipitous absorber host galaxies at small enough impact parameters that the cusp/core difference is noticeable. And, because the galaxy density profile is truncated at the virial radius so that the galaxy mass does not exceed the halo mass, at $\rho > R_{\rm vir}$ there is a Keplerian falloff in $v_{\rm esc}$. Very few absorbers are affected by this assumed mass truncation.

For the galaxy sample we find that our three luminosity bins (super-L^*, sub-L^* and dwarfs) have median luminosities of (2.0, 0.45, 0.03) L^* and, from the halo matching, median halo masses and virial radii of ($10^{11.8}$, $10^{11.2}$, $10^{10.3}$) $M_\odot$ and (230, 140, 70) kpc, respectively. For comparison, based on Equation (1), the median virial radius values for the three luminosity bins are (285, 215, 125) kpc. The Milky Way has an estimated B-band luminosity midway between the median luminosities for the super-L^* and sub-L^* samples; i.e., for our Galaxy the two prescriptions yield $R_{\rm vir} = 230$ and 170 kpc from Equation (1) and from the hybrid halo-matching formalism, respectively. In general, these values should be taken as *indicative* in defining the extent of the CGM.

3.2. CGM versus IGM Absorbers

In Figure 2, we show the cumulative distribution function (CDF) of projected nearest-neighbor distances for the sample of $L > L^*$ galaxies within 1 Mpc of Lyα absorbers. While there are many more super-L^* galaxies in the full database (203) than are shown in this plot, the others are missing for good reasons. Thirty-four galaxies are >1 Mpc from any absorber, an even larger number of galaxies (83) are not included due to having another super-L^* galaxy closer, and 12 are not in regions surveyed at least to L^* completeness. None of these are plotted in Figure 2, leaving a total of 74 galaxies as "hits" (>L^* galaxies with an absorber within 1 Mpc) and 34 as "misses" (>L^* galaxies with no absorber within 1 Mpc). The nearest galaxy distance CDFs for the sub-L^* and dwarf galaxies are similar in shape to Figure 2 when scaled down in distance due to their smaller virial radii (see discussion below) but contain fewer absorber/galaxy pairs in each sample. The inferences we draw from Figure 2 are as follows.

1. Most local Lyα absorbers (>80%) are projected significantly further from the nearest bright galaxy than the estimated virial radius of that galaxy: 200–250 kpc for L^* and 230–285 kpc for 2 L^*, the median luminosity for the sample. Most absorbers are found at 2–5 virial radii (median *projected* distance ~600 kpc) from the nearest bright galaxy, about twice as far as the distance between bright galaxies in our sample (Stocke et al. 2006). We classify these absorbers as IGM, not CGM, because they cannot be assigned unambiguously to a single bright galaxy (see further discussion below).
2. Bright galaxies are more centrally concentrated around absorbers than a random distribution (probability of this distribution occurring by chance is 1 part in 10^{11} using the K-S test). On the other hand, the "misses" have a CDF consistent with a random placement relative to the absorber. The other luminosity bins exhibit the same behavior at lesser but still significant levels. The central concentration of the "hits" in Figure 2 suggests to us that while the relationship between IGM absorbers and galaxies is not close, there is a statistical connection; i.e., both galaxies and absorbers trace the same large-scale dark matter distribution (see Davé et al. 1999; Penton et al. 2002).
3. Only ~15% of the local Lyα absorbers in Figure 2 are projected close enough to bright galaxies to be potentially within the estimated virial radius. Since many other galaxies (83 + 34 in the full sample) are farther away (despite being in well-surveyed galaxy regions) the number of CGM absorbers is an even smaller percentage of the total. Of course, projection effects can only diminish the number of CGM absorbers further still. Unfortunately, this means that starting with an extremely large sample of galaxies around QSO sight lines, only a small fraction (~5%) are close enough to target sight lines to sample the CGM.
4. Given the "hits" and "misses" in Figure 2, the covering factor of warm gas as traced by Lyα absorption several virial radii from bright galaxies is ~70%, consistent with previous results (e.g., Penton et al. 2002; Stocke et al. 2006). This result is also consistent with a recent analysis by Prochaska et al. (2011b) showing that only a fraction of local Lyα absorbers at $\log N_{\rm H\,I} \geqslant 13.5$ can be accounted for as very extended (300 kpc radius), fully covered galaxy CGMs.

Using this same super-L^* sample, we can construct the CDF for the ratio of next-nearest galaxy distance to nearest galaxy distance for each absorber. This new distribution (Figure 3) has a median ratio of 1.4, meaning that for a typical absorber the next-nearest galaxy is only 40% farther away in projection from the absorber, making it problematical to assign the absorber to any one bright galaxy in many cases. Further, many of these same absorbers also have lower luminosity galaxies in close proximity, which are not accounted for in this ratio. Taking this result together with the statistics of Figure 2, we conclude that, while most local Lyα absorbers are associated with galaxies in general, a typical Lyα absorbing cloud cannot be associated unambiguously with an individual galaxy; i.e., the association is rather with galaxy filaments or groups. This is the same conclusion reached by Morris et al. (1993) and Penton et al. (2002, 2004) and also theoretically by Davé et al. (1999). Penton et al. (2002) found that ~20% of all low-z Lyα absorbers are located in galaxy voids >3 Mpc from any known galaxy; the

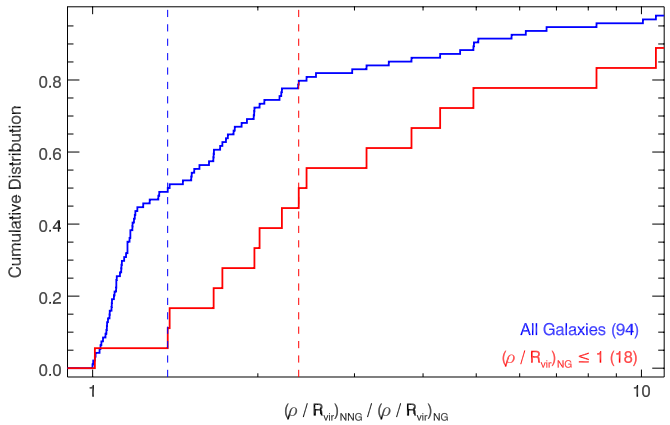

Figure 3. Ratio of next-nearest galaxy distance (ρ_{NNG}) to nearest galaxy distance (ρ_{NG}) in units of virial radii. The blue curve shows the CDF of this ratio for all galaxies $\leqslant$ 1 Mpc from the sight line, while the red curve shows only those galaxies with CGM absorbers at $\rho \leqslant R_{vir}$. The median of the blue CDF (blue dashed vertical line) shows that for all galaxy–absorber pairs the next-nearest galaxy is typically only 1.4 times farther away from the absorber than the nearest. The red dashed vertical line shows that for CGM absorbers the next-nearest galaxy is 2.4 times farther away, making the identification of a CGM absorber with a specific galaxy more unique (see Section 4.1 for further discussion). Sample numbers are shown in parentheses at lower right.

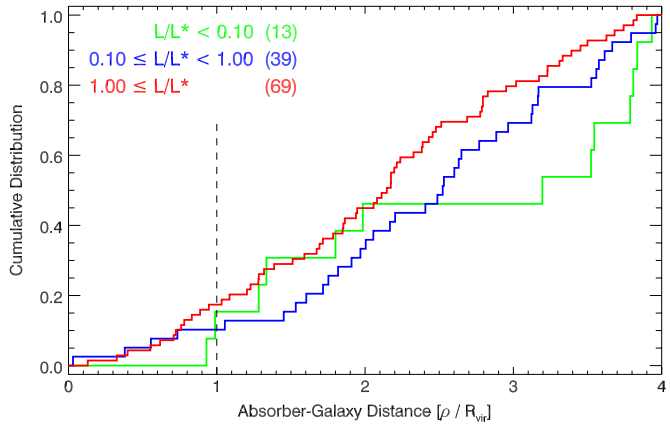

Figure 4. Cumulative distribution functions of absorber–galaxy distance for the three different luminosity bins used in this paper. While there is no strong indication of a difference between these three distributions, the statistics for the dwarfs are modest. Sample numbers are shown in parentheses at upper left.

remaining ~80% are located in galaxy filaments although not so close to any one galaxy to be considered in its CGM. The Davé et al. (1999) numerical simulations of Lyα absorbers exhibit a similar loose correlation between Lyα equivalent width and nearest galaxy distance, a correlation originally discovered observationally by Lanzetta et al. (1995). On the basis of their simulations, Davé et al. (1999) concluded that this observed correlation is consistent with a filamentary origin for most local Lyα clouds, in agreement with our assessment here.

However, if we restrict our scrutiny to just the potential CGM absorbers, the CDF shown in Figure 3 has a median ratio of ~2.4; i.e., the typical CGM absorber has a next-nearest neighbor galaxy of comparable size ~2.4 times farther away. For the small subset of Lyα absorbers that we term the CGM, there is little ambiguity concerning the galaxy associated with most absorbers (but see Section 4.1).

Figure 4 shows that the CDFs of nearest neighbor distances for all three luminosity bins exhibit similar behavior once the modest dependence on galaxy mass is removed by scaling the

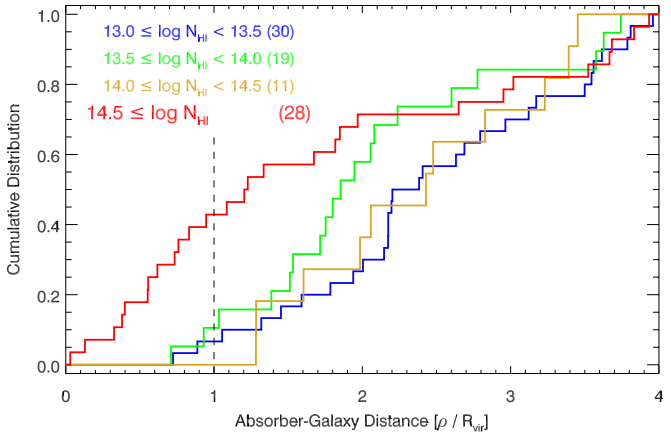

Figure 5. Cumulative distribution functions of absorber–galaxy distance for different absorber hydrogen column densities including galaxies of all luminosities. While there are a few low column density absorbers inside the virial radii of galaxies, most of the CGM absorbers, and all CGM absorbers at $\rho \leqslant 0.5\ R_{vir}$, have $\log N_{H\,I} \geqslant 14.5$. Nearly half of all high-column density absorbers are CGM absorbers. Sample numbers are shown in parentheses.

impact parameter to the virial radius of each galaxy. In Figure 4, there is a slight tendency for super-L^* galaxies to have a larger percentage of CGM versus IGM absorbers near them although this difference is not robust. If Equation (1) scaling is used, the difference in the fraction of CGM versus IGM absorbers is not statistically different between the three luminosity classes, although the number of true dwarf CGM absorbers is quite small: 2 of 13 by the halo-matching formalism and 5 of 22 by Equation (1).

However, a large difference in the column density of CGM versus IGM absorbers is evident in Figure 5 with few CGM absorbers present in this sample at $\log N_{H\,I} < 14.5$. On the other hand, 50% of all absorbers with $\log N_{H\,I} > 14.5$ are CGM, again consistent with Lanzetta et al. (1995) and subsequent work by H.-W. Chen (e.g., Chen & Mulchaey 2009). Among other things, this result means that even COS snapshot spectra (S/N < 5 per resolution element) will be sensitive enough to detect CGM absorbers given a sufficient path length per spectrum.

While we take these statistical results as ample evidence to classify an absorber as CGM if it is closer to a galaxy than the virial radius, projection effects can only decrease the number of true CGM absorbers. Given $d\mathcal{N}/dz = 50$ per unit redshift for Lyα absorbers with $N_{H\,I} \geqslant 10^{13.0}$, we expect 3–5 projected IGM absorbers in our combined targeted + serendipitous CGM absorber sample (see Section 4.4). Those absorbers with $N_{H\,I} < 10^{14.5}$ are most likely to be projected IGM absorbers misclassified as CGM. An example of this distinction is the pair of absorbers detected at very low-z in the COS spectra of 1ES 1028+511 and 1SAX J1032.3+5051 presented in Table 2 (see Paper II for a full discussion). An absorber in the 1ES 1028+511 sight line is detected 27 km s^{-1} and half of a virial radius away from an $M_r \approx -14.0$ post-starburst dwarf galaxy. But absorption near this velocity is not detected in the other QSO sight line 33 kpc away from the first sight line and at $\sim R_{vir}$ from the dwarf. However, a second absorber at $|\Delta v| = 79$ km s^{-1} is detected at comparable equivalent width in both sight lines and so is at least 33 kpc in extent. We identify the higher column density absorber as CGM and the latter (detected twice) as a single projected IGM absorber, associated with a large-scale gaseous filament in this region. Therefore, while the

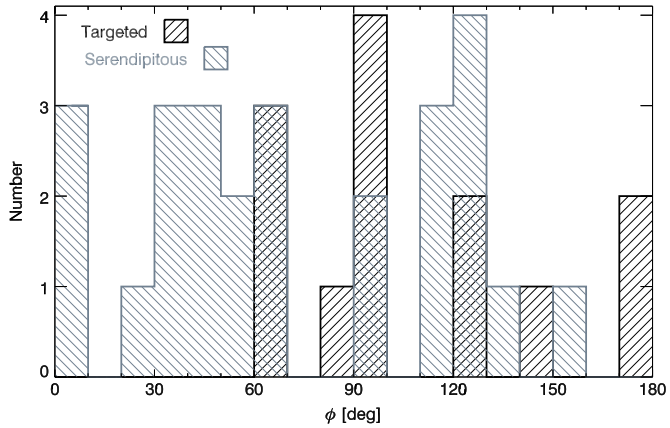

Figure 6. Position angle distribution for targeted (black outlined histogram shaded with back-slashes) and serendipitous (gray outlined histogram shaded with forward slashes) CGM absorbers, where such data are available through NED. The position angle is measured from the galaxy to the absorber relative to the galaxy's major axis. Thus, $\phi = 0°$ and $180°$ are along the major axis and $\phi = 90°$ is along the minor axis. QSO/galaxy pairs are plotted only when a well-defined disk is present, for which position angles are quoted in NED or SDSS. Because several of the COS-targeted QSO/galaxy pairs were selected to be along the minor axis, the serendipitous sample is more randomly chosen with respect to galaxy orientation.

CGM sample must include some projected IGM absorbers, it is likely that most of these are at $N_{\rm H\,I} \leqslant 10^{14}$.

3.3. The Covering Factor of the CGM and the Filamentary IGM in Warm Gas

In Section 2.1 we found that at least one Lyα absorber is detected for each galaxy CGM targeted by our COS spectra regardless of galaxy luminosity, implying a very high covering factor of CGM gas out to approximately the virial radius. Low- and high-ionization metal-line absorptions were usually but not always found associated with these CGM Lyα absorbers (10 out of 17 absorbers; see Table 2). Similarly, Tumlinson et al. (2011) found a very high covering factor of O VI-absorbing gas in the CGM of a large sample of low-z, $L > L^*$ late-type galaxies. However, to avoid any possibility of selection bias in either our targeted sample or in the SDSS galaxy sample of Tumlinson et al. (2011) influencing the covering factor, we employ the CGM serendipitous sample to determine covering factors. Evidence for some bias in the selection of the COS-targeted sample is shown in Figure 6, a plot of absorber location relative to the proximate galaxy's major axis. Several of the QSO targets were chosen to probe gas along the minor axis of a starburst or dwarf starburst galaxy. The subset of serendipitous absorbers found near galaxies with good determinations of disk position angle on the sky shows no obvious orientation preference with respect to the nearby galactic disk.

Figure 7 shows the covering factor of Lyα absorbing gas as a function of projected absorber/galaxy distance in units of virial radii for the three luminosity bins used in our serendipitous sample. These values were computed using the ratio of "hits" to ("hits" + "misses") where "hits" are absorber/galaxy matches within ± 400 km s^{-1} in radial velocity and within the bin of scaled impact parameter on the abscissa. The full list of 172 "hits" comes from DS08, while the 147 "Misses" are galaxies within each impact parameter bin with no associated Lyα absorber (i.e., at $|cz_{\rm abs} - cz_{\rm gal}| = |\Delta v| \leqslant 400$ km s^{-1} and $\log N_{\rm H\,I} \geqslant 13.0$). Because Galactic absorption lines can obscure the presence of Lyα absorption, we have excluded portions of the STIS spectra around the strong Galactic absorption lines: S II $\lambda\lambda$1250.6, λ1253.8, and λ1259.5; Si II λ1260.4; O I λ1302.2; Si II λ1304.4; C II λ1334.5; C II* λ1335.7; and Si IV λ1393.8 and λ1402.8. While other strong Galactic absorption occurs longward of 1450 Å, any Lyα obscured by those transitions would be at a higher redshift than the $z \leqslant 0.2$ limit imposed by this survey. Only 10 of 157 "misses" are excluded from the sample on this basis. Errors in the Figure 7 histogram are computed from sample size Poisson statistics (Gehrels 1986) and are shown as color-shaded regions in each bin.

Given the sizes of the Poisson errors, all three galaxy luminosity bins possess similar CGM area covering factors as a function of impact parameter once scaled by $R_{\rm vir}$. Within the virial radius the super-L^* and sub-L^* samples possess covering factors (C) consistent with $C = 1$ for the inner half virial radius and $C = 0.75$ for $0.5 \leqslant (\rho/R_{\rm vir}) \leqslant 1.0$. Because the galaxy surveys available to us become incomplete for $L < 0.1\,L^*$ at $cz > 5000$ km s^{-1}, the covering factor statistics for the dwarf sample are poor. So while the covering factor around dwarfs may be smaller than for more luminous galaxies, the available statistics do not support this conclusion at high confidence; more data are needed. The detection of Lyα absorption around all five dwarfs in the COS-targeted sample supports a high CGM covering factor of Lyα absorption for dwarfs within the virial radius.

For our first attempt at modeling the "warm" ($T \sim 10^4$ K) CGM gas, based on Figure 7 we will assume that super-L^* and sub-L^* galaxies have the same high values of covering factors mentioned above and dwarfs have $C = 0.50$ inside the virial radius.

3.4. The Extent of Hotter Gas around Galaxies

Since many O VI absorbers are found well beyond the virial radii of galaxies, to maximum impact parameters of $\sim$3.5 $R_{\rm vir}$ ($\sim$800 kpc for super-L^* galaxies and $\sim$450 kpc for sub-L^* galaxies; Stocke et al. 2006), this metal-bearing gas must be patchy. Figure 7 shows that only $\sim$60% of the sight lines that pass through regions at 1–4 $R_{\rm vir}$ have detectable Lyα absorption. From Figure 1 in Stocke et al. (2006), only $\sim$50% of these Lyα absorbers have detectable O VI at these distances for a total O VI covering factor of $\sim$30%. Once impact parameters are scaled to virial radii, there is little difference between the covering factors we find for the super-L^* and sub-L^* samples. As with the Lyα absorption, we are less certain about the dwarfs since the sample of O VI absorbers associated with dwarfs is very small. Neither the previous Stocke et al. (2006) study, the recent Prochaska et al. (2011b) study, nor the current accounting use O VI absorber samples which do *not* have associated Lyα absorption. While indications are that the number of such systems are small (DS08), the nature of these O VI-only absorbers and their relationship to the much more common Lyα + O VI systems is not yet clear (although see Savage et al. 2010, and Section 5.1 herein for a description of one important O VI-only system).

If we assume a near unity covering factor in O VI-absorbing gas around star-forming galaxies of all luminosities *inside* $R_{\rm vir}$ (consistent with the new Tumlinson et al. 2011 pointed survey) and a 30% covering factor from 1 to 3.5 $R_{\rm vir}$ found here, then a total $d\mathcal{N}/dz \approx 20$ per unit redshift interval for O VI absorbers at $\log N_{\rm O\,VI} \gtrsim 13.2$ (DS08; Tilton et al. 2012) can be obtained only if all three galaxy luminosity bins contribute significantly to the total cross-section. Tumlinson & Fang (2005) found a similar result.

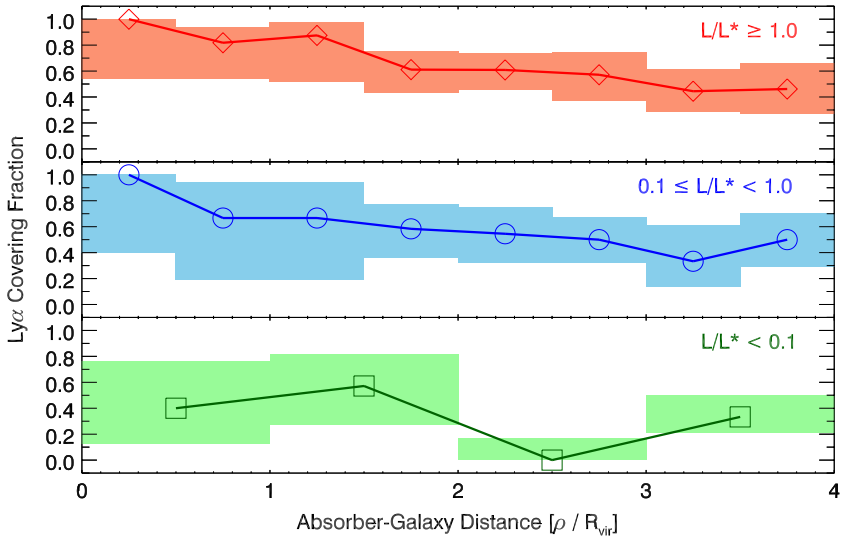

Figure 7. Covering fraction (C) of Lyα-absorbing gas for galaxies of various luminosities, where C ="hits"/("hits" + "misses"). The shaded regions are the Poisson errors for each bin. The super-L^* and sub-L^* samples have statistically indistinguishable covering factor distributions. While the dwarfs appear to have somewhat lower covering factors, the statistics are too meager for that sample to be certain.

(A color version of this figure is available in the online journal.)

This result differs from the assessment of Prochaska et al. (2011b) who claim that a ∼100% covering factor around sub-L^* galaxies out to 300 kpc (1.5–2 virial radii) can account for all O VI absorbers in the low-z universe. The difference between these two conclusions appears to be the assumed value of the covering factor. While we find no evidence for covering factors near unity like Prochaska et al. (2011b) assumed, the numbers of absorbers in these samples are still modest. The Stocke et al. (2006) sample of O VI absorbers in regions surveyed for galaxies to at least 0.1 L^* contains only 17 Lyα absorber data points (9 O VI detections and 8 non-detections). Using the current galaxy database, which is only slightly enlarged from Stocke et al. (2006), we have increased the O VI sample near sub-L^* galaxies to 9 detections and 10 non-detections with no statistically significant change in covering factor from our previous result. A maximum spread of metals around galaxies of ∼3.5 $R_{\rm vir}$ is also confirmed, except that we find one new O VI absorber at ∼5 $R_{\rm vir}$ (see Section 4.2). Deeper ($r \sim 22$–23) galaxy survey work close to each absorber sight line is required to reconcile the somewhat differing conclusions concerning O VI absorption.

4. THE MERGED SAMPLE OF TARGETED PLUS SERENDIPITOUS CGM ABSORBERS

4.1. Defining the Serendipitous CGM Absorbers

In Table 3, we list the basic properties of the close, serendipitous QSO/galaxy pairs obtained from the STIS/*FUSE* QSO sample of DS08 and the combined galaxy redshift database. This table includes all pairs in our complete samples (defined in Section 3.1) projected closer than 1.5 $R_{\rm vir}$ and includes the following information by column: (1) target of the STIS/*FUSE* spectroscopy; (2) nearest foreground Galaxy probed by this sight line; (3) and (4) the recession velocities of the absorber and galaxy. While the STIS absorber velocities are accurate to a few km s^{-1}, the galaxy velocities have poorer and variable accuracies depending upon the source of the redshift (see Section 3.1); (5) the impact parameter of the QSO absorber/galaxy pair in kpc; (6) the galaxy luminosity in L^* units; (7) the completeness limit galaxy luminosity in L^* units for the galaxy redshift survey in and around that sight line at the absorber distance; (8) the range of impact parameter values in units of the virial radius as defined by the "halo-matching" scheme (larger number) described in Section 3.1 and by Equation (1) (smaller number); (9) the range of absorber/galaxy relative velocities in units of the escape velocity ($v_{\rm esc}$) obtained assuming the range of virial radii used for the values in Column 8. Projection effects require that the values in Columns 8 and 9 are lower limits on the 3D galaxy–absorber distance and relative velocity in all cases. The galaxy chosen in each case as nearest is that object which is the smallest number of virial radii away from the absorber (see discussion below). The final column lists associated metal absorption species detected.

Notice that there are very few pairs at $\leqslant 0.5\ R_{\rm vir}$ but many at $0.5\ R_{\rm vir} \leqslant \rho \leqslant 1.5\ R_{\rm vir}$, which makes this serendipitous sample a good complement to the COS-targeted sample described in Section 2. Although the targeted sample contains very few luminous galaxies, this sample contains quite a few (17 at $L \geqslant L^*$), again making the sum total sample quite diverse with respect to galaxy luminosity and impact parameter. These absorbers are located relatively isotropically around their nearest associated galaxy and at $N_{\rm H\,I} > 10^{14.5}$ as shown in Figure 6.

We have included pairs projected out to 1.5 virial radii to ensure that we do not miss any potential absorber associated with an individual galaxy's CGM because the dividing line between CGM and IGM absorbers is somewhat arbitrary. To address this concern, we have used the scaling of Equation (1) to identify an alternative CGM sample including all absorber/galaxy pairs separated at $\leqslant 1.5\ R_{\rm vir}$. The sample presented in Table 3 and this new alternative CGM sample are largely the same, but because Equation (1) yields virial radii ∼20% larger than the halo-matching formalism for most galaxy luminosities, Table 4 lists 18 potential CGM absorber/galaxy pairs in this alternative sample not listed in Table 3 (i.e., the alternative sample includes all absorbers in Tables 3 and 4). The columns in Table 4 supply the same information as in Table 3. All but two (the first two entries) have impact parameters $\rho > R_{\rm vir}$ by the Equation (1) scaling and only 3/18 have unambiguous metal-line detections.

Table 3
Serendipitous CGM Absorber Sample

Target	Galaxy	cz_{abs} (km s^{-1})	cz_{gal} (km s^{-1})	ρ (kpc)	L_{gal} ($L*$)	L_{lim} ($L*$)	log $N_{H\,I}$	ρ/R_{vir}	$\lvert\Delta v\rvert/v_{esc}$	Associated Metals
3C 273	SDSS J122815.96+014944.1	1015	911	69	0.008	0.002	14.23 ± 0.02	0.73–1.26	1.4–3.1	O VI?
3C 273	SDSS J122950.57+020153.7	1585	1775	80	0.015	0.004	15.38 ± 0.34	0.74–1.32	2.2–5.2	C II, Si II/III
H 1821+643	J182202.6+642139	36324	36436	156	2.0	1.2	14.17 ± 0.08	0.54–0.68	0.43–0.59	
		36415					13.81 ± 0.16		0.080–0.11	
		36632					13.13 ± 0.03		0.75–1.0	
Mrk 335	J000529.1+201336	1957	1960	96	0.047	0.006	13.99 ± 0.10	0.71–1.30	0.027–0.066	
		2275					13.24 ± 0.06		2.8–7.0	
PG 0953+414	SDSS J095638.90+411646.1	42667	42759	434	6.7	2.8	13.68 ± 0.14	1.18–1.26	0.39–0.43	O VI, C III
		42756					13.35 ± 0.03		0.013–0.014	O VI, C III
PG 1116+215	SDSS J111905.51+211733.0	17698	17993	131	0.12	0.11	13.53 ± 0.02	0.80–1.42	2.3–5.5	O VI
		17774					13.0:		1.7–4.1	O VI, N V, C IV, Si III
		18226					13.21 ± 0.04		1.8–4.3	
PG 1116+215	SDSS J111906.68+211828.7	41521	41428	138	2.9	0.57	16.35 ± 0.10	0.45–0.53	0.31–0.39	O VI, C II/III, Si II/III/IV
PG 1211+143	IC 3061	2130	2317	108	0.19	0.008	13.42 ± 0.03	0.60–1.03	1.2–2.6	O VI
PG 1211+143	SDSS J121409.55+140420.9	15302	15309	136	1.9	0.081	15.67 ± 0.35	0.48–0.60	0.026–0.036	O VI?, N V, C III/IV, Si II/III/IV
		15425					14.13 ± 0.11		0.43–0.59	
		15605					13.58 ± 0.04		1.1–1.5	
PG 1211+143	SDSS J121413.94+140330.4	19329	19334	71	0.16	0.13	15.17 ± 0.10	0.41–0.72	0.028–0.062	O VI, C III/IV, Si III
		19467					13.82 ± 0.05		0.75–1.6	O VI, C III/IV
PG 1216+069	SDSS J121930.86+064334.4	24125	24116	500	6.4	0.19	13.87 ± 0.28	1.38–1.48	0.042–0.047	
PG 1216+069	SDSS J121923.43+063819.7	37091	37204	92	0.77	0.46	14.75 ± 0.04	0.39–0.55	0.46–0.75	O VI?, C III, Si II
PG 1259+593	SDSS J130207.44+584153.8	686	662	58	0.019	<0.001	13.83 ± 0.24	0.51–0.92	0.23–0.53	O VI
PG 1259+593	SDSS J130101.05+590007.1	13808	13862	136	1.0	0.29	15.51 ± 0.28	0.54–0.75	0.24–0.37	O VI, C III/IV, Si III
		13940					14.75 ± 0.38		0.34–0.54	O VI, N V, C III/IV, Si III
PHL 1811	SDSS J215456.65−091808.6	15430	15453	266	3.0	0.09	13.79 ± 0.02	0.85–1.01	0.098–0.13	
PHL 1811	2MASS J21545996−0922249	24222	24223	35	2.9	0.21	18.00 ± 0.50	0.11–0.14	0.002–0.003	C II/III/IV, Si II/IV
PHL 1811	J215506.5−092326	39661	39758	226	2.4	0.57	14.67 ± 0.19	0.76–0.93	0.41–0.55	O VI, C III
PHL 1811	J215454.9−092331	52926	52793	351	6.1	1.0	14.87 ± 0.03	0.98–1.05	0.53–0.59	O VI, Si III/IV
PKS 0405−123	2MASX J04080654−1212494	24394	23990	414	6.0	0.19	13.76 ± 0.02	1.16–1.25	1.7–2.0	
PKS 0405−123	2MASX J04075411−1214493	28950	28989	375	5.5	0.27	14.64 ± 0.12	1.07–1.17	0.17–0.19	O VI
		29127					13.32 ± 0.09		0.58–0.67	
PKS 0405−123	J040743.9−121209	45378	45718	195	3.5	0.69	13.17 ± 0.07	0.61–0.71	1.2–1.5	C II?, Si II?
		45624					13.46 ± 0.03		0.34–0.42	
PKS 0405−123	J040751.2−121137	50105	50065	116	8.8	0.82	16.45 ± 0.07	0.30–0.31	0.094–0.098	O VI, N V, C II/III, Si II/III/IV
PKS 1302−102	NGC 4939	3447	3110	295	6.4	0.39	13.31 ± 0.07	0.81–0.87	1.2–1.3	
PKS 1302−102	2MASX J13052026−1036311	12567	12759	225	3.4	0.058	13.01 ± 0.12	0.71–0.82	0.74–0.92	
		12665					14.83 ± 0.17		0.36–0.45	O VI, C IV, Si II/III/IV
PKS 1302−102	2MASX J13052094−1034521	28176	28304	350	4.2	0.29	14.95 ± 0.06	1.05–1.20	0.57–0.69	
		28435					17.10 ± 0.40		0.58–0.71	O VI?, C II/III, Si II/III/IV
PKS 2155−304	2MASX J21584077−3019271	16965	17005	421	6.3	0.097	14.48 ± 0.28	1.17–1.25	0.17–0.19	
		17109					14.04 ± 0.01		0.45–0.50	O VI
Q 1230+011	SDSS J123047.60+011518.6	23399	23585	54	0.47	0.18	15.06 ± 0.40	0.25–0.38	0.72–1.3	O VI?, C III/IV, Si III/IV?

Note. Associated metal line information is taken from Danforth & Shull (2008).

Table 4
Alternate CGM Absorber Sample

Target	Galaxy	cz_{abs} (km s^{-1})	cz_{gal} (km s^{-1})	ρ (kpc)	L_{gal} ($L*$)	L_{lim} ($L*$)	log $N_{H\,I}$	ρ/R_{vir}	$\lvert\Delta v\rvert/v_{esc}$	Associated Metals
3C 351	SDSS J170615.84+604218.8	3465	3581	172	0.24	0.020	13.52 ± 0.05	0.92–1.52	0.85–1.8	
		3597					13.66 ± 0.03		0.12–0.25	
Mrk 876	NGC 6140	932	910	180	0.23	0.018	14.46 ± 0.13	0.97–1.62	0.17–0.36	O VI?, Si III
PHL 1811	SDSS J215517.30−091752.0	22032	21951	497	4.7	0.17	14.37 ± 0.41	1.46–1.63	0.41–0.49	Si III/IV
PHL 1811	J215447.5−092254	23310	23278	307	0.85	0.20	14.94 ± 0.08	1.27–1.78	0.21–0.36	C II/III/IV, Si III
		23632					14.76 ± 0.15		2.4–4.0	
PHL 1811	J215450.8−092235	23694	23623	235	0.30	0.20	14.65 ± 0.11	1.20–1.93	0.57–1.2	
PKS 0312−770	J031201.7−765517	17824	17792	237	0.27	0.14	13.53 ± 0.03	1.23–2.02	0.27–0.56	
PKS 0312−770	J031158.5−764855	35466	35732	378	1.6	0.56	14.17 ± 0.04	1.38–1.78	1.6–2.4	
		35813					13.79 ± 0.02		0.50–0.74	
PKS 2155−304	ESO 466−032	4989	5126	320	1.5	0.012	13.43 ± 0.02	1.18–1.54	0.79–1.2	
		5098					13.56 ± 0.02		0.16–0.24	
		5166					13.21 ± 0.03		0.23–0.34	
PKS 2155−304	J215846.5−301738	20330	20226	330	0.61	0.14	13.07 ± 0.03	1.46–2.14	0.80–1.4	
PKS 2155−304	J215845.1−301637	31633	31887	399	2.0	0.33	14.12 ± 0.18	1.39–1.75	1.5–2.1	
		31736					13.47 ± 0.03		0.89–1.3	
Q 1230+011	SDSS J123103.89+014034.4	1489[a]	1136	119	0.022	0.003	13.62 ± 0.05	1.02–1.85	4.4–11	
Ton 28	SDSS J100618.16+285641.9	1067	1362	166	0.083	0.003	14.02 ± 0.06	1.09–1.97	2.9–7.1	

Notes. Associated metal line information is taken from Danforth & Shull (2008).
[a] This absorber is located near the galaxy group CGCG 014−054, of which the listed galaxy is the closest member.

Using these additional two $\rho < R_{vir}$ absorber/galaxy pairs in the analyses below does not alter the conclusions we derive by using the sample defined by "halo matching."

How unique are the host galaxy identifications given in Tables 3 and 4? There are two aspects to this question. First, an identification would be ambiguous if a different definition of virial radius caused a different galaxy to be identified as the host galaxy. The entries in Table 4 show that this is not the case because there is no individual absorber which has different galaxies listed as associated in Tables 3 and 4. But a second aspect of this issue is not addressed by comparing Tables 3 and 4; viz., are there other galaxies comparably close to the identified host galaxy but only slightly further away? Particularly since galaxies are almost always found in groups or clusters, other comparably close galaxies could be present in some cases. While it was shown in Figure 3 that the next-nearest galaxy to a CGM absorber is typically 2.4 times farther away, there are a few next-nearest neighbors substantially closer. Table 5 addresses this other aspect of the uniqueness issue by listing all those next-nearest galaxies potentially associated with absorbers by being <1.5 virial radii away. In some cases, this "next-nearest" galaxy is actually slightly closer physically to the absorber but farther away in number of virial radii; e.g., the Table 5 entry for the absorbers in the PKS 0405−123 sight line is a much less luminous galaxy than the one listed for these absorbers in Table 3.

Two groups of absorbers have multiple entries in Table 5 indicating a small group of galaxies close to those absorbers: PG 1211+143 at cz = 15,302, 15,425, and 15,695 km s^{-1} (Tumlinson et al. 2005) and PG 1259+593 at cz = 13,808 and 13,940 km s^{-1} (Richter et al. 2004). In both of these cases, the Lyα absorption is strong and complex and the *FUSE*-detected O VI absorption is significantly broader than predicted by the H I and lower ionization metal lines. Also in both cases the nearest galaxy we have listed in Table 3 is classified by the SDSS as an early-type system based on the color discriminator advocated by Strateva et al. (2001), which uses an SDSS color cut at $(u - r) = 2.22$. The presence of late-type galaxies comparably close to the sight line means that even the two early-type galaxies potentially associated with CGM absorbers are not unambiguous associations. The only other early-type galaxy association in Table 3 is in the PG 1116+215 sight line at cz = 41,521 km s^{-1}, a 3 L^* Sa type galaxy 138 kpc from the sight line. However, the galaxy survey in this direction is complete only to 0.6 L^* at that distance and there are several late-type galaxies closer to the QSO but which lack redshifts at this writing. In a recent paper from the "COS/Halos" Team, Thom et al. (2012) report the detection of Lyα absorption in 12 of 16 early-type galaxies, classified as such by their low specific SFR (Thom et al. 2012; Werk et al. 2012). However, just as with the examples above, Thom et al. (2012) admit that their fields have not been uniformly surveyed for galaxies at lower luminosities. While the evidence for warm gas absorption around early-type galaxies is strongly suggested by their observations, we contend that the source and fate of that gas is still uncertain. Deeper galaxy spectroscopy and further investigation of the absorption associated with small groups of galaxies is necessary and important to resolve this question.

From this analysis we conclude that (1) the unique identification between an absorber and its host galaxy is reasonably robust; (2) there is no compelling evidence for warm CGM clouds in early-type galaxies, consistent with earlier work by Chen et al. (2010) and Tumlinson et al. (2011) but at variance with Thom et al. (2012); and (3) small groups of galaxies contain complex absorbers in which the O VI absorption appears broader than its associated Lyα and lower ionization metal lines would predict. In the targeted sample the galaxies NGC 2611 (PG 0832+251 sight line) and NGC 3511 (PMN J1103−2329 sight line) have other nearby, lower-luminosity galaxies at comparable impact parameters (Paper II). The absorbers at the redshifts of these galaxies have multiple velocity components, and the one target that has (admittedly poor) *FUSE* spectroscopy contains strong O VI absorption. Complex, multi-phase gas may be a hallmark of spiral-rich groups of galaxies; e.g., see also a detailed

Table 5
Absorbers Possibly Associated with Galaxy Groups

Target	Galaxy	cz_{abs} (km s^{-1})	cz_{gal} (km s^{-1})	ρ (kpc)	L_{gal} ($L*$)	L_{lim} ($L*$)	ρ/R_{vir}	$\lvert\Delta v\rvert/v_{esc}$	χ_{ph}[a]	χ_{vir}[b]
3C 273	SDSS J123103.89+014034.4	1015	1105	168	0.022	0.002	1.44–2.61	1.3–3.2	2.43	2.04 ± 0.80
3C 273	NGC 4420	1585	1693	288	0.59	0.004	1.28–1.89	0.78–1.4	3.60	1.54 ± 0.52
3C 351	NGC 6292	3465	3411	301	0.70	0.020	1.29–1.86	0.38–0.65	1.75	1.29 ± 0.39
		3597						1.3–2.3		
PG 1116+215	SDSS J111905.34+211537.7	17698	17697	256	1.1	0.11	1.01–1.37	0.006–0.009	1.95	1.07 ± 0.34
		17774						0.44–0.69		
PG 1211+143	NGC 4189	2130	2115	333	0.91	0.002	1.36–1.89	0.10–0.17	3.33	2.15 ± 0.66
PG 1211+143	SDSS J121407.36+140924.8	15302	15290	398	5.3	0.081	1.14–1.26	0.053–0.061	2.93	2.22 ± 0.27
		15425						0.59–0.69		
		15605						1.4–1.6		
PG 1211+143	SDSS J121406.93+140437.9	15302	15586	180	0.19	0.081	1.00–1.72	2.3–5.1	1.32	2.52 ± 0.72
		15425						1.3–2.9		
		15605						0.15–0.34		
PG 1211+143	SDSS J121419.88+140509.8	19329	19259	149	1.2	0.13	0.58–0.77	0.30–0.46	2.10	1.19 ± 0.37
		19467						0.90–1.4		
PG 1259+593	SDSS J130033.95+585857.2	13808	13794	320	3.8	0.29	0.98–1.13	0.061–0.075	2.35	1.64 ± 0.29
		13940						0.64–0.79		
PG 1259+593	SDSS J130100.56+585804.7	13808	13854	235	1.2	0.29	0.91–1.22	0.24–0.38	1.73	1.65 ± 0.36
		13940						0.46–0.71		
PG 1259+593	SDSS J130022.13+590127.2	13808	13926	358	1.3	0.29	1.36–1.81	0.75–1.2	2.63	2.46 ± 0.53
		13940						0.089–0.14		
PHL 1811	J215516.5−092408	22032	22112	341	0.67	0.18	1.48–2.14	0.61–1.06	0.69	1.17 ± 0.22
PHL 1811	J215450.8−092235	23310	23623	235	0.30	0.20	1.20–1.93	2.5–5.1	0.77	1.03 ± 0.29
		23632						0.072–0.15		
PHL 1811	2MASX J21545868−0923057	24222	24103	89	3.8	0.21	0.27–0.31	0.32–0.38	2.54	2.80 ± 0.41
PKS 0405−123	J040758.0−121225	28950	28916	264	0.67	0.27	1.14–1.65	0.23–0.40	0.70	1.25 ± 0.23
		29127						1.4–2.5		
PKS 1302−102	J130525.6−103923	12567	12579	313	0.65	0.058	1.37–1.99	0.088–0.16	1.39	2.20 ± 0.43
		12665						0.63–1.1		
Q 1230+011	NGC 4517	1489[c]	1128	345	1.0	<0.001	1.38–1.90	2.4–3.9	2.90	1.14 ± 0.38

Notes. Associated metal line information is taken from Danforth & Shull (2008).
[a] The ratio of the impact parameter (in kpc) of the tabulated galaxy to that of the nearest galaxy (see Tables 3 and 4): $\chi_{ph} \equiv \rho/\rho_{NG}$.
[b] The ratio of the impact parameter (in virial radii) of the tabulated galaxy to that of the nearest galaxy (see Tables 3 and 4): $\chi_{vir} \equiv (\rho/R_{vir})/(\rho/R_{vir})_{NG}$.
[c] This absorber is located near the galaxy group CGCG 014−054, of which the listed galaxy is the second-closest member.

discussion of the $cz = 50{,}105$ km s^{-1} absorber in the PKS 0405−123 sight line (Table 3) in Prochaska et al. (2004), Savage et al. (2010), and Section 5.1.

4.2. Characterizing the Merged CGM Absorber Sample

Figure 8 combines the targeted and serendipitous absorber samples to provide the most numerous warm CGM cloud sample outside the Milky Way. In this plot of the basic observables, impact parameter, and absorber/galaxy radial velocity difference, colored symbols mark metal-bearing absorbers, while empty symbols are absorbers having no detected metal lines. Red filled symbols indicate the presence of low- and high-ionization metal lines like C II, Si III, and/or C IV found within the *HST*/STIS or *HST*/COS bandpasses. The blue filled symbols indicate those absorbers which contain only O VI λλ1032, 1038 and/or C III λ977 without the metal ions found in the *HST* bandpass; i.e., these absorbers have only *FUSE* bandpass metal absorption detected. Absorbers containing both *HST* bandpass metal ion absorption and also O VI are colored red. We make this distinction because the COS-targeted absorbers do not have *FUSE* spectra to search for associated O VI. Absorbers for which available data are inconclusive as to the presence of metals in the *HST* bandpass (poor S/N at the redshifted wavelengths of Si II, Si III, Si IV, C II, and/or C IV, or the wavelengths of these absorptions are not covered by available spectroscopy) are represented by symbols with question marks. Therefore, the dividing line between "metal-bearing" and "Lyα-only" absorbers is poorly defined in this sample due to the modest S/N of the STIS spectra, the availability of *FUSE* spectra, the absorber $N_{H\,I}$ value and the physical cloud conditions. In both parts of Figure 8, the squares indicate COS-targeted absorbers and the circles are the STIS serendipitous absorbers. The size of the symbols indicates the luminosity of the host galaxies with the largest symbols being $L > L^*$, the intermediate size symbols being sub-L^*, and the smallest symbols being absorbers associated with dwarfs. This plot is limited to absorbers at $\rho \leqslant 1.5\ R_{vir}$ using the halo-matching definition of the virial radius (i.e., absorbers in Tables 2 and 3 only).

Figure 9 shows a variation on the now-standard plot of impact parameter versus Lyα equivalent width first described by Lanzetta et al. (1995) and further investigated by Chen et al. (2001) and Chen & Mulchaey (2009). On this compressed scale the loose correlation between hydrogen line strength and projected distance from the nearest galaxy is not so obvious. Inside 0.5 R_{vir} there is little decline in W_λ with distance perhaps because at these small galaxy–absorber separations the 3D distances are dominated by projection effects. Outside 0.5 R_{vir} there is also no obvious correlation but a much larger spread in $N_{H\,I}$, although the range of impact parameters is small. More

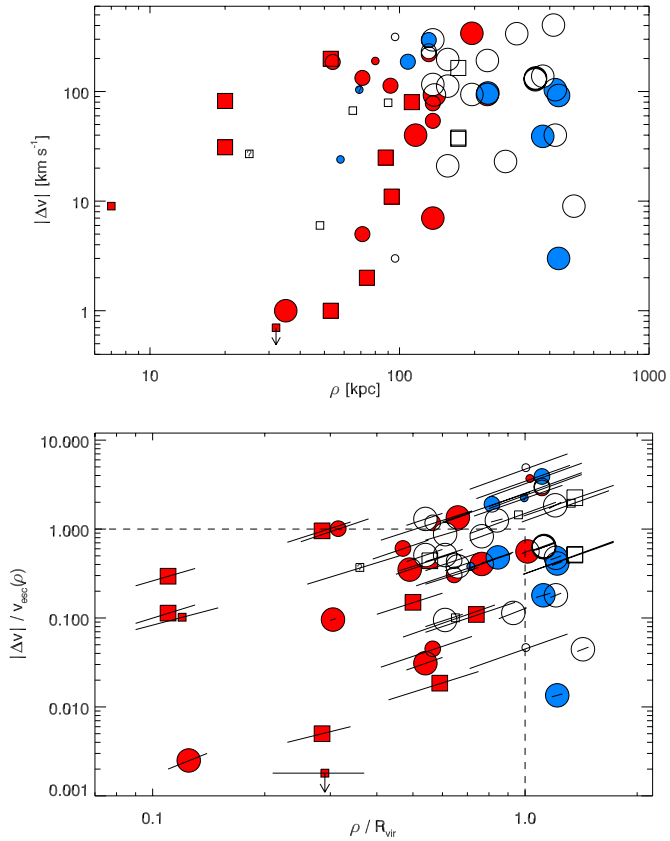

Figure 8. Distribution of CGM absorbers in impact parameter and absorber–galaxy radial velocity difference. The squares come from the COS-targeted sample and the circles are from the STIS-serendipitous sample. Filled symbols are metal-bearing absorbers, open symbols are Lyα-only absorbers. Red symbols have metal lines detected in the *HST*/STIS and *HST*/COS bandpasses, while blue circles are absorbers with O VI or O VI + C III metal absorption only detected in the *FUSE* bandpass. Absorbers with both O VI and *HST* bandpass metal lines are coded red. Symbol size encodes the host galaxy luminosity bin; largest symbols are from the super-L^* sample; intermediate size from the sub-L^* sample and dwarfs are the smallest symbols. The diagonal lines indicate the change in location in the plot by adopting a different virial radius prescription with the lower left end using the Equation (1) scaling and upper right end from the halo-matching prescription.

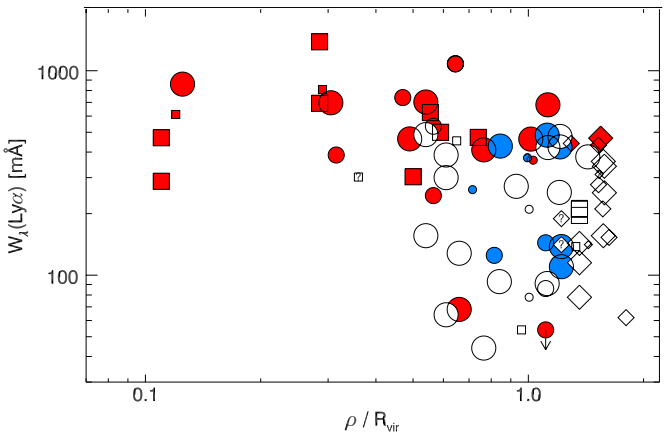

Figure 9. Plot of Lyα equivalent width vs. normalized impact parameter in units of the virial radius. As in Figure 8 the absorbers with metal ions detected in the *HST* band (e.g., Si II, Si III, and Si IV) are red filled symbols, absorbers in blue contain metals (O VI or C III) detected only in *FUSE* spectra, and unfilled symbols have Lyα-only detections. Symbols with question marks have unknown metal content. As in Figure 8 the size of the symbol indicates the luminosity of the nearby galaxy with squares indicating COS-targeted absorbers and circles indicating STIS serendipitous absorbers. Diamonds denote absorbers described in Table 4 and Figure 10. Because of their systematically lower $N_{\rm H\,I}$ we cannot rule out the possibility that many of the Lyα-only clouds have similar metallicities as the metal-bearing clouds.

obvious is the dichotomy of "metal-bearing" and "Lyα-only" absorbers; no absorber at $W_\lambda \geqslant 500$ mÅ lacks metals in the *HST* band. This may be a column density effect or an ionization effect or both.

For example, the three Lyα-only absorbers in the COS target HE 0435−5304 (overlapping open squares at $W_\lambda \approx 200$ mÅ) along the minor axis of ESO 157−49 are constrained geometrically to be outflowing gas (Stocke et al. 2010; Keeney et al. 2012) and so very likely contain metals at or somewhat below the metallicity of their host galaxy. These three minor axis clouds may differ from the two major-axis, metal-bearing clouds only by having lower $N_{\rm H\,I}$. Therefore, *using the current STIS and FUSE spectra*, we cannot constrain the absence of metal absorption lines in these and other Lyα-only absorbers to much better than a few tenths solar metallicity. This means that the current metal-bearing/Lyα-only distinction cannot be used as a significant discriminator for the origin of the Lyα-only clouds. Higher S/N spectra are required to make this distinction for CGM clouds and so to determine the plausible origin of the Lyα-only CGM clouds.

In a plot of the physical quantities, impact parameter and radial velocity difference (Figure 8(a)), we find that, regardless of associated galaxy luminosity, the CGM absorbers enriched with *HST*-bandpass metals (red filled symbols), whether targeted or serendipitous, are found $\leqslant$150 kpc in projection from their nearest galaxy neighbor. This maximum extent of lower-ionization (than O VI) metals is the same as found for low-z luminous galaxies using C IV as a marker for metals (Chen et al. 2001). Tumlinson et al. (2011) found a similar metal enrichment region in high column density O VI around late-type galaxies but they did not observe QSO sight lines beyond 150 kpc from bright galaxies. The observed radial velocity difference between the absorbers and their nearest neighbor galaxies for the metal-bearing absorbers in Figure 8(a) is also similar to the distribution found by Tumlinson et al. (2011, see their Figure 2) in their O VI absorber survey. At larger impact parameter ($\geqslant$150 kpc) and/or velocity difference ($|\Delta v| > 250$ km s^{-1}), the fraction of metal-bearing CGM absorbers dramatically decreases, likely a combination of increased ionization state and decreasing hydrogen column density.

Figure 8(b) plots the same absorber data as in Figure 8(a) but scaling the projected impact parameter by the virial radius and the radial velocity difference by the escape velocity from that impact parameter. These two coordinates are now partially correlated and each axis plots a projected value divided by a 3D (full-space) value. Thus, both coordinate values are strict lower limits. The diagonal lines show the spread in values associated with altering the virial radius definition; i.e., the upper right end of the line uses the "halo-matching" definition of $R_{\rm vir}$ and the lower left end uses Equation (1). Because the escape velocity is computed at the minimum absorber/galaxy distance, the escape velocity for each cloud could be somewhat less than as plotted. We expect that many of the absorbers with normalized velocity differences in Figure 8(b) close to unity have sufficient 3D velocity to escape while all the absorbers with $|\Delta v| > v_{\rm esc}$ have sufficient velocity to escape *if they are outflowing from the nearest galaxy*. By scaling the abscissa and ordinate by quantities related to galaxy mass, there is no indication of segregation by galaxy mass; i.e., there is no strong

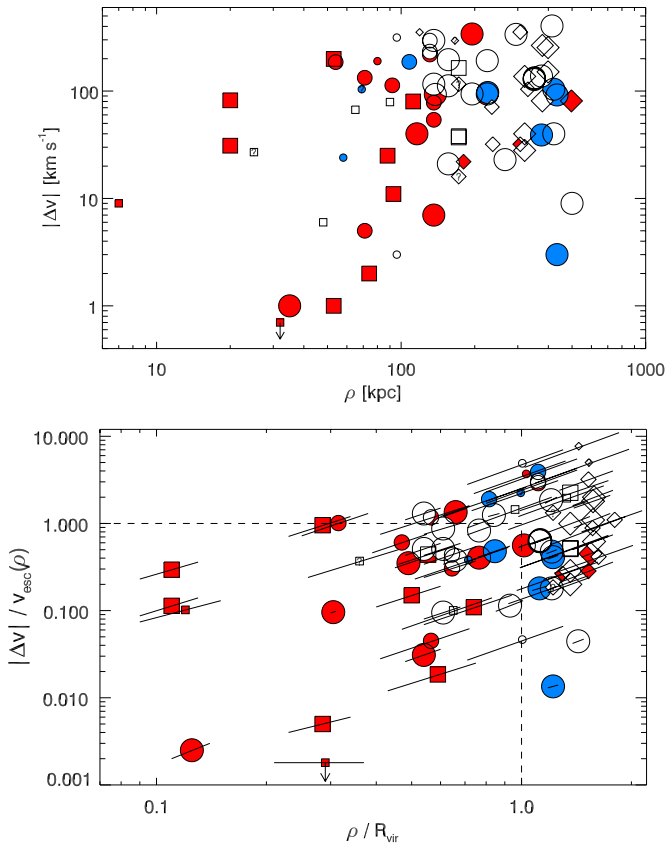

Figure 10. Distribution of CGM absorbers in impact parameter scaled by virial radius and absorber–galaxy radial velocity difference scaled by escape velocity. The symbols here are the same as in Figure 8 except that the diamonds are absorbers from the alternate CGM sample listed in Table 4.

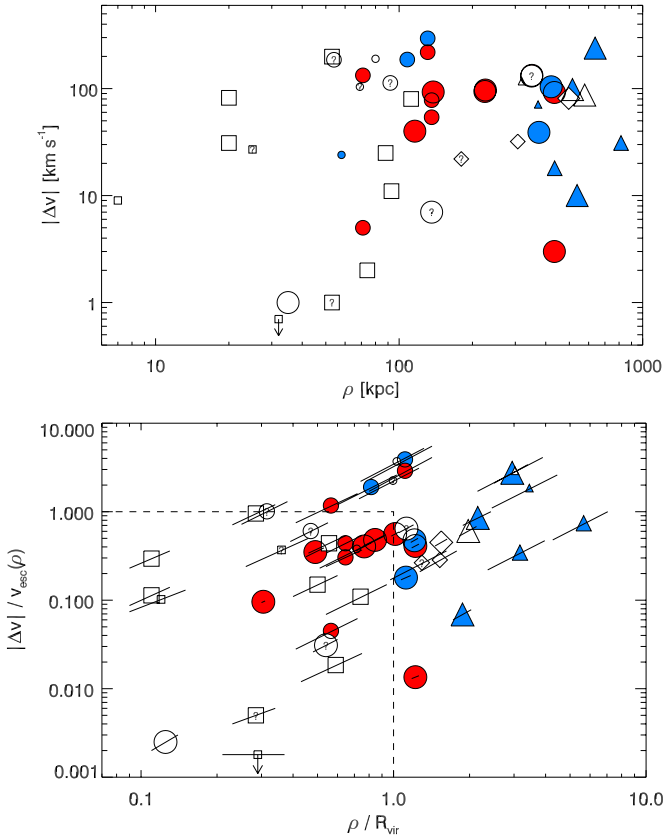

Figure 11. Distribution of absorbers in impact parameter scaled by virial radii and absorber–galaxy radial velocity difference scaled by escape velocity for all metal-bearing absorbers in regions surveyed for galaxies completely down to 0.15 L^*. The filled symbols all have O VI detections; the open symbols lack O VI detections, mostly due to the absence of *FUSE* spectroscopy. The blue filled symbols represent absorbers with O VI-only while the red filled symbols are absorbers containing both O VI and lower ionization absorption. Squares, circles, and diamonds are defined as in Figures 9 and 10, and the triangles show absorbers that are unique to this figure.

evidence for different physical conditions (e.g., sizes or masses) in warm CGM clouds around big and little galaxies. However, this sample is still modest in size and this conclusion requires further work to be confirmed.

Dividing Figure 8(b) into three regions along the x-axis, we find an 12:1 ratio of "metal-bearing" (red and blue symbols) to Lyα-only CGM absorbers (open symbols) at $\leqslant 0.5\,R_{\rm vir}$, a 14:11 ratio at 0.5–1 $R_{\rm vir}$ and a 9:12 ratio beyond $R_{\rm vir}$. Using the alternate definition of virial radius from Equation (1) only changes the statistics outside $R_{\rm vir}$, where three metal-bearing absorbers and 15 Lyα-only absorbers are added, for a total metal-bearing to Lyα-only ratio of 12:27. While there appears to be a clear transition of physical cloud conditions that occurs in the 0.5–1 $R_{\rm vir}$ regime, it is not clear what that transition means in terms of cloud origins, metallicity and physical structure. Higher S/N spectra certainly will assist in determining the nature and point of origin of the lower column density Lyα-only CGM clouds.

If we rather arbitrarily divide this sample vertically at $|\Delta v| = 0.5\,v_{\rm esc}$, 60% of the metal-bearing CGM absorbers are below that line. This suggests that these metal-enriched CGM clouds are bound to their associated galaxies although we cannot tell if these clouds are infalling or outflowing (see Section 4.4). The fraction of metal-bearing clouds at high relative velocities ($|\Delta v| > 0.5\,v_{\rm esc}$) increases with ρ to the point where six of nine "metal-bearing" clouds at $\rho > R_{\rm vir}$ have $|\Delta v| > 0.5\,v_{\rm esc}$ (Figure 8(b)). The changing cloud demographic with $\rho/R_{\rm vir}$ reinforces the use of the virial radius as an *approximate* indicator for the boundary of galactic halos.

In Figure 10, the alternate CGM absorber sample (Table 4) is added as diamond symbols to show that using the alternate definition of $R_{\rm vir}$ does not change the distribution substantially. The color and size codings in Figure 10 are the same as for Figure 8. The alternate sample absorbers are exclusively at $\rho \gtrsim R_{\rm vir}$ and possess $|\Delta v|$ indicative of unbound (if outflowing) gas in almost all cases. As shown explicitly in Figures 2, 4, and 5, there are many more absorbers beyond the virial radii of galaxies on the scale of galaxy groups and large-scale filaments (Penton et al. 2000b, 2004). Otherwise, the alternate sample offers no novel insights or trends not present in the primary sample shown in Figure 8. The sample shown in Figure 8 (and listed in Tables 2 and 3) is the primary CGM cloud sample used for analyses in this paper.

Figure 11 presents a plot similar to Figure 8 for all CGM metal-line absorbers plus all other metal-line absorbers in well-surveyed galaxy regions beyond the virial radius. Detections beyond the CGM are included only if the galaxy survey is complete to below 0.15 L^* at the absorber location. We chose this limit rather than 0.10 L^* because the sample size is a factor of two larger than if we use the slightly lower luminosity completeness limit. The 0.15 L^* luminosity limit is still low enough to provide confidence that almost all sub-L^* galaxies are included in the analysis. The blue symbols are O VI-only

absorbers; the red symbols are absorbers with O VI and lower ion absorption and the open symbols have lower ionization metal lines but no detected O VI. As in Figure 8, the size of the symbol encodes the luminosity of the nearest galaxy while the symbol shape encodes the sample from which the absorber was taken (squares = targeted sample in Table 2; circles = serendipitous sample in Table 3, diamonds = alternate serendipitous sample in Table 4; and triangles are additional O VI absorbers in regions surveyed completely to $L \geqslant 0.15\,L^*$). While lower-ionization metal absorbers generally do not occur in regions much beyond $R_{\rm vir}$ from the nearest galaxy, O VI-only absorbers (i.e., Lyα + O VI absorption only) extend much further out ($\sim$3.5 $R_{\rm vir}$) as reported previously (Stocke et al. 2006). One newly cataloged O VI-only absorber in the PG 1259+593 sight line near the starburst galaxy Mrk 232 is 5 $R_{\rm vir}$ (788 kpc) away in projection, somewhat greater than previously found for any sub-L^* galaxy. In no case do O VI absorbers extend much farther away from their nearest associated galaxy than a distance comparable to the size of a small, spiral-rich group of galaxies. Whether due to the larger ionization parameters of diffuse absorbers far from galaxies ($\log U \geqslant -1.5$) for photoionized clouds or much hotter temperatures ($T \geqslant 10^5$ K) for collisionally ionized clouds, O VI absorption appears to be the best probe for the extent of metal transport away from galaxies into the IGM at low z.

There are three O VI absorbers whose nearest galaxy is a dwarf, suggesting that some metal-line absorbers are associated with very small galaxies. In general, the data shown in Figure 11 support the conclusions made in Section 3.4 that extended, patchy (30% area covering factor) metal-enriched regions exist around galaxies of all luminosity classes. The existence of several O VI absorbers at $\rho > R_{\rm vir}$ with large $|\Delta v|/v_{\rm esc}$ supports the interpretation that at least some outflowing absorbers escape into the IGM. Because the ultimate extent of metals into the IGM is very sensitive to the amount of feedback (e.g., Chen et al. 2001), deep galaxy surveys in regions of O VI absorbers discovered by *HST*/COS at $z \geqslant 0.12$ are a high priority for future ground-based spectroscopic surveys of galaxies near targeted sight lines (e.g., B. A. Keeney et al., in preparation). On the longer-term, an O VI survey at $z < 0.1$ using new far-UV spectroscopic missions are required to measure more accurately the spread of metals around galaxies into the IGM.

It is tempting to compare this result with similar metal transport studies conducted at high S/N ($\sim$30–50) using high-z QSO spectra obtained with Keck/HIRES or VLT/UVES. But all low-z metal transport studies using STIS (and even COS given limited *HST* observing time) are severely S/N limited compared to high-z studies. The O VI absorber extent described in Stocke et al. (2006), Prochaska et al. (2011b), and the current paper all use absorber samples with $\log N_{\rm O\,VI} \geqslant 13.2$ (DS08). Much weaker C IV and O VI lines are detectable at high-z and a much greater extent of metals through the IGM is inferred (e.g., Aguirre et al. 2002), although not well tested owing to the lack of very deep ($L \geqslant 0.1\,L^*$) galaxy survey work at $z \sim 2$. S/N $\sim$ 30–50 *HST*/COS spectra are required to conduct similarly sensitive measurements at $z \sim 0$, whether with individual absorbers or using pixel co-addition techniques (Cowie & Songaila 1998).

4.3. Synopsis of Photoionization Modeling of Warm CGM Clouds

In general, where metals are associated with these CGM absorbers, the higher ions associated with warm, photoionized gas (Si IV and C IV) predominate over lower ions (Si II and C II) in both the targeted and the serendipitous samples. No strong Mg II ($W_\lambda \geqslant 0.5$ Å) absorption was found for any of the few targeted absorbers observed with the G285M grating and only one targeted and three serendipitous absorbers have stronger low ions (i.e., Si II > Si IV). The $cz = 5225$ km s^{-1} absorber in the PG 0832+251 sight line is one of the few absorbers dominated by lower ions and is an LLS at $\log N_{\rm H\,I} \approx 18.4$ (but Mg II was not observed for this, previously unknown, LLS). A dust lane across the disk of the nearby low-level starburst galaxy NGC 2611 and the sign of the absorber/galaxy velocity difference require that this absorber is outflowing from NGC 2611 (Stocke et al. 2010; Paper II) but its low relative radial velocity ($|\Delta v|/v_{\rm esc} \approx 0$; see Table 2) suggests that it will not escape into the IGM. A companion absorber at $cz = 5437$ km s^{-1} has a much larger $|\Delta v|/v_{\rm esc} = 1.2$ and is infalling based on the sign of its velocity difference from NGC 2611. This second component has a much higher ionization spectrum, more typical of the remainder of the sample.

There are a few other LLSs we have modeled based on direct detections of flux decrements in *FUSE* spectra: PG 1116+215 at $cz = 41{,}521$ km s^{-1} (Tripp et al. 1998), PHL 1811 at $cz = 24{,}222$ km s^{-1} (Jenkins et al. 2003), PKS 0405−123 at $cz = 50{,}105$ km s^{-1} (Prochaska et al. 2004), and PKS 1302−102 at $cz = 28{,}435$ km s^{-1} (see Table 6). These LLSs are all associated with $L \geqslant 0.3\,L^*$ galaxies consistent with many earlier studies of strong Mg II/LLS absorbers (e.g., Steidel 1995; Churchill et al. 2000; Kacprzak et al. 2011; Chen et al. 2010).

Another of the very few low-ionization absorbers is at 1585 km s^{-1} in the 3C 273 sight line in the serendipitous sample (see Table 3). Because this absorber already had been studied in detail by Sembach et al. (2001), Tripp et al. (2002), and Stocke et al. (2004), we modeled this absorber as a check on our CLOUDY analysis process. Standard photoionization modeling by Tripp et al. (2002) found a surprisingly high hydrogen density of $n_{\rm H} = 10^{-2.8}$ cm^{-3}, low temperature ($\sim 10^4$ K), and thus quite a small line-of-sight size of 70 pc. The metallicity of 6% solar and a super-solar Si/C ratio suggesting recent Type II supernova enrichment are consistent with the absorber originating in a nearby ($\rho \approx 70$ kpc) post-starburst dwarf galaxy of similar metallicity (Stocke et al. 2004). The large absorber/galaxy radial velocity difference, large impact parameter (see Figure 8(b); top right small red filled circle) and small host galaxy mass require that this absorber will escape into the IGM. While the equivalent width measurements for the various low ions are slightly different in DS08 as compared to those used by Tripp et al. (2002), we recover very similar cloud parameters (see Table 6) including small cloud size and low metallicity. This absorber is one of the few (three) metal-bearing absorbers with no O VI detection. There are a few other targeted and serendipitous absorbers which have modeled line-of-sight sizes $\sim$100 pc but all of these have higher ionization parameter and O VI detected.

We have attempted photoionization modeling only for those 15 serendipitous absorbers in Tables 3 and 4 plus 9 targeted absorbers in Table 2 with multiple metal ion detections. We required detections of two or more ionization states of the same element in order for a satisfactory model to be calculated; i.e., (C II, C III, C IV) in the serendipitous sample where *FUSE* spectra are available or (Si II, Si III, Si IV) where only *HST*/STIS or *HST*/COS spectra exist like in the targeted sample. Column densities of O VI are not used in this modeling both because this high ion likely traces collisionally ionized gas and because

Table 6
Indicative Photoionization Models of Warm CGM Clouds

Sight Line	cz_{abs} (km s^{-1})	log $N_{H\,I}$	log U	log $(Z/Z_\odot)$	log n_H[a]	D_{cl}[b] (kpc)	log[c] $(M_{cl}/M_\odot)$
HE 0439−5254	1662	15.21 ± 0.44[d]	$-2.4^{+0.3}_{-0.2}$	$+0.1^{+0.9}_{-0.4}$	−3.7	1.1	3.7
PG 0832+251	5227	18.48 ± 0.17[d]	$-3.5^{+0.1}_{-0.2}$	-0.5 ± 0.2	−2.6	16	8.3
PG 0832+251	5425	16.39 ± 0.91[d]	$-2.4^{+0.4}_{-0.5}$	$-0.9^{+0.7}_{-0.5}$	−3.7	28	7.9
PMN J1103−2329	1194	15.94 ± 0.47[d]	$-2.2^{+0.4}_{-0.5}$	$-0.8^{+0.5}_{-0.4}$	−3.9	31	7.8
RX J0439.6−5311	1671	15.41 ± 0.42[d]	$-2.6^{+0.4}_{-0.2}$	$-0.3^{+0.6}_{-0.5}$	−3.5	1.2	4.0
SBS 1108+560	665	17.38 ± 0.63[d]	-3.1 ± 0.4	$0.0^{+1.0}_{-0.5}$	−3.0	7.4	6.8
SBS 1108+560	778	15.44 ± 0.42[d]	-2.3 ± 0.3	-0.5 ± 0.3	−3.8	5.7	5.7
SBS 1122+594	1204	15.92 ± 0.42[d]	-2.5 ± 0.4	-0.2 ± 0.3	−3.5	3.8	5.5
VII Zw 244	712	15.81 ± 0.26[d]	$-2.8^{+0.1}_{-0.2}$	$-0.2^{+0.1}_{-0.2}$	−3.2	0.70	3.5
3C 273	1585	15.85 ± 0.09[e]	$-3.2^{+0.2}_{-0.1}$	-0.9 ± 0.2	−2.9	0.17	2.1
PG 1116+215	41521	16.35 ± 0.10[f]	-3.3 ± 0.1	$-0.3^{+0.1}_{-0.2}$	−2.8	0.28	2.8
PG 1211+143	15302	15.67 ± 0.35	$-2.9^{+0.5}_{-0.3}$	$-0.5^{+0.3}_{-0.4}$	−3.2	0.52	3.2
PG 1211+143	19329	15.17 ± 0.10[g]	$-2.4^{+0.1}_{-0.2}$	-0.9 ± 0.1	−3.7	2.2	4.5
PG 1211+143	19467	13.82 ± 0.05	-2.1 ± 0.1	$-0.2^{+0.2}_{-0.1}$	−3.9	0.14	0.9
PG 1259+593	13808	15.51 ± 0.28	$-2.2^{+0.3}_{-0.9}$	$-1.1^{+0.9}_{-0.3}$	−3.9	14	6.7
PG 1259+593	13940	14.75 ± 0.38	$-1.7^{+0.3}_{-1.3}$	$-0.6^{+0.8}_{-0.5}$	−4.4	21	6.9
PHL 1811	22032	14.88 ± 0.09[h]	$-2.7^{+0.3}_{-0.2}$	$-0.3^{+0.2}_{-0.3}$	−3.3	0.14	1.4
PHL 1811	23310	14.94 ± 0.08	-2.7 ± 0.2	-0.2 ± 0.2	−3.3	0.15	1.5
PHL 1811	24222	18.00 ± 0.50[f]	$-3.5^{+0.3}_{-0.9}$	$-0.7^{+0.8}_{-1.4}$	−2.5	4.1	6.5
PHL 1811	52926	14.87 ± 0.03	-2.6 ± 0.5	$-0.5^{+0.4}_{-0.5}$	−3.5	0.33	2.3
PKS 0405−123	50105	16.45 ± 0.07[f]	-3.0 ± 0.1	$+0.1 \pm 0.2$	−3.1	1.2	4.4
PKS 1302−102	12665	14.83 ± 0.17	-2.8 ± 0.1	$+0.2 \pm 0.2$	−3.3	0.08	0.6
PKS 1302−102	28435	17.10 ± 0.40[f]	$-3.1^{+0.5}_{-0.3}$	$-1.7^{+0.6}_{-0.4}$	−3.0	6.0	6.6
Q 1230+011	23399	15.06 ± 0.40	$-2.2^{+0.4}_{-0.7}$	-0.2 ± 0.4	−3.9	3.0	4.8

Notes. Column densities are given in units of cm^{-2} and densities in cm^{-3}.
[a] Total hydrogen column density, $\log n_H = -6.074 - \log U$.
[b] Cloud thickness along the line of sight.
[c] Cloud mass, assuming spherical clouds with diameter D_{cl}, uniform density n_H, and purely hydrogen+helium composition.
[d] We have constrained the H I column densities of the targeted absorbers by assuming that the H I and metal lines reside in a single photoionized phase. See Keeney et al. (2012) and Paper II for details.
[e] We have adopted the column densities of Tripp et al. (2002) to model this absorber rather than those of Danforth & Shull (2008).
[f] These column densities have been modified from the DS08 values by including information on the Lyman-limit decrement for high column density absorbers. The column density for the PKS 0405−123 absorber is from Prochaska et al. (2004).
[g] The DS08 column density for this absorber ($\log N_{H\,I} = 15.73 \pm 0.32$) has been revised using a new curve-of-growth analysis that favors $b = 33 \pm 4$ km s^{-1} and $\log N_{H\,I} = 15.17 \pm 0.10$.
[h] DS08 lists two absorbers at $cz = 21{,}995$ and 22,050 km s^{-1}, but further scrutiny reveals no evidence of multiple velocity components.

its redshifted wavelength has been observed for only one of the targeted absorbers, PG 0832+251 at $cz = 5225$ km s^{-1}. While the targeted CGM absorbers have only Lyα with which to determine a hydrogen column density, the serendipitous absorbers all have higher Lyman line detections from *FUSE* and thus much more accurate $N_{H\,I}$ values from curve-of-growth analysis (DS08). While the nine targeted absorbers that meet the metal-line criteria have poorly determined $N_{H\,I}$ values (this is particularly true of the M 108 absorbers because the COS spectrum of SBS 1108+560 contains a higher-redshift LLS that reduces the S/N at Lyα significantly), we have used other constraints to reduce the errors on the hydrogen column density considerably. Specifically, the range of plausible $N_{H\,I}$ values in Table 6 requires consistency with a single-phase photoionization model constrained by the observed metal-line ratios, an absorber size $<$ the impact parameter, and an absorber metallicity $\lesssim$ the galaxy metallicity (which sets a lower bound on $N_{H\,I}$). The procedure which uses these constraints to create viable photoionization models is shown in detail in Keeney et al. (2012) for the two metal-bearing absorbers in Table 6 in the HE 0439−5254 and RX J0439.6−5311 sight lines.

These cloud models are derived from single homogeneous CLOUDY (Ferland et al. 1998) calculations assuming only photoionization by an external radiation field as specified in Haardt & Madau (2012). Even the most proximate absorbers in the targeted sample are farther away from their associated galaxies than their "proximity distance" where additional ionization from hot stars begins to contribute significantly if the escape fraction is as high as ∼5% (Giroux & Shull 1997). All of the models were produced using the same, standard procedure explained in detail on a case-by-case basis in Paper II. Here, by way of a synopsis, we list the results of these models in Table 6, which contains the following information by column: (1) the sight line target name; (2) the absorber heliocentric recession velocity (km s^{-1}); (3) the log of the neutral hydrogen column density ($\log N_{H\,I}$) in cm^{-2}; (4) the log of the ionization

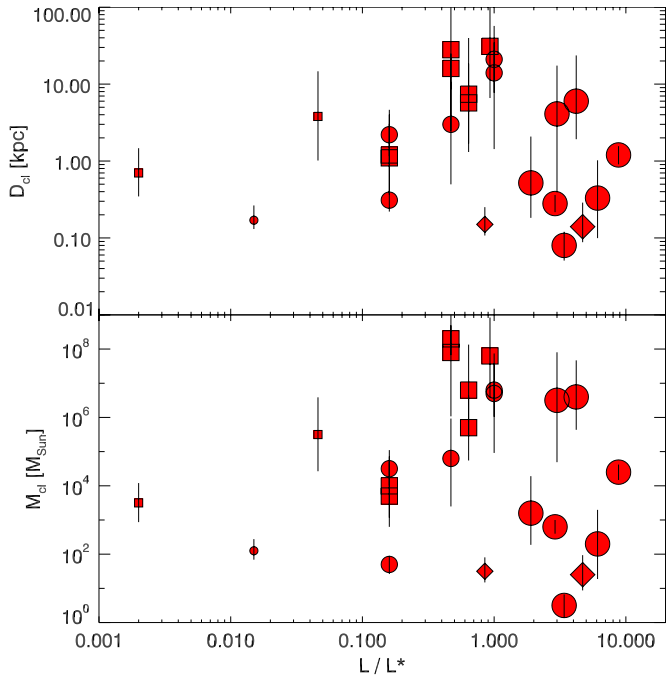

Figure 12. Distribution of modeled CGM cloud diameters (top) and cloud masses (bottom) as a function of host galaxy luminosity. The symbology is the same as for Figure 10 and all symbols are filled (indicating metal-bearing clouds) because a requirement for our applying CLOUDY modeling to absorbers in our sample is that at least two different ionization states of the same element (i.e., either C or Si) must be present.

(A color version of this figure is available in the online journal.)

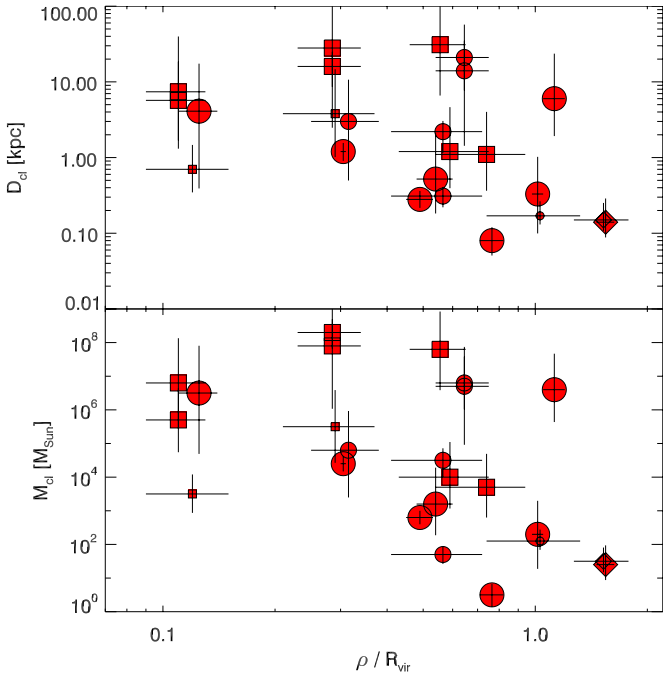

Figure 13. Distribution of modeled CGM cloud diameters (top) and cloud masses (bottom) as a function of scaled impact parameter. The symbology is the same as for Figure 10 and all symbols are filled (i.e., "metal-bearing") as required for the CLOUDY modeling. The declining CGM cloud sizes and masses as a function of impact parameter is similar to the trend of Lyα equivalent width with radius seen in Figure 9. While a power law has been fit to these data (see the text for best-fit parameters), these fits are poor (reduced $\chi^2 \gg 1$).

(A color version of this figure is available in the online journal.)

parameter ($\log U$); (5) the log of the mean metallicity as determined from CLOUDY modeling ($\log(Z/Z_\odot)$) assuming solar abundance amounts and ratios from Grevesse et al. (2010); (6) the log of the total hydrogen density ($\log n_{\rm H}$) in cm^{-3}; (7) a characteristic cloud diameter ($D_{\rm cl}$) as determined from a modeled line-of-sight cloud depth in kiloparsecs; and (8) the logarithm of the estimated total cloud mass ($\log M_{\rm cl}$) in solar masses. As a check on our CLOUDY modeling, we have used our procedure to reproduce the physical conditions derived by others for some of the same absorbers in Table 6 including 3C 273 at $cz = 1585$ km s^{-1} (Tripp et al. 2002) and PKS 0405−123 at $cz = 50{,}105$ km s^{-1} (Prochaska et al. 2004). The sizes and masses of our models differ from others by factors of 2–3 and 4–10, respectively, even in cases where we have used the same measured column densities. These differences underscore that these models are indicative, not precise.

Before using the model results of Table 6 to assess physical conditions in the CGM of late-type galaxies, the next set of figures explores whether these derived quantities are dependent on either galaxy luminosity or impact parameter. Despite concerns that the virial radius and escape velocity scalings may mask trends between CGM cloud parameters and galaxy luminosity, Figure 12 shows that neither cloud diameter (top) nor mass (bottom) are dependent upon galaxy luminosity (although data below 0.1 L^* are quite sparse). The physical conditions derived from the CLOUDY modeling of these clouds (temperature, density, and pressure) also show no dependence on host galaxy luminosity. Warm CGM clouds are similar regardless of the host galaxy nearby, excepting that no LLSs have been detected around dwarfs, consistent with earlier results (Steidel 1995; McLin et al. 1998). However, there are weak trends in cloud diameter and mass with scaled impact parameter that are similar to the Lyα equivalent width dependence seen in Figure 9 with smaller, less massive clouds at larger scaled impact parameters (Figure 13): $D_{\rm cl} = (0.19 \pm 0.04\,{\rm kpc})(\rho/R_{\rm vir})^{-1.7\pm0.2}$ and $M_{\rm cl} = (36 \pm 2\,M_\odot)(\rho/R_{\rm vir})^{-6.2\pm0.5}$ (quoted errors are statistical only). While these best-fit power laws decline with radius, the scatter is substantial and the fits quantified above are poor (reduced $\chi^2 \gg 1$). Large, massive clouds exist at all radii. However, Lyα-only clouds are found almost exclusively at $\rho \approx R_{\rm vir}$.

Despite the generally declining cloud size and mass with impact parameter, the pressure within CGM clouds estimated from mean cloud densities (Table 6, Column 6) and temperatures (not shown but always near $\log T \approx 4.0$–4.3 K) does not appear to decline very steeply with scaled impact parameter regardless of galaxy luminosity (Figure 14). The best-fit power law to the data in Figure 14 is $(P/k) = (12 \pm 2\,{\rm cm^{-3}\,K})(\rho/R_{\rm vir})^{-0.3\pm0.2}$, and has a reduced χ^2 value of 3.3. Clearly any trend in these data is minimal. The surprising absence of a clear trend in cloud pressure with impact parameter will be addressed in Section 5.1. Neither cloud diameter, mass nor pressure vary significantly with absorber–galaxy relative velocity for this sample of 24 modeled CGM absorbers.

4.4. Limited CGM Cloud Origin Information

The following information which bears on the origins of the CGM clouds in this sample is available: (1) absorber metallicity for 24 modeled clouds (Table 6); (2) infall/outflow determination made using the 3D orientation of the galaxy (possible for only four galaxies and eight absorbers in this sample); (3) the position angle on the sky relative to the galaxy orientation (i.e., absorber projected closer to the major or minor axis; Bouché et al. 2012) as shown in Figure 6 (39 absorbers

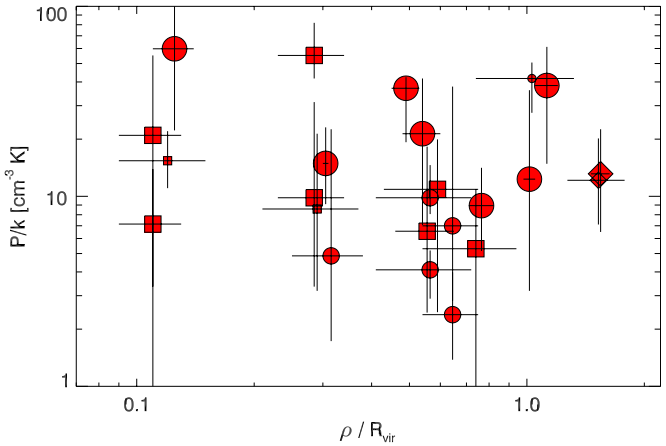

Figure 14. Modeled mean pressure (P/k in cm^{-3} K) inside warm CGM clouds as a function of scaled impact parameter. Surprisingly, there is no indication of a strong trend as might be expected if these clouds are in pressure equilibrium with a hot ($T \approx 10^6$ K) gaseous halo, whose density is declining rapidly with radius around the host galaxy. While a power law has been fit to these data (see the text for best-fit parameters), this fit is poor (reduced $\chi^2 \approx 3.3$).

(A color version of this figure is available in the online journal.)

have these data); and (4) absorber velocity relative to its host galaxy as a fraction of escape velocity (Figure 8(b), which plots 58 absorbers from Tables 2 and 3). The last two sets of data are suggestive in some cases but not conclusive as to cloud infall/outflow kinematics and origin.

4.4.1. Absorber Metallicity versus Host Galaxy Metallicity

While absorber and host galaxy metallicities are important in determining whether the absorbing gas originated in the nearby galaxy, this information is not entirely definitive because modeled metallicity values can have large associated errors (±0.2–0.4 dex; see Table 6 and Paper II). Also, a dilution of metal-enriched gas by more pristine gas in the galaxy's vicinity can decrease absorber metallicity by an unknown amount so that an absorber which originates in the host galaxy can have $Z_{abs} < Z_{gal}$. Recently, Lehner et al. (2013) found a strong bifurcation of luminous galaxy CGM absorber metallicities at $Z_{abs} = 0.1$–0.2 solar. These authors conclude that the more metal-rich absorbers likely originate in the nearby large galaxy and may be outflowing or recycling gas while the lower metallicity gas is infall. We adopt a similar criteria to make our tentative assessments of this sample of absorbers. Of the modeled absorber metallicities for the 24 cases in Table 6, many values are broadly consistent with the metallicities of their host galaxies. Whether these absorbers are infalling or outflowing is not specifically known but nine of them have $|\Delta v| \ll v_{esc}$ so we identify these as likely recycling gas. Six of these are at $\rho \leqslant 0.5\ R_{vir}$. For most other absorbers in Table 6, the modeled absorber metallicities are not sufficiently accurate or sufficiently different from their host galaxy metallicities to provide secure cloud origin determinations.

However, there are a few absorbers for which we can be more definite. Three absorbers have modeled metallicities consistent with gas originating in the nearby host galaxy (i.e., $Z_{abs} \approx Z_{gal}$) but with $|\Delta v| > v_{esc}$. We identify these three absorbers as likely outflowing gas. One of these is the 3C 273 absorber at $cz = 1585$ km s^{-1}, which has a metallicity of a few percent solar (Tripp et al. 2002; Table 6). Its host galaxy is a nearby, post-starburst dwarf, which also has a few percent solar metallicity, suggesting that the absorber is outflowing and its radial velocity ($\Delta v = 5.2\ v_{esc}$) requires it to be unbound (Stocke et al. 2004).

Four other absorbers have metallicities of $\leqslant$20% solar with super-L^* associated galaxies (Lehner et al. 2013), much less than expected if the gas originated in their host galaxies even with dilution by pristine gas. We identify these absorbers as likely infalling gas. One targeted sample absorber associated with the starburst galaxy NGC 2611 (Table 2) has ∼10% solar metallicity and is constrained to be infalling gas by the geometrical argument made in the next subsection. A low-metallicity (∼15% solar) absorber in the targeted PMN J1103−2329 sight line is associated with a 0.9 L^* spiral and is also constrained geometrically to be infalling. A low-metallicity serendipitous absorber (∼3% solar) is identified with a 2 L^* galaxy in the PKS 1302−102 sight line ($cz = 28{,}435$ km s^{-1} absorber). The fourth low-metallicity absorber/galaxy pair is somewhat more ambiguous. The PG 1211+143 absorbers at $cz = 19{,}329$ and $19{,}467$ km s^{-1} have metallicities of ∼15% solar and solar. In this case we interpret the higher metallicity absorber as originating, not in the nearest 0.16 L^* galaxy (Table 3), but in a 1.2 L^* galaxy (Table 5) only slightly further away at 0.77 R_{vir} in projection. The lower metallicity absorber could either originate in the lower luminosity galaxy or be falling into either of the two nearby galaxies, originating elsewhere. Given that this system is most simply described as a large galaxy with a small companion in its halo, the least ambiguous interpretation of these two absorbers is entirely with respect to the 1.2 L^* spiral (Tumlinson et al. 2005) with the solar metallicity absorber being outflow and the subsolar absorber being infall.

4.4.2. Three-dimensional Orientation of Host Galaxy

Although the sign of the absorber/galaxy radial velocity difference is known, whether the absorber is infalling or outflowing is not known unless the 3D orientation of the galaxy can be determined (Stocke et al. 2010). This is the primary reason why we have chosen to plot the absolute value of the galaxy–absorber velocity difference in Figures 8 and 10. Three-dimensional orientation determinations are possible only for those few galaxies with both well-defined disks inclined at an intermediate angle relative to us on the sky and also some global internal extinction pattern (i.e., one side of the galaxy disk is more obscured than the other from our perspective, and therefore more distant from us). Even possessing this information, an infall/outflow determination is possible only for absorbers within about 45° of the galaxy's minor axis, for which we *assume* a total motion perpendicular to the galaxy's disk. Therefore, we have solid determinations for only eight absorbers near four galaxies in the targeted list: HE 0435−5304/ESO 157−49 (three components with Lyα-only detected; Keeney et al. 2012), SBS 1108+560/M108, PNM J1103−2329/NGC 3511, and PG 0832+251/NGC 2611 (see Paper II for detailed descriptions). The geometry and sign of Δv require that the two lower redshift HE 0435−5304 absorbers are outflowing while the third is infalling. The lower redshift, higher metallicity SBS 1108+560 absorber is found to be outflowing, the other infalling. PG 0832+251 possesses one outflowing (the $\log(Z/Z_\odot) = -0.5$ LLS) and one infalling ($\log(Z/Z_\odot) \sim -0.9$) absorber (Table 6). The PNM J1103−2329 absorber associated with NGC 3511 is infalling and has low metallicity ($\log(Z/Z_\odot) \sim -0.8$). No absorber/galaxy pairs in the serendipitous list have geometrically well-determined directions for the gas flow.

But the case of the three Lyα-only absorbers located along the minor axis just beyond the virial radius of ESO 157−49 is a cautionary tale for this analysis. The geometry of the host galaxy requires that two of these are outflowing absorbers but no metals are detected in the COS spectra (Keeney et al. 2012). However, the absorbers' lower $N_{\rm H\,I}$ values makes the absence of metal absorptions reasonable if these clouds have similar metallicity and physical conditions to the absorbers found in the other two sight lines around ESO 157−49 (Keeney et al. 2012). Therefore, the assignment of these two absorbers specifically, and the other "Lyα-only" clouds in general, as very low metallicity infalling gas is not justified by the limited sensitivity of the current data. Given the substantial fraction of CGM absorbers at $\rho > 0.5\,R_{\rm vir}$ which are "Lyα-only" clouds, a confident accounting of low-metallicity gas infall onto galaxies requires higher S/N spectra than in hand currently.

4.4.3. Absorber Location Relative to Host Galaxy's Minor Axis

Another piece of information that is available for many absorbers is absorber location relative to the host galaxy's major axis (see Figure 6). This determination is possible for 26 serendipitous CGM absorbers and 14 (all but 3) targeted absorbers based on galaxy sky orientations from NED. Most of these values come from SDSS and have been checked by us for plausibility. Several host galaxies simply lack such information while others have no well-defined major axis (e.g., a dwarf Magellanic spiral) and some galaxies are face-on. Using a sample of very low-z Mg II absorbers, Bouché et al. (2012) found most absorbers concentrated around either the host galaxy's major or minor axis. They identified the major axis absorbers with infalling gas and the minor axis absorbers as outflowing gas. But this assignment is far from certain (e.g., the 3C 232 absorber near NGC 3067 and one absorber each in the three sight lines mentioned in the last subsection are located along the minor axis but constrained by geometry to be infalling; Stocke et al. 2010, Section 2.1). Therefore, until this dichotomy can be tested further, we must view it as interesting but unreliable. This is especially true for the serendipitous sample absorbers, which are rather isotropically configured around their host galaxies. The absence of a bi-modal, major axis/minor axis concentration in absorber position angle persists even for absorbers at absorber/galaxy separations of $\leqslant$100 kpc. Therefore, we make no cloud origin determinations based on these data.

4.4.4. Absorber Velocity Relative to Host Galaxy

In Section 4.2, Figure 8(b) was divided into plausible regions in both coordinates which we interpret further here using the additional information described above.

1. Inside $0.5\,R_{\rm vir}$ almost all absorbers (12 of 13) contain metals. The one exception is a dwarf associated with a COS pointing. Although the data quality of this spectrum is good (S/N $\sim$ 20 in G130M and $\sim$12 in G160M), the metallicity of gas associated with this dwarf could also be quite low, plausibly below 0.1 solar which would not be detectable in the spectrum given the observed $N_{\rm H\,I}$ value. Six of these thirteen absorbers have radial velocity differences, $|\Delta v| \leqslant 0.1 v_{\rm esc}$, so low that we conclude that these six are bound clouds, despite not knowing whether they are outgoing or infalling at the present time. These six have $Z_{\rm abs} \approx Z_{\rm gal}$. Geometry constrains two of these 13 absorbers to be outflowing and one to be infalling (see Section 4.4.2). Two other absorbers (at $cz = 5425$ km s^{-1} in the PG 0832+251 sight line and at $cz = 1194$ km s^{-1} in the PMN J1103−2329 sight line), which are constrained to be infalling by geometry, have large $|\Delta v|/v_{\rm esc} = 1.2$ and 0.54, respectively. Both of these absorbers have low metallicities. The $|\Delta v| > v_{\rm esc}$ for the PG 0832+251 absorber strongly suggests that this is infalling gas originating outside NGC 2611; the case of the PMN J1103−2329 absorber is less certain. The remaining metal-bearing clouds at small impact parameter have intermediate $|\Delta v|/v_{\rm esc} = 0.2$–$0.8$ values (see Figure 8(b)) and so are less securely classified.
2. At $0.5\,R_{\rm vir} < \rho < R_{\rm vir}$, 14 absorbers have metals detected at $\log(Z/Z_\odot) \gtrsim -1.0$. Four of these have $\log(Z/Z_\odot)$ close to solar metallicity and so we identify these four as originating inside their $L \geqslant L^*$ host galaxies. Three of these four have $|\Delta v|/v_{\rm esc} < 0.1$ and are identified as likely bound recycling gas clouds. The remainder have intermediate values of $|\Delta v|/v_{\rm esc}$ and metallicity (or uncertain metallicity) so that their kinematic origin and fate are unclear. The 11 Lyα-only clouds in this region have unknown metallicities and so unknown origin and fate.
3. Outside the virial radius to our arbitrary limit of $1.5\,R_{\rm vir}$ there are nine metal-enriched absorbers, four of which have relative velocities much greater than $v_{\rm esc}$, while four others have a velocity indicative of probable escape. Of the three absorbers that have $|\Delta v| \gg v_{\rm esc}$, two have $Z_{\rm abs} \approx Z_{\rm gal}$ and are identified as outflowing, unbound gas (including the 3C 273 absorber discussed in Section 4.4.1); the third absorber has a very low ($\log(Z/Z_\odot) \sim -1.7$) metallicity, so we identify it as infalling (see Section 4.4.1).
   The Lyα-only absorbers in this region have varying relative velocities and so their origins and fates are unknown, excepting for the three in the HE 0435−5254 sight line along the minor axis of ESO 157−49, discussed above.
   Given the substantial sky area surveyed around these galaxies for absorbers, and the $d\mathcal{N}/dz = 50$ per unit redshift for $\log N_{\rm H\,I} \geqslant 13.0$ (Penton et al. 2004), a few (three to five) of the absorbers at large impact parameters could be projected systems; i.e., the absorbers are actually several Mpc away radially despite having redshifts within ± 400 km s^{-1} of the galaxy.

In summary, based upon using a combination of the factors listed above, we have not yet obtained secure origins and fates for CGM clouds in a majority of cases. However, probable assignments can be made in some cases. Nine absorbers at $\rho < R_{\rm vir}$ (six at $\rho < 0.5\,R_{\rm vir}$) have metallicities broadly consistent with their host galaxies and very low absorber–galaxy velocity differences (radial velocity difference $\leqslant$10% of $v_{\rm esc}$). The latter population is very likely bound, recycling "galactic fountain" gas, although we cannot distinguish which clouds are outgoing and which are infalling at the present time. Five CGM absorbers with metallicities comparable to their host galaxy metallicities have sufficient velocities to escape and so we identify them as unbound outflow; three of these are constrained by geometry (Section 4.4.2) to be outflowing gas. Importantly, three absorbers with $Z_{\rm abs} \ll Z_{\rm gal}$ are identified as infalling. One of these three is constrained geometrically to be infalling gas. The bulk of the absorbers, particularly the Lyα-only clouds, have unknown origins at the present time. While current data do not provide unambiguous origin and fate for the majority of CGM absorbers, our analysis suggests that this is a realizable goal. Future, higher-S/N UV spectra with COS can determine cloud metallicities at <10% solar and ground-based spectroscopy of

H II regions in the host galaxies will provide more accurate absorber/galaxy metallicity differences to help determine the origin of these clouds.

In the next section, we use the photoionization modeling of enriched clouds with multiple ion metal detections described in Section 4.3 to determine warm CGM cloud properties in bulk. Based on the analysis in this section, a substantial fraction ($\sim$ one-third) of these absorbers is identified as "galactic fountain" clouds based on their metallicities and kinematics.

4.5. CGM Physical Characteristics Derived from the Combined Samples

As shown in Table 6, the warm, photoionized CGM gas clouds typically have 10% solar to solar metallicities, ionization parameters of $\log U = -2.2$ to -3.0, cloud sizes (characteristic diameters) of 0.1–10 kpc, total densities of $\sim 10^{-3}$ to 10^{-4} cm^{-3}, temperatures (not shown) of 16,000–24,000 K, and masses of $\sim$10–$10^8\,M_\odot$. Many of the absorbers in Table 6 have locations projected within the inner half virial radius of the associated galaxy and relative velocities indicative of being bound, recycling gas. There are six Lyman-limit and partial Lyman-limit systems in Table 6 that have considerably higher densities ($n_{\rm H} \geqslant 10^{-3.0}$ cm^{-3}) than the other absorbers and are among the more massive CGM clouds. The cloud parameters found in Table 6 are similar to those found for highly ionized HVCs around the Milky Way (Shull et al. 2009; Lehner & Howk 2011; Putman et al. 2012) but most of these clouds have lower ionization parameters, lower mean densities, and larger sizes and masses. Among the CGM clouds modeled using CLOUDY, three absorbers appear to be unbound, outflowing gas (see Section 4.4). There is no obvious distinction between the models for unbound versus bound clouds in this sample, although four of the unbound absorbers (3C 273 at $cz = 1585$ km s^{-1} and PKS 0405−123 at $cz = 45{,}378$ km s^{-1} in Table 3 and PHL 1811 at $cz = 22{,}032$ km s^{-1} (see discussion of this absorber below) and PHL 1811 at $cz = 23{,}310$ km s^{-1} in Table 4) have no detected O VI ($\log N_{\rm O\,VI} \leqslant 13.2$). Only one other metal-bearing serendipitous absorber has undetected O VI (the LLS in PHL 1811 at $cz = 24{,}222$ km s^{-1}).

The discussion in Section 4.3 and Figures 12–14 show that, except for the marginally significant decline in CGM cloud size and mass with impact parameter, there is little distinction between CGM clouds as a function of galaxy luminosity (for galaxies with $L \geqslant 0.1\,L^*$), radial location or relative velocity once the virial radius scaling is applied. The dwarf sample has lower covering factor and cloud masses but these conclusions are based upon smaller numbers of examples. Since the clouds we have modeled using CLOUDY are a modest fraction of the full ensemble of CGM clouds, we must assume something about the clouds we have not modeled (or cannot model), those containing few or no metal absorptions. In order to proceed we will assume that all other CGM clouds are physically similar to the models in Table 6. Almost all of the CGM clouds at $\rho \leqslant 0.5\,R_{\rm vir}$ have been modeled and the inner half virial radius contains the more massive clouds statistically, so the most massive portion of the CGM is well modeled by the available data. For the outer half of the CGM, to be conservative we assume that the "Lyα-only" clouds are scaled-down versions of the clouds modeled in Table 6, smaller and less massive but with the same $\log U$, consistent with the available data. However, it is possible that some or even many of the Lyα-only CGM clouds at large impact parameter are more highly ionized (many are detected in O VI) with $\log U \geqslant -2.0$, which could mean that they are larger and more massive. If this is the case our calculations have underestimated the total CGM warm cloud mass somewhat.

While we have measured very high CGM cloud covering factors, these near unity values do not require very large filling factors of CGM clouds because we are viewing these galaxies from afar, a situation geometrically quite different from our view inside the Milky Way looking outward where large observed area covering factors for HVCs *do imply* large volume filling factors (Shull et al. 2009; Lehner & Howk 2011). The current situation is analogous to viewing clouds in our own Earth's atmosphere around the setting Sun. A similar geometry causes the covering factor of CGM clouds around external galaxies to be near unity, even if the filling factor of clouds is $\lesssim$10% (see below).

In the present case, we have measured a very high covering factor for the CGM out to approximately $R_{\rm vir}$. Now we need to estimate the filling factor for clouds of varying cloud sizes from these covering factors. To do this we assume that a galaxy halo extends spherically to its virial radius and is partially filled with spherically shaped warm CGM clouds whose sizes are determined from the modeled sizes found in Table 6. Since we are viewing these galaxies from an arbitrary direction, the assumption of cloud sphericity seems reasonable; i.e., the line-of-sight cloud diameters found by photoionization modeling characterize cloud sizes averaged over viewing angle, which is well approximated by circular clouds inside a circular CGM region on the sky. For the calculation below, a covering factor of $C \sim 100\%$ inside $1/2\,R_{\rm vir}$ and $C \sim 75\%$ between $0.5\,R_{\rm vir}$ and $R_{\rm vir}$ is assumed, values consistent with Figure 3 for the super-L^* and sub-L^* samples. For the dwarfs we assume $C = 0.5$.

An additional, an important geometrical factor to consider is "shadowing." When one or more clouds lie behind another from our perspective, the observed covering factor (C) implies a larger filling factor (F) of CGM clouds, augmented by the amount of "shadowing" (S). S is the mean number of distinct clouds along a sight line within any one galaxy CGM (i.e., at $|\Delta v| \leqslant 400$ km s^{-1}) and can be measured statistically using the percentage of multiple CGM systems (e.g., in Tables 2–4 individual galaxy entries are accompanied by multiple absorber recession velocities where $S > 1$). For the combined serendipitous and targeted CGM sample shown in Tables 2 and 3, $S = 1.4 \pm 0.2$ with no evidence for a significant difference in shadowing between the inner and outer half virial radii. This means that for a given value of the covering factor, the number of CGM clouds is 40% larger by taking shadowing into account. A modest amount of shadowing requires a modest filling factor if cloud sizes are much less than the virial radius. If the filling factor of CGM clouds were close to unity (which it is not), virtually every sight line would include multiple components (i.e., $S > 2$). There is no evidence for a different value of S for the dwarfs.

Based on these geometrical assumptions, the covering factor C is given by

$$C = \frac{N_{\rm cl} \times \pi r_{\rm cl}^2}{S \times \pi R_{\rm CGM}^2}, \quad (2)$$

where $N_{\rm cl}$ is the number of CGM warm clouds, $r_{\rm cl}$ is the median cloud radius, and $R_{\rm CGM}$ is the radius of the galaxy's CGM, which we take to be the virial radius. In this case, the volume filling factor (F) is given by

$$F = N_{\rm cl}\,\frac{4/3\pi r_{\rm cl}^3}{4/3\pi R_{\rm CGM}^3}. \quad (3)$$

Table 7
Model Parameters for Warm CGM Clouds

Subsample	$\langle L \rangle$ (L^*)	$\langle R_{vir} \rangle$ (kpc)	$\langle F \rangle$[a]	$\langle N_{cl} \rangle$[b]	$\langle \log M_{cl} \rangle$[c]	$\langle \log M_* \rangle$	$\langle \log M_{vir} \rangle$
Super-L^*	2.0	230–290	3%–6%	3000–4500	10.0–10.4	10.4–10.7	11.8–12.1
Sub-L^*	0.45	140–210	5%–10%	1000–1500	9.5–9.9	9.7–10.3	11.2–11.7
Dwarfs	0.03	70–120	0.5%–1%	150–250	7.8–8.3	8.8–9.6	10.3–11.0

Notes. All masses are given in units of $M_\odot$. Quantities listed as a range are calculated using virial radii determined from halo abundance matching and from Equation (1), respectively. Estimated errors in warm cloud masses are ± 0.2 dex for super-L^* and sub-L^* galaxies, and ± 0.5 dex for dwarfs.
[a] Volume filling factor of warm CGM clouds in the inner half ($R \leqslant 0.5\,R_{vir}$) of the CGM; the outer half ($0.5\,R_{vir} < R \leqslant R_{vir}$) has $\langle F \rangle$ values $\sim$8 times smaller.
[b] Total number of warm CGM clouds per galaxy with diameters $>$1 kpc. All super-L^* and sub-L^* galaxies have $\gtrsim$10,000 tiny clouds $\leqslant$1 kpc in size.
[c] Total mass per galaxy in warm CGM clouds.

Equations (2) and (3) imply that

$$N_{cl} = C \times S \times \frac{R_{CGM}^2}{r_{cl}^2} \quad (4)$$

and

$$F = C \times S \times \frac{r_{cl}}{R_{CGM}}. \quad (5)$$

By this formulation, the filling factor is given by the covering factor times the shadowing factor diminished by the ratio of cloud size to CGM size. The surface area and volume of an annular region (i.e., the outer half of the CGM: $0.5\,R_{vir} \leqslant \rho \leqslant R_{vir}$) are related slightly differently from the circular area and spherical volume assumed above, requiring small numerical correction factors of order unity to the above equations.

We combine the physical cloud parameters found in Table 6 with the covering factors shown in Figure 7 to estimate a mass per galaxy in warm CGM clouds. That is, we determine the range of cloud masses and their relative numbers in our sample based on the modeling results in Table 6 and assume that these model results are representative of the full cloud population. The observed covering and shadowing factors are then used to determine cloud numbers (Equation (4)) and filling factors (Equation (5)) for the various sizes of clouds found. While the covering factor is dominated by a large number of little clouds, the filling factor (and thus the mass) is dominated by the few bigger clouds, which are slightly more frequent in the inner half CGM volume. For the cloud sizes in Table 6, the overall filling factor is $\sim$15 times less than the covering factor in the absence of shadowing (modest shadowing and small cloud sizes require small CGM filling factors). The numbers of clouds and their masses as a function of cloud size then result in a total CGM mass in warm gas. We use the available data in two radial bins, $\rho \leqslant 0.5\,R_{vir}$ and $0.5\,R_{vir} < \rho \leqslant 1\,R_{vir}$, and two host galaxy luminosity bins (super-L^*+ sub-L^* and dwarfs). We have combined the super-L^* and sub-L^* absorber samples because these galaxies have similar CGM covering factors (Figure 7) and similar modeled cloud parameters (Figure 12). On the other hand, we have treated the inner and outer half CGM regions ($\rho < 0.5 R_{vir}$ and $0.5\,R_{vir} \leqslant \rho < R_{vir}$) separately to account for the slightly lower covering factor at larger radii (see Figure 7), the slightly lower average mass of modeled CGM clouds (Figure 13) and the significantly smaller number of absorbers modeled (Figure 8 and Table 6), Importantly, almost all of the Lyα-only absorbers are in the outer half virial radius. Most clouds at $0.5\,R_{vir} \leqslant \rho < R_{vir}$ had insufficient metal absorption-line detections to be modeled, which is likely due to these absorbers being physically smaller with smaller masses since they have smaller $N_{H\,I}$. We conclude that, despite the nearly twice larger volume projected onto the outer half virial radius, three-quarters of the CGM warm cloud mass is contained within the well-modeled inner half virial radius.

Table 7 shows the results of the mass estimates based on Equations (2)–(5) using cloud parameters based on the CLOUDY model results in Table 6 for the 24 clouds with multiple ion detections taken as representative of the CGM warm gas clouds as a whole. Data in Table 7 include by column (1) luminosity subsample; (2) median luminosity of the subsample in L^* units; (4) median virial radius (in kiloparsecs); (5) the filling factor of warm CGM clouds summed over cloud size within the inner half virial radius. The outer half has filling factors which are $\sim$8 times less than the values in this column; (6) the total number of CGM clouds with sizes $>$1 kpc; (7)–(9) the logarithm of the estimated total mass in CGM warm gas, in stars, and in baryons plus dark matter inside the virial radius (i.e., Column 9 is the "halo mass"), respectively. All masses are given in solar masses. All values are referenced to the median luminosity galaxy in each subsample. For quantities in Columns 3–9, the range of values given refers to the range of virial radii and halo masses assuming the two different prescriptions for these quantities presented in Section 3.1. The smaller values are from the halo-matching algorithm while the larger values are found by using Equation (1).

For all three luminosity bins, the estimated ensemble mass in warm photoionized CGM clouds is substantial. In the largest galaxies the CGM warm clouds contain $\sim 10^{10}\,M_\odot$ of gas, about half the amount of baryons as in the stars, gas and dust in the galaxy's disk. These masses are quite uncertain ($\pm$0.2 dex) since they depend on the small number of very massive CGM clouds in this sample and on their masses as determined by photoionization modeling. In turn this modeling depends on line strengths of H I and metal absorption lines measured in modest to good S/N spectra from STIS and COS, respectively. By comparing the column densities of key metal ions in DS08 and in other publications modeling the same absorbers (e.g., Tripp et al. 2002; Tilton et al. 2012), these measurements can differ by 10%–20%, affecting the modeling significantly. For example, Table 7 lists a cloud size for the 3C 273 absorber at $cz = 1585$ km s^{-1} that is $\sim$3 times larger than found by Tripp et al. (2002). However, we see no systematic variation in the cloud parameters determined from the COS spectra (which lack higher-order Lyman lines for accurate curve-of-growth H I

column densities) and the STIS spectra, which generally have significantly less S/N but, in conjunction with *FUSE* spectra, allow curve-of-growth determinations of hydrogen column density. The main uncertainty in the estimates in Table 7 is the modest number of CGM clouds which were successfully modeled by CLOUDY. This is particularly true for the dwarfs where only three absorbers in our sample have been modeled. For that subsample we estimate a larger uncertainty for the mass estimate in Table 7 of ±0.5 dex.

Because we have modeled these clouds entirely using their lower, largely photoionized ions, the total warm CGM mass in Column 6 does not explicitly include any "warm–hot" gas collisionally ionized by shock fronts associated with the motion of these clouds through a hotter substrate. O VI is detected in all but three serendipitous metal-bearing clouds (Table 3), as well as in the one targeted absorber for which a *FUSE* spectrum is available. This suggests that a "warm–hot" interface is associated with virtually all warm CGM clouds. The recent "COS-halos" study (Tumlinson et al. 2011) found a high covering factor of O VI to at least 0.5 $R_{\rm vir}$ in a sample of $L > L^*$ star-forming galaxies. The similar extent and covering factor of absorbers strongly suggests that these absorbers are related. From the recent Tumlinson et al. (2011) analysis, this hotter gas comprises a somewhat smaller, but still substantial, amount compared to the photoionized gas mass we find here.

The median luminosities for the super-L^* and sub-L^* samples bracket the total luminosity estimated for the Milky Way. Therefore, for the statistics, physical models, and halo-matching scalings adopted here, we expect that the Milky Way's CGM should extend to ∼200 kpc and should contain ∼2000 warm CGM clouds >1 kpc in size with a filling factor of order 4%. This inferred filling factor means that approximately one in every 25 Si III-absorbing HVCs should be located at distances of 50–150 kpc, rather than in the low halo (<10–20 kpc above the disk; Collins et al. 2009; Lehner & Howk 2011). Although much fewer in numbers than the Si III HVCs discovered and inventoried by Shull et al. (2009) and Collins et al. (2009), these more distant CGM clouds are estimated to contain an order of magnitude more mass (∼10^{10} $M_\odot$) than the highly ionized HVCs. Recently, Lehner & Howk (2011) have used background stars to infer that many highly ionized HVCs are close to the disk, ⩽20 kpc away. Because the detection rate of these HVCs is ∼50% in absorption against distant halo stars and the detection rate of Si III HVCs against extra-galactic targets is ∼80% (Shull et al. 2009), many Milky Way highly ionized HVCs do not have good constraints on their distances and so may be much more distant than 20 kpc above the disk. These covering factors leave open the possibility that the Milky Way has a distant (50–150 kpc), highly ionized, and much more massive CGM cloud population like we have found around other galaxies. Indeed, there is no reason to expect our Galaxy to be different in this respect.

5. DISCUSSION

5.1. The Baryon Budget in Spiral-rich Galaxy Groups

Rich clusters of galaxies are often considered to be fair samples of the universe due to their enormous size and deep gravitational potential wells. In this context, a related assumption is that clusters contain the cosmological baryon to dark matter ratio (White et al. 1993). Observationally, both in rich clusters and in smaller groups of galaxies dominated by massive ellipticals, the intra-cluster, and intra-group diffuse gas emits copious X-rays (Sarazin 1988; Mulchaey 2000) and contains most of the baryons (White et al. 1993). However, Mulchaey et al. (1996) failed to detect thermal X-rays from spiral-rich groups of galaxies and, based upon the lower velocity dispersion of spiral-rich groups compared to elliptical-dominated groups, they speculated that the only viable method for detecting such gas was through absorption lines in the spectra of bright background QSOs. While O VI 1032, 1038 Å absorption was specifically mentioned by them as likely transitions to conduct such a search, H I Lyα remains sensitive to diffuse gas at temperatures slightly in excess of 10^6 K, but requires high-S/N spectra to detect even modest column densities ($\log N_{\rm H\,I} \geqslant 13$), which imply total hydrogen columns $\log N_{\rm H} \geqslant 19$ due to the extremely small neutral fractions at $T > 10^6$ K.

Using a very high S/N (∼50) COS spectrum of PKS 0405−123, Savage et al. (2010) reported the discovery of the first broad, symmetrical O VI absorption which matches the Mulchaey et al. (1996) predictions quite well and is arguably the first detection of diffuse, hot gas in spiral groups. In this case, the very hot temperature of this gas is required both by the line width of the symmetrical O VI absorption and the absence of detectable Lyα. The broad O VI absorber in PKS 0405−123 lies at $\rho > 100$ kpc in projection from two late-type galaxies and also has associated warm-gas absorption at $cz = 50, 105$ km s^{-1} which is included in Tables 3 and 6 (see also Prochaska et al. 2004). In another high-S/N COS spectrum, a broad Lyα (BLA) absorption was found in HE 0226−4110 by Savage et al. (2011a) blended with strong, much narrower Lyα associated with warm, photoionized gas. The BLA appears associated with much hotter gas including O VI and Ne VIII absorptions. A few other BLAs blended with narrower Lyα have already been found in an ongoing search of all high-S/N COS spectra (Savage et al. 2011b; C. W. Danforth et al., in preparation). The relatively strong O VI absorptions ($\log N_{\rm O\,VI} \geqslant 14.2$) discovered by Tumlinson et al. (2011) are not the same absorber type as the broad, shallow O VI seen by Savage et al. (2010), and may actually mask the presence of the broad, shallow absorption in many cases even in relatively high-S/N spectra (Savage et al. 2011b).

The COS UV spectrograph on *HST* is sensitive enough that a full accounting of BLAs and broad, shallow O VI absorptions can be made. This census can confirm the apparent abundance of BLAs tentatively seen at lower S/N with STIS (Richter et al. 2004; Lehner et al. 2007; Danforth et al. 2010). A large number of BLAs per unit redshift are expected if these are detections of hot, extended gas in spiral-rich groups. Because spiral-rich groups far exceed elliptical-dominated groups and clusters in number density, the detection of a massive intra-group medium in spiral groups could contribute a significant number of baryons to the universal budget (∼20%; Savage et al. 2010).

Here we have found strong evidence for high covering factor warm gas clouds around galaxies of all luminosities and used their derived properties from photoionization modeling to infer the mass in these clouds. We find no strong distinctions between the warm CGM cloud properties around late-type galaxies of differing luminosities at $L \geqslant 0.1\,L^*$. While warm clouds are detected around dwarfs, the current statistics are poor. We find no strong evidence for warm clouds around early-type galaxies at all (but see Thom et al. 2012). Using the results of our warm gas CGM inventory in Table 7, Table 8 shows our best estimates for the percentage of baryons in the various reservoirs in spiral galaxies of varying luminosities. This table uses the results on the CGM from this survey and results from other works to characterize the location and physical conditions of the baryons

Table 8
Spiral Galaxy Baryon Inventory

Subsample	$\log M_{vir}$	$\log M_{bar}$	M_*/M_{bar}	M_{warm}/M_{bar}	$M_{O\,VI}/M_{bar}$	$M_{coronal}/M_{bar}$	$M_{missing}/M_{bar}$
Super-L^*	11.8	11.0	20%	10%	6%	$\leqslant$10%	$\gtrsim$50%
Sub-L^*	11.2	10.4	20%	15%	[9%]	[$\leqslant$10%]	$\gtrsim$50%
Dwarfs	10.3	9.5	20%	<5%	[<1%]	[$\leqslant$10%]	$\gtrsim$65%

Notes. All masses are given in units of $M_\odot$. All values use M_{vir} and R_{vir} from the halo-matching technique. All percentage values are approximate.

detected thus far in late-type galaxies. The stellar baryon fraction is taken to be 20% for all galaxies based on a constant mass-to-light ratio of $M/L \approx 1$–2 in solar units but could be a somewhat smaller fraction in lower luminosity galaxies (Moster et al. 2012). Molecular and atomic disk gas and dust usually are a small fraction of the total and HVCs detected in 21 cm emission are likewise a negligible amount, although the percentage of baryons in these reservoirs could be much more significant in dwarfs (Peeples & Shankar 2011). A detailed accounting of the relative number of baryons in stars and disk gas as a function of galaxy mass is beyond the scope of this paper; therefore, these collapsed baryon reservoirs are included with the stars in Table 8 and are assumed to total 20% of the baryon inventory (Fukugita et al. 1998; Shull et al. 2012) for all three luminosity subsamples.

The 10%–15% baryon fraction estimate for warm CGM clouds in luminous galaxies is based on the accounting and photoionization modeling in this paper but also assumes that the "Lyα-only" clouds are physically similar to the modeled clouds and that their lower $N_{H\,I}$ values correspond to smaller sizes and masses as the modeled clouds. It is possible that these lower column density H I clouds could be much more highly ionized (O VI is detected in many of them) and more massive than the clouds we have modeled using CLOUDY. If this is the case, the values in Column 5 may somewhat underestimate the warm CGM cloud mass. The 6% estimate of hot, collisionally ionized gas in luminous galaxies comes from the recent Tumlinson et al. (2011) "*HST*/COS halos survey." The O VI absorption found by that group has a similarly high covering factor and physical extent around galaxies as the warm clouds we have detected, so it is natural to suggest a relationship between the two. Indeed, where O VI could be detected in these clouds it usually was detected (only five firm non-detections in Tables 3 and 4). Although the photoionized and the shock-heated gas may overlap considerably, creating a "double-counting" of baryons issue, CGM clouds and their shocked interfaces may account for as much as 15%–25% of all massive spiral galaxy baryons. Since the Tumlinson et al. (2011) survey observed only the most massive galaxies, the other listings in Column 6 of Table 8 are extrapolations to lower luminosities based on assuming a scaling between the warm CGM clouds and the warm–hot gas seen in high-column density O VI absorption. These scaled values are shown in brackets to indicate that they are not based on actual observations and are quite uncertain.

Table 8 includes the following information by column: (1) luminosity subsample; (2) the logarithm of the total virial mass (M_{vir}; dark matter + baryons) in solar masses; (3) the logarithm of the baryonic mass (M_{bar}) in solar masses determined by assuming that a late-type galaxy contains the 5:1 cosmic ratio of dark matter to baryons (Larson et al. 2011); (4) the baryon fraction in stars and disk gas and dust (Fukugita et al. 1998; Peeples & Shankar 2011) as discussed above; (5) the baryon fraction in warm CGM clouds; (6) the baryon fraction in WHIM gas probed by strong O VI (Tumlinson et al. 2011) assuming no "double counting" with the warm, photoionized baryons. Estimates in brackets are scaled values assuming the same fraction of the warm cloud mass as seen in the massive galaxies; (7) the limit on the percentage of very hot ($T \gtrsim 10^7$ K) coronal gas around spirals set by the failure to detect hot ($kT \sim 300$ eV) gas around the Milky Way or other nearby galaxies (Bregman 2007; Anderson & Bregman 2010); but see Anderson & Bregman (2011) and the discussion of Gupta et al. (2012) below. Since this limit is set by observations of Milky-Way-sized galaxies, the value for dwarfs is a very uncertain extrapolation and is listed in brackets for that reason; (8) the percentage of "missing baryons" assuming that the stars, CGM warm clouds, CGM warm–hot interface gas traced by O VI and coronal gas potentially detected in X-rays are the only major reservoirs and also assuming that spirals and other late-type galaxies are "closed boxes" for which the cosmic ratio of baryons to dark matter applies (but see below). That is, Column 8 is 100% minus the sum of Columns 4–7. The values in the last column are all shown as approximate due to the substantial uncertainties for the values in the preceding columns. By this accounting we confirm that the amount "missing" is large.

The listings in Table 8 use the total virial mass and the virial radius values calculated using the halo-matching scalings shown in Figure 1. The scalings from Equation (1) yield similar baryon percentages because all mass amounts scale upward by a similar amount under that assumption (see Section 3.1).

The hot gas ($T \gtrsim 10^6$ K) predicted by Mulchaey et al. (1996) and potentially discovered by Savage et al. (2010, 2011b) using high-S/N COS spectra is a candidate for this "missing baryon" reservoir. If this hot gas extends over the full virial radius of a spiral-rich group (400 kpc radius is assumed here), it could contain as much as $7 \times 10^{11}\ M_\odot$ of baryons (Savage et al. 2010); this is enough to account for the "missing baryons" in an entire spiral-rich galaxy group. Since we have seen that warm CGM clouds likely are infalling and outgoing through the virial radius of an individual spiral galaxy, a single galaxy is not necessarily a closed box and so may not sample the cosmological ratio of baryons to dark matter individually. The largest extent of metal-enriched gas away from galaxies is probed by H I + O VI absorbers, which are found up to ~800 kpc from luminous galaxies (see Section 4.2 and Figure 11). Since this is comparable to the physical size of a spiral-rich group, it is possible that metals are not spread beyond the extent of a single group of galaxies. Also the warm cloud kinematics shown in Figures 8–11 shows that even the CGM clouds with the largest $|\Delta v|$ only modestly exceed v_{esc}. Based on the current census, it is likely that most CGM clouds are confined to a single galaxy group and do not escape into the diffuse IGM. Therefore, a case can be made that a region the size of an entire spiral-rich group like the Local Group can be considered a "closed box"

for baryon content and chemical evolution modeling. If significant amounts of gas and metals escape beyond the bounds of spiral-rich groups, this process could have occurred mostly at higher redshifts and earlier cosmic times when the spiral-group gravitational potential well had not developed fully.

Using the halo-matching scaling in Figure 1 a spiral-rich group with a total luminosity of a few L^* has a total halo mass of $10^{12.7}$–$10^{13.0}$ $M_\odot$ and a total baryonic mass 0.8 dex less than that amount. The reservoir of hot gas suggested by the Savage et al. (2010, 2011b) detections amounts to $\sim 7 \times 10^{11}$ $M_\odot$ of gas or 40%–80% of the baryons predicted to be present in such a group. Thus, this hot gas reservoir could account for the remaining "missing baryons" in spiral galaxy systems. If present, this hot gas would also be the largest baryon reservoir in such systems, a factor of two or more larger than all the stars, gas, and dust in the disks of the group galaxies combined.

Indirect evidence for the existence of a very extensive hot gas surrounding late-type galaxies is shown in Figure 14, which displays warm CGM cloud pressure as a function of scaled impact parameter. There is no obvious trend in this plot despite declining cloud sizes and masses as a function of scaled impact parameter (see Figures 12 and 13) as well as declining Lyα absorption W_λ with impact parameter (Figure 9). If these warm clouds are in near pressure equilibrium with a hot diffuse gas, then such a flat pressure profile is unexpected unless either the scale height of this gas is much larger than the virial radii of the more luminous galaxies in this sample (i.e., $\geqslant$200–300 kpc in radius) and/or the density profile of this hot gas is unexpectedly flat with radius from these galaxies (Fang et al. 2013). Since the latter hypothesis may require an unphysically flat mass profile, this speculation, and the cloud pressure data from the CLOUDY modeling which support it, must be treated with some caution until confirmed by new observations.

Neither circumstance (large scale height or flat density profile) is observed for the hot coronal gas detected around the Milky Way (Bregman 2007) where scale heights of only a few kiloparsecs are inferred. Also very extended X-ray emitting halos have not been detected in general around nearby spiral galaxies (Bregman 2007; Anderson & Bregman 2010). But X-ray imagers are not sensitive to gas with temperatures near 10^6 K, so that very extended gas could be present and remain largely undetectable to *Chandra* or *XMM-Newton*. Given the median pressure shown in Figure 14 ($P/k \approx 10\,\mathrm{cm}^{-3}$ K) over a size $\geqslant$300 kpc, and by assuming pressure balance between warm CGM clouds and this putative hot diffuse gas at $T \sim 10^6$ K, then the total baryonic mass of this gas is $\geqslant 2 \times 10^{11}$ $M_\odot$. The density, pressure, temperature, and total hot gas mass inferred from pressure balance with warm CGM clouds are in close agreement with the very recent, adiabatic model of Fang et al. (2013). This amount is comparable to the "missing baryons" in a spiral galaxy group.

Recently, Gupta et al. (2012) reanalyzed the X-ray spectroscopy of eight bright AGNs which all probe the Galaxy halo and Local Group CGM. Although the location, size and thus mass of the O VII absorption found in these spectra at $\log N_{\mathrm{O\,VII}} \approx 16$ is controversial, this column density in O VII is close to the amount predicted by the O VI column density found by Savage et al. (2010, 2011b) if $T \sim 10^6$ K; i.e., this Local Group detection could be very extended hot gas consistent with the broad, shallow O VI found in other spiral-rich groups. Gupta et al. (2012) suggest that if the O VII extent is $\geqslant$150 kpc it would have a very large mass $>10^{11}$ $M_\odot$ (see also Fang et al. 2013), similar to what we calculate based on both the PKS 0405−123 broad O VI absorber and on the warm CGM cloud pressures.

However, other non-detections appear inconsistent with this interpretation. Excepting a possible *Chandra* detection of O VIII in the PKS 2155−304 sight line (Fang et al. 2007), only one other plausible detection of O VII has been made with the *Chandra* and *XMM-Newton* spectrometers (Buote et al. 2009). If this hot gas is a common feature of most or all spiral groups, it should have been detected in X-ray absorption lines along other sight lines, and has not been, even in co-added *Chandra* spectra (Yao et al. 2010). But current X-ray spectrometers have limited spectral resolution and poorly characterized systematic noise (Yao et al. 2012), so that non-detections may be due primarily to these issues at the current time. Better spectral resolution using well-characterized detectors are necessary to make advances in this field at X-ray wavelengths. On the other hand, a sensitive COS census of BLAs and broad O VI absorbers is possible and should find $d\mathcal{N}_{\mathrm{BLA}}/dz \approx$ 10–20 per unit redshift if spiral-rich groups contain significant amounts (and extents) of hot gas. A solid measurement of the $d\mathcal{N}/dz$ for such systems can help infer their sizes, confirming the large hot gas masses suggested here. A BLA search using COS is currently underway using only high-S/N (>20:1) spectra (C. W. Danforth et al., in preparation).

5.2. Input for Galactic Chemical Evolution Models

Any accurate accounting of the mass infall and outflow rates into and out of spirals is premature due to the uncertainty in the physical structure, kinematics, metallicity, and thus origin for many CGM clouds in our sample. While metal-enriched and Lyα-only clouds are present in the current CGM cloud sample, the distinction between these two types is not well defined owing to the limited S/N of the UV spectroscopy used. Lyα-only clouds could be enriched at levels similar to the metal-bearing clouds but with their metal absorption lines currently undetectable given their generally lower H I column densities (for examples, see Section 4.4.1 and Keeney et al. 2012). However, the most basic prediction coming from Galactic chemical evolution models, the necessary accretion of low-metallicity gas, finds some preliminary support from this study. Only four good examples of low-metallicity gas in the CGMs of $\gtrsim L^*$ spirals have been found using current data (see Section 4.4.1). This suggests that higher S/N COS spectroscopy will be able to characterize many other examples of gas infall by detecting metal absorption at levels significantly below the metallicity of the host galaxy (i.e., at <10% solar for an L^* galaxy). Since low-metallicity gas has already been detected in the Milky Way halo (e.g., Complex C; Richter et al. 2001; Collins et al. 2007; Shull et al. 2011), external galaxy CGM studies using high-S/N COS spectroscopy can add a statistical accounting of the amount of gas accreted, outflowing and recycling to generalize the Milky Way results to other spirals.

What is possible now is a first, rough accounting of the amount of "galactic fountain" gas which is being recycled in the CGM of these galaxies. In Section 4.4 based on the data shown in Figure 8, we identified nine CGM absorbers as good candidates for high-metallicity recycling gas, which are ∼15% by number and ∼40% by mass of our full CGM cloud sample. This fraction is a lower limit on the recycling gas mass since there are almost certainly other recycling gas clouds which have not been identified unambiguously by our accounting. Assuming that $\gtrsim$40% of the mass of the CGM is in recycling

gas and using the total warm baryonic CGM cloud mass in Table 7 for a 2 L^* galaxy (and ignoring any modest contribution from shock-excited gas traced by O VI to be conservative), a typical super-L^* galaxy is recycling $\gtrsim 4 \times 10^9\ M_\odot$ of high-metallicity gas, about half of which is infalling at any one time. Based on their locations in Figure 8(a), we assume that the infalling high-metallicity "galactic fountain clouds" are falling ballistically from a total distance of ~100 kpc at a median total speed of ~30 km s^{-1} (i.e., correcting the impact parameter and radial velocity difference to 3D quantities statistically). Thus, recycling CGM gas can provide $\gtrsim 0.6\ M_\odot\ \mathrm{yr}^{-1}$ of enriched gas accretion onto the galactic disk. Scaling this result to a Milky-Way-size galaxy predicts $\gtrsim 0.3\ M_\odot\ \mathrm{yr}^{-1}$ of infalling, recycling gas, about one-third or more of the infall rate estimate from Si III-absorbing HVCs (Shull et al. 2009). Comparing the estimated accretion rate we have obtained with the total infalling gas estimate based on Si III HVCs suggests an origin for the remaining $\lesssim 0.7\ M_\odot\ \mathrm{yr}^{-1}$ from outside the galaxy. This is not at all unexpected given the example of several Milky Way HVCs like Complex C. Increasing the sample size of CGM absorbers at $\rho \leqslant 0.5\ R_{\rm vir}$ by targeting new, close QSO/galaxy pairs will allow a substantial increase in the known population of CGM clouds which are recycling galactic gas and will improve this crude, first estimate.

Because we have found evidence for a larger reservoir of hot, metal-enriched gas in spiral galaxy groups (Savage et al. 2010), any gas expelled from dwarfs and spirals may largely accumulate there. Due to the lower escape speeds for lower mass galaxies, much of this hot gas could come from dwarfs in the group. The lower covering factor and much smaller total masses of CGM clouds around dwarfs found in Sections 3.3 and 5.1 are modest support for this picture. At present there are only a couple examples of absorbing gas escaping from dwarf galaxies in this sample, but any accretion of gas onto larger spirals probably comes mostly at the expense of nearby, lower luminosity, lower metallicity galaxies in the same galaxy group. Low-metallicity absorbers accreting at much higher velocities (open circles at $\rho/R_{\rm vir} = 0.5$–1.0 and $|\Delta v| \approx 0.3$–$1.0\ v_{\rm esc}$) may make up the additional $\lesssim 0.7\ M_\odot\ \mathrm{yr}^{-1}$ of infalling gas required by the current rate of Milky Way star formation. This suggests that, while the Milky Way is not a "closed box" for galaxy evolutionary models, the Local Group might be. Since the star formation histories of local dwarfs (Mateo 1998; Skillman 2005) as well as the histories of our Galaxy and M31 (Dalcanton et al. 2012) are now being constructed, it may be possible in the near future to construct a chemical evolution model for the entire Local Group assuming overall mass conservation.

6. SUMMARY

In this study we have used two samples of absorbers near galaxies found with *HST* to investigate and characterize the CGM of low-z, late-type galaxies. The COS GTO Team has observed 11 QSOs projected near foreground galaxies, detecting warm, photoionized gas around all 10 $L < L^*$ spiral and irregular galaxies probed by these *HST*/COS spectra. These galaxies include modest starbursts, normal spirals and dwarfs, and one LSB galaxy. There are no obvious distinctions between the absorptions found around any of these different types. Absorbers range from "Lyα-only" clouds at $\log N_{\rm H\,I} \approx 13.5$, where we find no metals detected in available spectra, to an LLS with numerous metal detections and $\log N_{\rm H\,I} \approx 18.5$. H I Ly$\alpha$ and metal ions typical of photoionized "warm" clouds are detected in many of these absorbers, but higher ions like C IV and Si IV typically have larger equivalent widths than lower ions like C II and Si II, indicative of ionization parameters for these clouds of $\log U = -2.0$ to -3.5.

In order to increase the sample size of CGM absorbers, particularly at $L > L^*$, and to investigate a more random selection of galaxy CGMs, we have gathered a "serendipitous" CGM cloud sample of ~60 absorbers using the *HST*/STIS sample compiled by DS08 from 35 well-observed sight lines, most of which also have *FUSE* spectroscopy. The *FUSE* data are important, providing coverage of the higher Lyman lines (and accurate $N_{\rm H\,I}$ values from the curve-of-growth technique) and the important O VI ion, sensitive to diffuse photoionized or collisionally excited gas. A few absorbers were found to have Lyman-limit decrements in their *FUSE* spectra. The targeted *HST*/COS QSOs do not (except for one) have complementary *FUSE* data. The CGM absorbers discovered in these serendipitous spectra are similar to the targeted absorbers. While the spectra, line measurements and detailed absorber modeling and host galaxy properties are presented elsewhere (Paper II), in this paper we presented the analysis of these data, which leads to the following conclusions.

1. Only ~5% of all Lyα absorbers are projected close enough to galaxies to probe their CGM; i.e., most Lyα absorbers are IGM not CGM if the virial radius is taken as the rough dividing line between these two populations (Section 3.2).
2. The covering factor of warm gas clouds inside the virial radius of late-type galaxies is very high, consistent with unity inside 0.5 $R_{\rm vir}$ and ~75% between 0.5 $R_{\rm vir}$ and $R_{\rm vir}$ for luminosities $\geqslant 0.1\ L^*$. These high covering factors are consistent with the ubiquity of Lyα absorbers found in both the COS-targeted survey presented here and other recent surveys (Prochaska et al. 2011b; Tumlinson et al. 2011). While CGM detections and statistics are sparse for dwarf galaxies at $L < 0.1\ L^*$, the covering factors around dwarfs are still substantial, ~50% inside $R_{\rm vir}$ (Section 3.3).
3. We find no strong evidence for warm CGM clouds around early-type galaxies (but see Thom et al. 2012); the only three candidate early-type galaxies associated with absorbers in this sample all have late-type galaxy alternate identifications (Section 4.1).
4. While this survey uses a similar galaxy and absorber database as Stocke et al. (2006), new galaxy survey work (chiefly new SDSS data releases and Prochaska et al. 2011b) allows a reassessment of the extent of O VI absorbers away from galaxies which confirms our earlier results. We find that the O VI absorption screen around galaxies is patchy with an approximate covering factor ~0.3 at $\log N_{\rm O\,VI} \geqslant 13.2$ out to 3.5–4 $R_{\rm vir}$ around galaxies of all luminosities. While the current data are still sparse at low galaxy luminosities, we extrapolate that dwarfs and sub-L^* galaxies are the major sources for O VI absorbers (Sections 3.4 and 4.2, Figure 11).
5. The merged sample of COS-targeted and STIS-serendipitous absorbers allows a detailed characterization of the CGM of late-type galaxies from super-L^* spirals to sub-L^* spirals and irregulars and, with limited statistics, to dwarfs at $L < 0.1\ L^*$. Inside 0.5 $R_{\rm vir}$ almost all absorbers detected are "metal-bearing" and many have velocities too low to easily escape from the host galaxy. Even without knowing their direction of motion we identify nine of these clouds as likely recycling "galactic fountains." A few absorbers have metallicities <0.2 solar, too low to be easily ascribed to gas originating in their nearby "host" galaxy and a few absorbers can be identified unambiguously as

gas originating in the host galaxy which is escaping into the IGM. These galactic wind candidates have metallicities comparable to their associated galaxy's metallicity and high radial velocities with respect to their associated galaxy ($|\Delta v| > v_{esc}$). Because of the limited S/N of the UV spectra, some of the COS-targeted absorbers and most of the STIS-serendipitous absorbers cannot be so easily classified. A complete accounting of the origin and fate of CGM clouds must await new absorber samples found in higher-S/N (>20:1) COS spectra (Section 4.2).

6. Photoionization (CLOUDY) modeling of those 24 targeted and serendipitous absorbers with multiple ionization states of the same element (at least two of Si II/Si III/Si IV or C II/C III/C IV) finds CGM cloud ionization parameters of $\log U = -2.0$ to -3.5, typical metallicities of 10%–100% solar values, total cloud densities of $n_H = 10^{-3}$ to 10^{-4} cm^{-3}, cloud diameters of 0.1–30 kpc, and masses of 10–10^8 $M_\odot$ (see also Paper II). The small clouds are best sampled by this survey as they provide the largest covering factor, while the massive clouds provide the greatest filling factor (5%–8% for the most massive galaxies) and the most total mass. However, there are only 10 of these large ($\gtrsim$3 kpc), massive ($\gtrsim 10^5$ $M_\odot$) clouds in this sample which means that the total CGM mass in warm gas is not very tightly constrained. Also $\gtrsim$50% of the CGM clouds do not have sufficient metal absorption to provide adequate input for modeling. For this study, we have assumed that these unmodeled clouds ("Lyα-only" clouds or clouds with only marginal metal-line detections) have similar physical conditions to the modeled clouds (Section 4.3).
7. Unlike the geometry created by observing Milky Way HVCs and highly ionized HVCs from a location inside the distribution of these clouds, very large covering factors of external galaxy CGMs do not translate into near unity filling factors. In the simple viewing geometry assumed herein, the filling factor depends on the covering factor, the mean number of clouds detected in any one CGM and the ratio of cloud size to the size of the CGM (see Equations (2)–(5) in Section 4.5). For a Milky-Way-size galaxy we estimate a CGM volume filling factor of ~4%, which means that only a small fraction of highly ionized Si III HVCs (Collins et al. 2009; Lehner & Howk 2011) are much more distant CGM clouds. This is consistent with Lehner & Howk's recent result, which places many (but not all) Si III HVCs within a few kpc of the galactic disk. A low filling factor is also consistent with our observation that only a few CGM absorbers have multiple velocity components (Section 4.5).
8. Based on our analysis, which includes derived filling factors and CGM warm cloud parameters, a Milky-Way-size galaxy has ~10^{10} $M_\odot$ of warm CGM clouds in its "halo" (inside its virial radius). Placing the warm CGM cloud population studied here into the overall context of the baryon inventory of spiral galaxies finds that the warm CGM can account for ~10%–15% of the full baryon content of luminous spiral galaxies assuming that these systems contain the cosmic ratio of baryons to dark matter. Including the amount of "warm–hot" gas traced by O VI recently found around luminous spirals by Tumlinson et al. (2011), and assuming minimal "double counting" between these two reservoirs, means that the CGM contains a total number of baryons comparable to those present in galactic disks, including stars, gas, and dust (see Tables 7 and 8; Sections 4.5 and 5.1).
9. Although our survey contains only a modest number of absorbers associated with dwarf galaxies, we tentatively conclude that warm CGM clouds account for $\leqslant$5% of the baryons in dwarf galaxies. Comparing this result with the massive warm CGMs we have found around more luminous galaxies suggests that many of the warm CGM clouds escape from the dwarfs into the IGM.
10. Adding in a maximum allowable 10% of very hot ($T \approx 10^7$ K) coronal gas near spiral galaxies (Bregman 2007; Anderson & Bregman 2010) leaves $\gtrsim$50% of spiral galaxy baryons unaccounted for. The recent COS discovery of very broad Lyα and broad O VI-absorbing gas at $T > 10^6$ K by Savage et al. (2010, 2011b), and the suggestion based on STIS spectroscopy that BLAs may be quite plentiful (Richter et al. 2004; Lehner et al. 2007; Danforth et al. 2010), leads to the hypothesis that the Local Group and other spiral-rich groups could contain $\gtrsim 10^{11}$ $M_\odot$ of very hot gas, analogous to the intra-cluster and intra-group medium detected in elliptical-dominated clusters and groups (see also Fang et al. 2013; Gupta et al. 2012). If a spiral intra-group medium of this amount is also ubiquitous, these gaseous reservoirs are a significant fraction (~20%) of the universal baryon inventory. Mulchaey et al. (1996) had predicted that this spiral group gas was most easily detectable as O VI absorption in the spectra of background QSOs. This prediction now has tantalizing confirming evidence in a couple of cases (Savage et al. 2010, 2011b). Analysis of high-S/N COS spectroscopy currently underway (C. W. Danforth et al., in preparation) can confirm this conjecture (Section 5.1).
11. Indirect support for the existence of a hot ($T \sim 10^6$ K), extensive (>300 kpc), and thus massive spiral intra-group medium comes from the analysis of the physical structure of the warm, photoionized CGM clouds in our sample. Figure 14 shows that, despite having slightly declining cloud sizes and masses with increasing impact parameter, CGM clouds show no clear evidence for a strongly declining pressure with impact parameter. If these clouds are in pressure equilibrium with an external intra-cloud medium, then the pressure of that medium must also be nearly constant with radius away from the galaxy to a distance comparable to the virial radii of these systems (~150–250 kpc for sub-L^* and super-L^* galaxies). The pressures shown in Figure 14 do suggest a rather flat density profile with radius which may be unphysical and so these results from the CLOUDY modeling of warm CGM clouds and its interpretation must be treated with some caution. However, see supporting evidence in Fang et al. (2013) and Gupta et al. (2012) for this hot gas in our own Local Group. Nevertheless, by applying pressure balance and assuming $T \approx 10^6$ K and a gaseous extent of >300 kpc in radius suggested by Figure 14 finds $> 7 \times 10^{11}$ $M_\odot$ of gas, sufficient to account for most if not all of the "missing baryons" in spiral galaxies. An accurate inventory of BLAs and broad O VI absorption can independently confirm very large cross-sectional absorbing areas for these systems (Section 5.1).
12. Although a robust accounting of the kinematics, metallicity (relative to the host galaxy), and thus origin and fate of individual CGM clouds is not yet possible, this analysis has provided some tentative information on the gas that fuels star formation in late-type galaxies. Specifically, we estimate that low impact parameter, low Δv, high-metallicity clouds plausibly associated with "galactic fountains"

account for $\gtrsim$0.3 $M_{\odot}$ yr^{-1} of gas infall rate in Milky-Way-size galaxies. This amount is nearly one-third of the amount found in the close-in HVC population to be infalling onto the Galactic disk (Shull et al. 2009). While this suggests that the bulk of the accreting gas comes from outside the system, we were able to identify only a very few (4) plausible examples of infalling, low-metallicity gas clouds from this sample at this time. To identify these infalling, low-metallicity clouds definitively will require both higher-S/N COS spectroscopy to determine cloud metallicities to levels < 0.1 solar and also accurate host galaxy metallicities from ground-based spectroscopy. Nevertheless, this study offers tantalizing preliminary evidence for the detection of low-metallicity gas accretion required by Galactic chemical evolution models (Larson 1972; Chiappini et al. 2001, Section 5.2).

The present work is a start to the process of characterizing the CGM of spiral galaxies. A more definitive characterization of the CGM will require an *HST*/COS QSO/galaxy survey using ~500–1000 orbits to explore the parameter space of galaxy luminosity (and thus mass and virial radius extent), galaxy type, SFR, and metallicity. High S/N values (>20:1) are essential for accurate warm cloud models, cloud metallicities (in comparison with "host" galaxy metallicities), physical extents around galaxies, and importantly to search for broad, shallow absorption indicative of hot, spiral intra-group gas. Detailed study of spiral groups with known or suspected hot gas reservoirs is required to make a definitive confirmation; i.e., the gas temperature derived from the absorption line widths should be comparable to the velocity dispersion of the galaxies in these groups. Several possible BLAs in spiral groups identified herein can provide a viable test of the presence of a massive spiral intra-group gas. A detailed census of the warm and hot CGM in late-type galaxy groups is a necessary piece to construct an accurate model for galactic structure and evolution.

This work was supported by NASA grants NNX08AC146 and NAS5-98043 to the University of Colorado at Boulder for the *HST*/COS project. B.A.K. gratefully acknowledges additional support from NSF grant AST1109117. Further, we gratefully acknowledge M. Trenti for halo abundance matching expertise and results, and J. Werk, Y. Yao, and J. Bullock for helpful conversations. This research has made use of the NASA/IPAC Extragalactic Database (NED), which is operated by the Jet Propulsion Laboratory, California Institute of Technology, under contract with the National Aeronautics and Space Administration.

Facilities: HST (COS, STIS), *FUSE*, WIYN (HYDRA), ARC (SPIcam, DIS)

REFERENCES

Aguirre, A., Schaye, J., & Theuns, T. 2002, ApJ, 576, 1
Anderson, M. E., & Bregman, J. N. 2010, ApJ, 714, 320
Anderson, M. E., & Bregman, J. N. 2011, ApJ, 737, 22
Bahcall, J. N., Bergeron, J., Boksenberg, A., et al. 1993, ApJS, 87, 1
Binney, J., & Tremaine, S. 1987, Galactic Dynamics (Princeton, NJ: Princeton Univ. Press), 567
Bland-Hawthorn, J., & Maloney, P. R. 1999, ApJL, 510, 33
Blitz, L., Spergel, D. N., Teuben, P. J., Hartmann, D., & Burton, W. B. 1999, ApJ, 514, 818
Bouché, N., Hohensee, W., Vargas, R., et al. 2012, MNRAS, 426, 801
Bowen, D. V., Tolstoy, E., Ferrara, A., Blades, J. C., & Brinks, E. 1997, ApJ, 478, 530
Bregman, J. N. 2007, ARA&A, 45, 221
Buote, D. A., Zappacosta, L., Fang, T., et al. 2009, ApJ, 695, 1351
Cen, R., & Ostriker, J. P. 1999, ApJ, 514, 1
Chen, H-W., Lanzetta, K. M., & Webb, J. K. 2001, ApJ, 556, 158
Chen, H.-W., Lanzetta, K. M., Webb, J. K., & Barcons, X. 1998, ApJ, 498, 77
Chen, H.-W., & Mulchaey, J. S. 2009, ApJ, 701, 1219
Chen, H.-W., Wild, V., Tinker, J. L., et al. 2010, ApJL, 724, 176
Chiappini, C., Matteucci, F., & Romano, D. 2001, ApJ, 554, 1044
Chomiuk, L., & Povich, M. S. 2011, AJ, 142, 197
Churchill, C. W., Mellon, R. R., Charlton, J. C., et al. 2000, ApJ, 543, 577
Collins, J. A., Shull, J. M., & Giroux, M. L. 2004, ApJ, 605, 216
Collins, J. A., Shull, J. M., & Giroux, M. L. 2007, ApJ, 657, 271
Collins, J. A., Shull, J. M., & Giroux, M. L. 2009, ApJ, 705, 962
Côté, B., Martel, H., Drissen, L., & Robert, C. 2012, MNRAS, 421, 847
Cowie, L., & Songaila, A. 1998, Natur, 394, 44
Dalcanton, J. J., Williams, B. F., Lang, D., et al. 2012, ApJS, 200, 18
Danforth, C. W., & Shull, J. M. 2005, ApJ, 625, 555
Danforth, C. W., & Shull, J. M. 2008, ApJ, 679, 194 (DS08)
Danforth, C. W., Stocke, J. T., & Shull, J. M. 2010, ApJ, 710, 613
Davé, R., Hernquist, L., Katz, N., & Weinberg, D. H. 1999, ApJ, 511, 521
Davé, R., & Oppenheimer, B. D. 2007, MNRAS, 374, 427
Diehl, R., Halloin, H., Kretschmer, K., et al. 2006, Natur, 439, 45
Eisenstein, D. J., Weinberg, D. H., Agol, E., et al. 2011, AJ, 142, 72
Fang, T., Bullock, J. S., & Boylan-Kolchin, M. 2013, ApJ, 762, 20
Fang, T., Canizares, C. R., & Yao, Y. 2007, ApJ, 670, 992
Ferland, G. J., Korista, K. T., Verner, D. A., et al. 1998, PASP, 110, 761
Fukugita, M., Hogan, C. J., & Peebles, P. J. E. 1998, ApJ, 503, 518
Gehrels, N. 1986, ApJ, 303, 336
Giroux, M. L., & Shull, J. M. 1997, AJ, 113, 1505
Green, J. C., Froning, C. S., Osterman, S., et al. 2012, ApJ, 744, 60
Grevesse, N., Asplund, M., Sauval, A. J., & Scott, P. 2010, Ap&SS, 328, 179
Gupta, A., Mathur, S., Krongold, Y., Nicastro, F., & Galeazzi, M. 2012, ApJL, 756, 8
Haardt, F., & Madau, P. 2012, ApJ, 746, 125
Heckman, T. M., Lehnert, M. D., Strickland, D. K., & Armus, L. 2000, ApJS, 129, 493
Impey, C. D., Petry, C. E., & Flint, K. P. 1999, ApJ, 524, 536
Jannuzi, B. T., Bahcall, J. N., Bergeron, J., et al. 1998, ApJS, 118, 1
Jenkins, E. B., Bowen, D. V., Tripp, T. M., et al. 2003, AJ, 125, 2824
Kacprzak, G. G., Churchill, C. W., Barton, E. J., & Cooke, J. 2011, ApJ, 733, 105
Kacprzak, G. G., Churchill, C. W., Ceverino, D., et al. 2010, ApJ, 711, 533
Keeney, B. A., Momjian, E., Stocke, J. T., Carilli, C. L., & Tumlinson, J. 2005, ApJ, 622, 267
Keeney, B. A., Stocke, J. T., Rosenberg, J. L., Tumlinson, J., & York, D. G. 2006, AJ, 132, 2496
Keeney, B. A., Stocke, J. T., Rosenberg, J. L., et al. 2012, ApJ, submitted
Kereš, D., & Hernquist, L. 2009, ApJL, 700, 1
Kereš, D., Katz, N., Fardal, M., Davé, R., & Weinberg, D. H. 2009, MNRAS, 395, 160
Klypin, A., Kravtsov, A. V., Bullock, J. S., & Primack, J. R. 2001, ApJ, 554, 903
Lanzetta, K. M., Bowen, D. V., Tytler, D., & Webb, J. K. 1995, ApJ, 442, 538
Larson, D., Dunkley, J., Hinshaw, G., et al. 2011, ApJS, 192, 16
Larson, R. B. 1972, MNRAS, 157, 121
Lehner, N., & Howk, J. C. 2011, Sci, 334, 955
Lehner, N., Howk, J. C., Tripp, T. M., et al. 2013, ApJ, submitted
Lehner, N., Savage, B. D., Richter, P., et al. 2007, ApJ, 658, 680
Lehnert, M. D., & Heckman, T. M. 1996, ApJ, 462, 651
Martin, C. L., Shapley, A. E., Coil, A. L., et al. 2012, ApJ, 760, 127
Marzke, R. O., Huchra, J. P., & Geller, M. J. 1994, ApJ, 428, 43
Mateo, M. 1998, ARA&A, 36, 435
McGaugh, S. S., Schombert, J. M., Bothun, G. D., & de Blok, W. J. G. 2000, ApJL, 533, 99
McLin, K. M. 2003, PhD thesis, Univ. Colorado Boulder
McLin, K. M., Giroux, M. L., & Stocke, J. T. 1998, in ASP Conf. Ser. 136, Galactic Halos, ed. D. Zaritsky (San Francisco, CA: ASP), 175
Meyer, M. J., Zwaan, M. A., Webster, R. L., Schneider, S., & Staveley-Smith, L. 2008, MNRAS, 391, 1712
Montero-Dorta, A. D., & Prada, F. 2009, MNRAS, 399, 1106
Morris, S. L., Weymann, R. J., Dressler, A., et al. 1993, ApJ, 419, 524
Morris, S. L., Weymann, R. J., Savage, B. D., & Gilliland, R. L. 1991, ApJL, 377, 21
Moster, B. P., Naab, T., & White, S. D. M. 2012, MNRAS, submitted (arXiv:1205.5807)
Moster, B. P., Somerville, R. S., Maulbetsch, C., et al. 2010, ApJ, 710, 903
Mulchaey, J. S. 2000, ARA&A, 38, 289

Mulchaey, J. S., Mushotzky, R. F., Burstein, D., & Davis, D. S. 1996, ApJL, 456, 5
Osterman, S., Green, J., Froning, C., et al. 2011, Ap&SS, 335, 257
Peeples, M. S., & Shankar, F. 2011, MNRAS, 417, 2962
Penton, S. V., Shull, J. M., & Stocke, J. T. 2000a, ApJ, 544, 150
Penton, S. V., Stocke, J. T., & Shull, J. M. 2000b, ApJS, 130, 121
Penton, S. V., Stocke, J. T., & Shull, J. M. 2002, ApJ, 565, 720
Penton, S. V., Stocke, J. T., & Shull, J. M. 2004, ApJS, 152, 29
Prochaska, J. X., Chen, H.-W., Howk, J. C., Weiner, B. J., & Mulchaey, J. S. 2004, ApJ, 617, 718
Prochaska, J. X., Weiner, B., Chen, H.-W., Cooksey, K. L., & Mulchaey, J. S. 2011a, ApJS, 193, 28
Prochaska, J. X., Weiner, B., Chen, H.-W., Mulchaey, J. S., & Cooksey, K. L. 2011b, ApJ, 740, 91
Putman, M. E., Bland-Hawthorn, J., & Veilleux, S. 2003, ApJ, 597, 948
Putman, M. E., Peek, J. E. G., & Joung, M. R. 2012, ARA&A, 50, 491
Richter, P., Savage, B. D., Tripp, T. M., & Sembach, K. R. 2004, ApJS, 153, 165
Richter, P., Sembach, K. R., Wakker, B. P., et al. 2001, ApJ, 559, 318
Robitaille, T. P., & Whitney, B. A. 2010, ApJL, 710, 11
Salucci, P., Lapi, A., Tonini, C., et al. 2007, MNRAS, 348, 41
Sarazin, C. L. 1988, X-Ray Emission from Clusters of Galaxies (Cambridge: Cambridge Univ. Press)
Savage, B. D., Lehner, N., & Narayanan, A. 2011a, ApJ, 743, 180
Savage, B. D., Narayanan, A., Lehner, N., & Wakker, B. P. 2011b, ApJ, 731, 14
Savage, B. D., Narayanan, A., Wakker, B. P., et al. 2010, ApJ, 721, 960
Schaye, J. 2001, ApJ, 559, 507
Sembach, K. R., Howk, J. C., Savage, B. D., Shull, J. M., & Oegerle, W. R. 2001, ApJ, 561, 573
Sembach, K. R., Savage, B. D., Lu, L., & Murphy, E. 1995, ApJ, 451, 616
Sembach, K. R., Wakker, B. P., Savage, B. D., et al. 2003, ApJS, 146, 165
Shapley, A. E., Steidel, C. C., Pettini, M., & Adelberger, K. L. 2003, ApJ, 588, 65
Sheth, R. K., & Tormen, G. 1999, MNRAS, 308, 119
Shull, J. M., Jones, J. R., Danforth, C. W., & Collins, J. A. 2009, ApJ, 699, 754
Shull, J. M., Smith, B. D., & Danforth, C. W. 2012, ApJ, 759, 23
Shull, J. M., Stevans, M., Danforth, C., et al. 2011, ApJ, 739, 105
Skillman, E. D. 2005, NewAR, 49, 453
Spitzer, L. 1956, ApJ, 124, 20
Steidel, C. C. 1995, in QSO Absorption Lines, ed. G. Meylan (Garching: Springer), 139
Stinson, G., Brook, C., Prochaska, J. X., et al. 2012, MNRAS, 425, 1270
Stocke, J. T., Keeney, B. A., & Danforth, C. W. 2010, PASA, 27, 256
Stocke, J. T., Keeney, B. A., McLin, K. M., et al. 2004, ApJ, 609, 94
Stocke, J. T., Penton, S. V., Danforth, C. W., et al. 2006, ApJ, 641, 217
Strateva, I., Ivezić, Z., Knapp, G. R., et al. 2001, AJ, 122, 1861
Thom, C., Tumlinson, J., Werk, J. K., et al. 2012, ApJL, 758, 41
Tilton, E. M., Danforth, C. W., Shull, J. M., & Ross, T. L. 2012, ApJ, 759, 112
Trenti, M., Stiavelli, M., Bouwens, R. J., et al. 2010, ApJL, 724, 202
Tripp, T. M., Jenkins, E. B., Williger, G. M., et al. 2002, ApJ, 575, 697
Tripp, T. M., Lu, L., & Savage, B. D. 1998, ApJ, 508, 200
Tripp, T. M., Sembach, K. R., Bowen, D. V., et al. 2008, ApJS, 177, 39
Tumlinson, J., & Fang, T. 2005, ApJL, 623, 97
Tumlinson, J., Shull, J. M., Giroux, M. L., & Stocke, J. T. 2005, ApJ, 620, 95
Tumlinson, J., Thom, C., Werk, J. K., et al. 2011, Sci, 334, 948
van de Voort, F., & Schaye, J. 2012, MNRAS, 423, 2991
Wakker, B. P. 2001, ApJS, 136, 463
Wakker, B. P., & Savage, B. D. 2009, ApJS, 182, 378
Wakker, B. P., & van Woerden, H. 1997, ARA&A, 35, 217
Wakker, B. P., York, D. G., Howk, J. C., et al. 2007, ApJL, 670, 113
Weiner, B. J., Coil, A. L., Prochaska, J. X., et al. 2009, ApJ, 692, 187
Werk, J., Prochaska, J. X., Thom, C., et al. 2012, ApJS, in press (arXiv:1212.0558)
Weymann, R., Rauch, M., Williams, R., Morris, S., & Heap, S. 1995, ApJ, 438, 650
White, S. D. M., Navarro, J. F., Evrard, A. E., & Frenk, C. S. 1993, Natur, 366, 429
Yao, Y., Shull, J. M., Wang, Q. D., & Cash, W. 2012, ApJ, 746, 166
Yao, Y., Wang, Q. D., Penton, S. V., et al. 2010, ApJ, 716, 1514